



Università di Pisa

---

DIPARTIMENTO DI FISICA "ENRICO FERMI"

Corso di Laurea in Fisica

TESI DI LAUREA

## Commissioning and First Data Analysis of the Mainz Radius Experiment.

Candidato:

**Adriano Del Vincio**

Matricola 562946

Relatore:

**Prof. Francesco Forti**

**Prof.ssa Concettina Sfienti**



# Contents

<b>Appendices</b>	<b>4</b>
<b>1 Neutron Skin Thickness Measurement</b>	<b>9</b>
1.1 The Mainz Radius Experiment . . . . .	9
1.2 Nuclear Equation of State (EOS) and Neutron Skin Thickness . . . . .	10
1.3 Parity-violating Scattering Experiment . . . . .	12
1.3.1 Neutron Star Radius . . . . .	14
1.4 Transverse Asymmetry . . . . .	15
1.4.1 Description of the Process . . . . .	16
1.4.2 Concept of the Experiment . . . . .	18
<b>2 Experimental setup</b>	<b>21</b>
2.1 Overview of the Experiment . . . . .	21
2.2 Statistical Uncertainty . . . . .	22
2.3 MAMI . . . . .	23
2.3.1 Polarized Beam . . . . .	26
2.3.2 Vertical Polarization Measurement . . . . .	27
2.3.3 Mott Polarimeter . . . . .	28
2.4 Experimental Hall Setup . . . . .	29
2.5 Detector Description . . . . .	31
2.6 Beam Monitors . . . . .	33
2.6.1 Beam stabilization . . . . .	35
2.7 Electronics . . . . .	36
2.7.1 Voltage to Frequency Converter . . . . .	36
2.7.2 Master Board . . . . .	36
2.7.3 Nino Board . . . . .	37
<b>3 Detectors Test, Alignment and Calibration.</b>	<b>39</b>
3.1 Nino Board . . . . .	39
3.2 Detector Test . . . . .	40
3.3 Calibration . . . . .	45
3.3.1 Alignment of the Scattering Plane. . . . .	45
3.3.2 Beam Monitor Calibration, XY Monitor . . . . .	46
3.3.3 Current (PIMO) Calibration . . . . .	48
3.3.4 Energy Monitor (ENMO) calibration. . . . .	49
3.3.5 Calibration of the PMTs . . . . .	51
3.3.6 Auto-calibration Procedure . . . . .	54
3.4 Data Tree Implementation . . . . .	57
<b>4 Asymmetry on Carbon and Rates on Lead Target.</b>	<b>59</b>
4.1 Model for Fitting the Data . . . . .	59
4.2 Data Pre-selection and Fit . . . . .	60
4.3 Polarization Loss . . . . .	64
4.4 Fit with a Linear Model . . . . .	66

4.5	False Asymmetries . . . . .	71
4.5.1	Energy Asymmetry . . . . .	73
4.6	Rates on Lead . . . . .	74
<b>5</b>	<b>Final Result and Conclusion</b>	<b>77</b>
5.1	Linear Model Result . . . . .	79
5.2	Data Without Polarization . . . . .	79
5.3	Conclusion and Outlook . . . . .	80
<b>Appendices</b>		<b>81</b>
.1	Abbreviations . . . . .	83
.2	Data Tree . . . . .	83

# Commissioning and first data analysis of the Mainz Radius Experiment.

Adriano del Vincio

## Abstract

The Mainz Radius Experiment (MREX) is an experimental campaign with the aim of determining fundamental properties of the equation of state (EOS) of nuclear matter. All of the thermodynamic properties of a system of nucleons, including energy, pressure, temperature, density, and the asymmetry between the number of neutrons and protons in nuclear-matter, are contained in the EOS. An important parameter, poorly-known at the state of current knowledge, is the slope of the symmetry energy at saturation density  $L$ , which quantifies the dependencies of the energy per nucleon associated with the changes in neutron-proton asymmetry. It is also an essential element for the determination of the radius of neutron star, whose description is still determined by the EOS, despite a difference of many order of magnitude with respect to the physical dimensions of the nuclei. The slope of the symmetry energy  $L$  is strongly correlated to a characteristic shown by heavy nuclei, the neutron-skin thickness, that is the difference between the spacial distribution radius  $R$  of neutrons and protons. Nowadays it is well-known, thanks to various nuclear physics experiments, that the neutrons of a nucleus tend to accumulate at a larger radius, forming a neutral thin layer around atomic nuclei. This peculiar characteristic is known in literature as neutron-skin thickness. The experimental measurement of this quantity is the main method to estimate the value of  $L$ , which is used as an input to many theoretical models of neutron stars. MREX is focused on the determination of the neutron skin thickness of  $^{208}Pb$  from parity-violating experiments (PV) performed at the future MESA electron accelerator in Mainz, that is currently under construction. The parity-violating experiments, where longitudinal polarized electrons scatter from a fixed target at a single value of momentum transfer, consist in the determination of the cross section asymmetry  $A_{pv} = \frac{\sigma^+ - \sigma^-}{\sigma^+ + \sigma^-}$  related to the different longitudinal polarization state of the beam. The parity-violating electron scattering is a valid probe to determine the neutron-skin thickness, because it is highly sensitive to the neutron distribution due to the larger coupling of the  $Z^0$  boson to the weak charge  $Q_W$  of neutrons, which is approximately  $-0.99$  per neutron, while that of the proton is  $0.07$ . In this context, it is necessary to determine one of the possible background sources for the PV experiments, known as beam normal single spin asymmetry  $A_n$ , or transverse asymmetry. The asymmetry  $A_n$ , that concerns transversely polarized electrons, comes from the interference between two Feynman diagrams where one or two virtual photons are exchanged, giving a contribution of the order of  $20\text{ ppm}$ . Because the values of  $A_n$  are typically higher than  $A_{pv}$ , the presence of a small transverse electron polarization component could produce an effect that is of the same order of magnitude of the  $A_{pv}$ . The work of this thesis focuses on the measurement of the transverse asymmetry  $A_n$  carried out at the Mainz microtron accelerator (MAMI) on a  $^{12}C$  target. The  $^{12}C$  target is particularly suited for studying and testing the electronics systems and detectors that will be employed in the next phase of the MREX experiment, the determination of  $A_n$  for  $^{208}Pb$ . The measurement consists in the determination of  $A_n$  using two Cherenkov detectors made of fused-silica materials coupled to 3 and 8 photo-multiplier tubes. The two detectors have been tested in the laboratory, together with the new electronics for the data read-out, that consist in the NINO-asic board with which the impulse signals coming from the detectors are acquired. The beam parameters, as the transverse position of the beam, the scattering angles, and the current intensity and energy are determined with particular accuracy because their variation over time can result in effects that overlap with  $A_n$ . This required the development of a new analysis program, processing the raw data to extract the beam parameters relevant for the analysis, and separating the contributions of the false asymmetries from  $A_n$ . The work consisted in a first part dedicated to the calibration of the monitors, to measure the parameters of the beam. The second part was focused on the analysis of the data collected during the beam time, removing the outliers, identifying possible errors and isolating the contribution of false asymmetries.  $A_n$  has been measured for electron-carbon scattering at two fixed angles ( $\theta_B = -22.5^\circ$ ,  $\theta_A = 22.5^\circ$ ) corresponding to a transfer momentum of  $Q^2 = 0.04\text{ GeV}^2$ . The measured values are:  $A_B = -21 \pm 5\text{ (stat)}\text{ ppm}$  for

detector B and  $23.1 \pm 1.7$  (*stat*) *ppm* for detector A. The different sign of the two measurements is in agreement with the opposite kinematic, and the two measurements are compatible within 1  $\sigma$ , and in agreement with the previous measurements performed at MAMI. The results obtained confirm the capabilities of the electronic systems and components used during the experiments and are encouraging in anticipation of the next measurement of the transverse asymmetry for lead.

# Organization of Contents

This thesis is divided into two parts: the first part is dedicated to the motivation behind the MREX experiment and the description of MAMI electron accelerator, where most of the work was carried out. The second part focuses on the analysis of the data collected during the experiment. The list below is an overview of each chapter and a brief explanation of its contents:

- **chapter 1:** Motivation of the MREX experiment for the measurement of the neutron skin thickness of  $^{208}Pb$ . The equation of state (EOS) for nuclear matter is given, paying special attention to the slope of the symmetry energy at saturation density  $L$ . This term relates the EOS for nuclear matter to the structure of the neutron star, and is directly related to the neutron star radius. Its determination is of great significance for distinguishing various existing theoretical EOS models, and also for the internal structure of neutron star. Following, the parity violating electron scattering (PV) on  $^{208}Pb$  is discussed. The PV scattering is the main experimental method to extract the neutron skin thickness  $\delta r_{np}$ , which is correlated to  $L$ . At the end of this chapter, we briefly introduce the Beam Normal Single Spin Asymmetry (BNSSA), also known as transverse asymmetry, the subject of this thesis. The BNSSA represents the most important background process in parity violating experiments, the determination of which is mandatory for isolating possible systematic effects.
- **chapter 2** This chapter focuses on the MAMI electron acceleration and its structure, based on a cascade of microtrons, to accelerate the electrons. One section of the chapter is dedicated to the beam monitors, that measure the beam parameters using resonant electromagnetic cavities which are excited by the passage of the electrons. These beam parameters are necessary to estimate and remove the effect of beam fluctuations on the total asymmetry  $A_{tot}$ . Finally, we briefly introduce the setup for measuring the transverse asymmetry, and describe the two Cherenkov detectors used.
- **chapter 3:** In this chapter some simple detector tests performed in the laboratory are introduced, and the result of the calibration phase, which precedes the transverse asymmetry measurement, is discussed. The calibration involves measuring the parameters to convert the raw data from beam monitors into data with the correct physical units. After calibrating the monitors, we explain the auto-calibration procedure, required to measure the PMT offset, that later are used to correct the asymmetry measurements.
- **chapter 4:** The analysis of data is the main topic of chapter 4. For various values of the beam current, the rates with a lead target are determined, and the time required to measure the transverse asymmetry with lead with an precision of  $\simeq 2\text{ ppm}$  is calculated. Following that, we discuss the data selection and the fit procedure for carbon data.
- **chapter 5:** The result of the analysis is reported. The transverse asymmetry is measured by each PMT individually, and the result are averaged to obtain a single  $A_n$  measurement for each detector.



# Chapter 1

# Neutron Skin Thickness Measurement

The physical motivation for the MREX experiment are the topic of the first chapter of this thesis. Starting from the semi-empirical formula for the binding energy of the nuclei, a simplified model is introduced, which describes some properties of the nuclear matter, in the case of dominant neutron density. With this it is possible to introduce  $L$ , the slope of the symmetry energy at saturation density, and the connection between this quantity and the neutron skin thickness and the radius of neutron stars. MREX will measure the neutron skin thickness via parity-violating experiment, as explained in a section of this chapter. The chapter ends with the basic concepts of the transverse asymmetry, the primary focus of this thesis, and the concept of the experiment to measure this quantity.

## 1.1 The Mainz Radius Experiment

The Mainz Radius Experiment (MREX), at the Mainz nuclear physics institute, is an experimental campaign with the aim of investigating the nature of atomic nuclei, by measuring the neutron skin thickness of  $^{208}Pb$ . The characteristics of atomic nuclei are mainly determined by the strong interaction, whose existence was firstly speculated by Yukawa in 1935. The strong interaction is responsible of a broad range of phenomena: from the nature of the nuclei, the compositions of baryons and meson to the exotic structure of neutron stars. Hence, nuclear physics offers many answers to fundamental questions that are important also in other fields of physics. The neutron stars, which are among the most researched astrophysical objects, are particularly well suited to study theories of dense nuclear matter. It can be surprising to think that, despite having differences of so many orders of magnitude, neutron rich nuclei and neutron stars share the same fundamental physics description, given by the Equation Of State (EOS) of nuclear matter [1]. The EOS represents the fundamental relation between state variables such as temperature, energy, pressure and the neutron-proton asymmetry. Specifically, the goal of the MREX experiment is to determine an important parameter of the EOS, the slope of the symmetry energy at saturation density  $L$ , which controls the change in energy due to presence of an asymmetry between neutron and proton densities. This parameters plays an important role for the determination of the radius of the neutron stars and it is also responsible for a peculiar characteristic shown by heavy nuclei: the neutron skin thickness. The neutron skin thickness  $\delta r_{np}$  is a phenomena that affect heavy nuclei, which consists in the accumulation of the excess of neutrons near the surface, producing a neutral layer of neutrons. It is defined as:

$$\delta r_{np} = \sqrt{\langle r_n^2 \rangle} - \sqrt{\langle r_p^2 \rangle}, \quad (1.1)$$

where,  $\langle r_n^2 \rangle$  and  $\langle r_p^2 \rangle$  are the rms radii of proton and neutron distributions. The neutron skin thickness is sensitive to  $L$ , so an accurate determination of  $\delta r_{np}$  provides significant constraints on the value of  $L$ , which can be used as an input to many theoretical models of the structure of the neutron stars. There are numerous challenges in determining  $\delta r_{np}$ .  $r_p$  is measured with high accuracy with the electrons elastic scattering experiments, whereas the determination of  $r_n$  has traditionally relied on hadronic experiments, such as proton-nucleus scattering,  $\pi^0$  photo-production,  $\alpha$  and  $\pi$  nucleus scattering. These processes suffer from large and often uncontrolled theoretical uncertainties that

compromise the extraction of  $r_n$ . The most promising method, that is the least model dependent, is parity-violating electron scattering, where longitudinal polarized electrons are elastically scattered off an unpolarized target. This method consists in the measurement of the cross-section asymmetry between right and left handed electrons:

$$A_{pv} = \frac{\sigma_R - \sigma_L}{\sigma_R + \sigma_L} \quad (1.2)$$

This process is dominated by the exchange of a virtual photon, which is sensitive to the charge form factor, and of a  $Z_0$  boson, that is sensitive to the weak form factor. Since the weak charge of the neutron is  $Q_w = 0.99$  and the weak charge of the proton is 0.04, the weak form factor contains the information on the neutron density, necessary to measure  $\delta r_{np}$ . In this context, the MREX experiment is an experimental campaign with the aim of measuring the neutron skin thickness via the parity violating scattering with the new MESA electron accelerator, at the nuclear physics institute of Mainz.

## 1.2 Nuclear Equation of State (EOS) and Neutron Skin Thickness

During the 30s of the last century, a considerable part of the scientific community was focused in the study of the structure of atomic nuclei. The discovery that every atoms has a positive charged nucleus dates back to 1908, with the famous Rutherford experiment, where alpha particles scatter on a thin gold foil. In the following years, especially after the birth of quantum mechanics in the second half of the 1920s, important progress was made in the knowledge of atomic nuclei and their properties. In 1935, a significant contribution was given by Carl Friedrich von Weizsäcker and Hans Bethe, who proposed the semi-empirical mass formula, to approximate the mass of an atomic nucleus [2]. Although some refinements have been made over the years, the general structure of the formula is the same today. The model proposed by Weizsäcker is the application of the liquid-drop model for nuclear matter, where the nucleus is described as a drop of protons and neutrons, assumed to be incompressible and held together by a nuclear potential. The semi-empirical mass formula states that the mass of a nucleus with  $Z$  protons and  $N$  neutrons is given by:

$$m = Zm_p + Nm_n - \frac{E_B(N, Z)}{c^2} \quad (1.3)$$

where  $E_B$  is the binding energy, containing 5 parameters:

$$E_B = a_V A - a_s A^{\frac{2}{3}} - a_c \frac{Z^2}{A^{\frac{1}{3}}} - a_{asym} \frac{(N - Z)^2}{A} + \delta(N, Z) \quad (1.4)$$

The first two terms  $a_V, a_s$  are the volume energy and the surface energy, and conceptually analogous to the volume and surface parameter of the liquid drop model. The volume term represent the energy due to the interaction of each nucleon with the other nearby nucleons. This term is proportional to  $A = N + Z$ , that is the number of nucleons, which is proportional to the volume. The second term represents the surface energy, and it is a correction to the volume energy. For the volume energy parameter, it is assumed that each nucleon interacts with a constant number of nearby nucleons. This is not true, because the strong nuclear force is a short distance interaction, and furthermore the external protons and neutrons have less neighbors to interact with. This correction terms is proportional to  $A^{\frac{2}{3}}$ , thus proportional to the surface area. The third term, with coefficient  $a_c$  denote the binding energy correction due to the Coulomb repulsion between protons. The fourth term, the asymmetry term, is proportional to the asymmetry between neutrons and protons. The theoretical justification for this terms is due to the Pauli exclusion principle. Neutrons and protons are distinct type of particles, and occupy different quantum states. Because neutrons/protons are fermions, they can not occupy a state with the same quantum numbers, therefore higher energy states are progressively filled. If there is an asymmetry between neutrons and protons, for example the number of neutrons is larger than the number of protons, some neutrons will be in higher energy states with respect to the protons. The imbalance between the nucleons causes the energy to be higher with respect to the situation with the

equal number of  $p$  and  $n$ . The last term is the pairing term, and describes the effect of spin coupling, which leads to the formation of protons or neutrons pairs. It has a positive or negative values depending on the parity of  $N, Z$ . We stress the fact that the liquid-drop model has the underlying assumption that the nucleons are incompressible. For this reason it is well defined the concept of saturation density  $\rho_0$ , the maximum density beyond which nucleons can not be compressed further. In the end the liquid drop models assume that the density  $\rho$  is almost equal to  $\rho_0$  and independent of mass number  $A$ . In the context of neutron stars, it is more useful to consider the binding energy per nucleons  $\epsilon = \frac{-E_B}{A}$  in the thermodynamic limit in which the number of nucleons (and so the volume) is taken to infinity:

$$\epsilon(\rho_0, \alpha) = -\frac{E_B}{A} = -a_V + a_{asym} \left( \frac{\rho_n - \rho_p}{\rho_n + \rho_p} \right)^2, \quad (1.5)$$

Where we have introduced the proton and neutron densities  $\rho_n$  and  $\rho_p$ , and the saturation density  $\rho_0$ . We notice that the surface term and the pairing terms vanish for  $A \rightarrow \infty$ , and we are neglecting the Coulomb term  $a_c$ <sup>1</sup>. In reality, this simple equation is only an approximation, because the nuclear matter doesn't behave like an ideal liquid drop, and it is not incompressible. To describe the response of the nuclear matter to density variation, as well as temperature, etc. we need the equation of state (EOS) of the system, the fundamental relation that binds all these quantities together. In the ideal limit of  $T = 0$ , the EOS for neutron stars depends on  $\rho$ , the conserved baryon density, and neutron-proton asymmetry  $\alpha$ . Starting from equation 1.5, the energy density is expanded in a power series of  $\alpha = \frac{\rho_n - \rho_p}{\rho_n + \rho_p}$ :

$$\epsilon(\rho, \alpha) \simeq \epsilon_{snm} + \alpha^2 S(\rho) + O(\alpha^4), \quad (1.6)$$

where the energy is split in two terms, with  $\epsilon_{snm} = \epsilon(\rho, \alpha = 0)$  representing the energy density for snm, i.e with equal amount of neutrons and protons. Since the the strong force does not depend on the isospin, no odd power of  $\alpha$  appears in the expansion; or in other words, neglecting electromagnetic interaction and weak interaction, the EOS depends only on the relative asymmetry between neutrons and protons and it does not matter if such an asymmetry is biased towards protons or neutrons. The term  $S(\rho)$  is the symmetry energy, and represents the cost of converting symmetric nuclear matter ( $\alpha = 0$ ) to pure neutrons matter, as in the case of neutron star. Now we can proceed considering the saturation density. A further expansion around  $\rho_0$  is done, following [3]:

$$\begin{aligned} S(\rho) &= J + L \cdot \frac{\rho - \rho_0}{3\rho_0} + \frac{1}{2} K_{sym} \cdot \left( \frac{\rho - \rho_0}{3\rho_0} \right)^2 \\ \epsilon_{snm}(\rho) &= \epsilon_0 + \frac{1}{2} K_0 \left( \frac{\rho - \rho_0}{3\rho_0} \right)^2 \end{aligned} \quad (1.7)$$

Several new terms appear in this expression:

- $\epsilon_0$  is the energy per nucleon for symmetric matter at saturation density.
- $J$  is the symmetry energy at saturation density.
- $L$  is the slope of the symmetry energy.
- $K_0$  is the incompressibility coefficient for symmetric matter.
- $K_{sym}$  is the incompressibility coefficient for the symmetry energy.

In equation 1.7 appears a new quantity:  $L$ , the slope of the symmetry energy. This is a key component of the EOS, whose value is an important parameter to determine the radius of neutron star.  $L$  quantifies the difference between the symmetry energy at saturation (as in the nuclear core)

---

<sup>1</sup>This term is relevant in presence of a  $\rho_p \neq 0$ , but neutron star can be assumed globally with almost zero electric charge, so this will not give a contribution.

and the symmetry energy at lower densities, as in the nuclear surface.  $L$  is also related to the pressure  $P$  at saturation density. Giving the EOS in term of  $\rho$  and  $\alpha$ , the pressure can be written as:

$$P = \rho^2 \frac{\partial \epsilon(\rho, \alpha)}{\partial \rho} \quad (1.8)$$

Equation 1.8 can be simply derived from the first principle of thermodynamics. Now it is possible to substitute everything in  $\epsilon$ , making all the dependencies explicit:

$$\epsilon(\rho, \alpha) = (\epsilon_0 + \alpha^2 J) + \alpha^2 Lx + \frac{1}{2}(K_0 + \alpha^2 K_{sym})x^2, \quad (1.9)$$

where  $x = \frac{\rho - \rho_0}{3\rho_0}$ . Considering pure neutron matter, with  $\alpha = 1$ , the pressure at saturation density  $P_0$  can be easily computed with the formula (1.8). The result is:

$$P_0 \simeq \frac{1}{3}\rho_0 L \quad (1.10)$$

From this expression we learn that the slope of the symmetry energy is essential to determine the pressure for densities near saturation. Such conditions are encountered in nuclei and in the core of neutron stars. The contribution of the symmetric term  $\epsilon_{snm}(\rho)$  vanishes, and the pressure depends only on  $L$ , at first order. Knowing that, it becomes clear the link between  $L$  and the neutron skin thickness. Let's consider the case of the  $^{208}Pb$ , with an excess of 44 neutrons. Placing the excess of neutrons in the surface of the nucleus is discouraged by the surface term  $a_S$ , which tends to minimize the area. However, if the excess of neutrons is placed in the core of the nucleus, it increases the symmetry energy  $S(\rho)$ . In conclusion, the neutron skin is the result of the competitions between the surface tension and the slope of the symmetry energy. . Theoretical models, while predicting different values , show that there is a strong correlation between these two quantities, as show in figure (1.1).

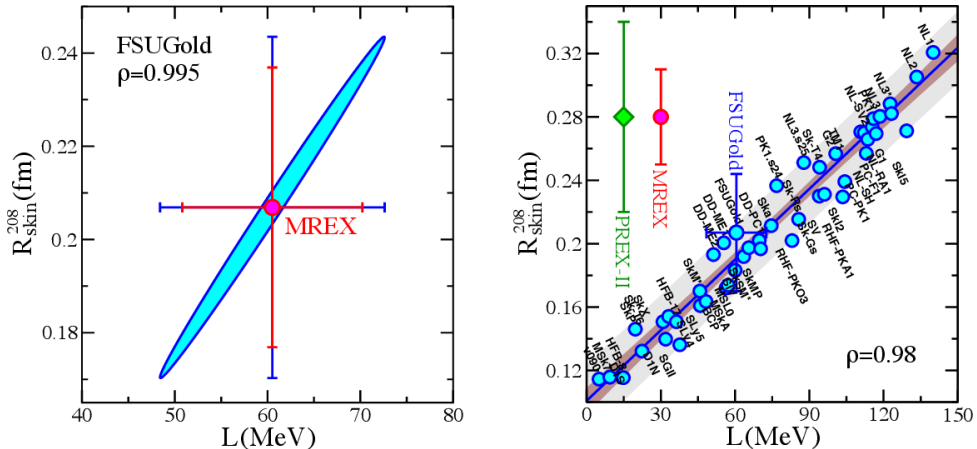


Figure 1.1: *On the right* Neutron skin thickness of  $^{208}Pb$  as a function of the slope of the symmetry energy  $L$ . Each dot represent the a value of  $L$  and  $\delta r_{np}$  as predicted by various theoretical models. The error bars represent  $\pm 0.06$  fm and  $\pm 0.03$  fm for the future experiments of PREX-II and MREX. Notice the different scale for x and y axis, a small uncertainty for the neutron skin measurement correspond to an higher uncertainty for the values of  $L$ . *On the left* Covariance ellipse displaying the correlation between  $L$  and the neutron skin thickness, for FSUGold model. The covariance  $\rho$  is equal to 0.995.

Because of such a strong linear correlation, a measurement of the neutron skin gives access to  $L$ .

### 1.3 Parity-violating Scattering Experiment

Parity violating electron scattering seems to be a promising method for the determination of the neutron-skin thickness of heavy nuclei.  $^{208}Pb$  is chosen because of its significant neutron excess

and stability ( $^{208}Pb$  is a double magic nucleus). The advantage of this method is that it is free from the many uncertainties associated to strong interaction. The main disadvantage is the need to accumulate large statistics, because the reaction are mediated by the weak interaction, associated with smaller scattering amplitude compared to electromagnetic and strong interactions. The parity violating scattering is highly sensitive to the neutron density because, as mentioned above, since the weak charge of the neutron is larger compared to the weak charge of the proton. In this reaction, longitudinally polarized electrons are elastically scattered off a lead target. The important quantity to determine is the parity violating asymmetry  $A_{pv}$ , the difference in cross section between the scattering of right and left handed electrons.

$$A_{pv} = \frac{\sigma_R - \sigma_L}{\sigma_R + \sigma_L}, \quad (1.11)$$

The theoretical calculation of  $A_{pv}$  includes the interference between the exchange of virtual  $\gamma$  and  $Z^0$ . In the Born approximation  $A_{pv}$  is directly proportional to the weak form factor, and is given by:

$$A_{pv} \simeq \frac{G_F Q^2}{4\pi\alpha} \cdot \frac{Q_W F_W(Q^2)}{Z F_{ch}(Q^2)}, \quad (1.12)$$

where  $G_F$  is the Fermi constant,  $Q^2$  is the transferred momentum,  $Z$  and  $Q_W$  are the electric and weak charge of the nucleus,  $F_{ch}$  and  $F_W$  are the charged and weak form factors of the nucleus. The charge form factor of the lead nucleus is known with high accuracy (precision of 0.02 %), so in this limit the only quantity that is unknown is  $F_W(Q^2)$ . In the long wavelength approximation, isolating various moments of the spacial distribution, the weak form factor at single value of momentum transfer is given by:

$$F_W(Q^2) = \frac{1}{Q_W} \int \rho_W(r) \frac{\sin(Qr)}{Qr} d^3r = (1 - \frac{Q^2}{6} R_W^2 + \frac{Q^4}{120} R_W^4 + \dots) \quad (1.13)$$

Where the weak form factor  $F_W$  is normalized in such a way that  $F_W(Q^2 = 0) = 1$ , and the weak charge radius  $R_W$  is introduced, defined as:

$$R_W = \frac{1}{Q_W} \int r^2 \rho_W(r) d^3r \quad (1.14)$$

Using the expansion in equation 1.13, the weak charge radius correspond to  $R_W^2 = -6 \frac{\partial F_W}{\partial Q^2} \Big|_{Q^2=0}$ . In principle  $R_W$  follows from the derivative of the form factor with respect to  $Q^2$  at  $q = 0$ . Since the measurement performed by PREX, and the future measurement of MREX are at a finite  $q$ , one needs to assume some information about the form of the weak density  $\rho_W$ . The form of the weak density and  $F_W$  is assumed to be well described by the Helm model [4]. This model depends on two parameters that are adjusted to reproduce the value of  $F_W(q)$  at the measured value  $q$ . With this method, the weak radius  $R_W$  is extracted from  $A_{pv}$ , as explained in [5]:

$$R_W = 5.83 \pm 0.18(\text{exp.}) \pm 0.03(\text{model}) \text{ fm} \quad (1.15)$$

The last step to calculate  $\delta r_{np}$  is to connect  $r_n$  to  $R_W$ . This is done by writing  $\rho_W$  in terms of the proton and neutron densities  $\rho_p$  and  $\rho_n$  and the weak charges  $q_p$  and  $q_n$ , as explained in [5]. With this last passage, the neutron skin thickness of  $^{208}Pb$  is obtained. Now it is clear that parity-violating experiment are a promising method to extract information about neutron density. The difficulty is represented by the small values of  $A_{pv}$  asymmetry. The value for lead is expected to be  $\simeq 0.6 \text{ ppm}$ . This requires high statistic to reduce the uncertainty of the measurement and high control over the systematic effects. In 2012 the PREX collaboration measured for the first time the neutron skin through parity-violating experiment [6], obtaining:

$$\delta r_{np} = 0.33^{+0.16}_{-0.18} \text{ fm} \quad (1.16)$$

The error associated to this first measurement is not enough small to provide significant constraints on the values of  $L$ . In 2019, a new measurement of the PREX collaboration [7], obtain of  $\delta r_{np} =$

$0.283 \pm 0.071\text{fm}$  The MREX experiment has the objective of measuring the neutron skin of lead with a precision of 10% ( $\pm 0.03\text{ fm}$ ). This high precision is needed to decrease the uncertainty associated to  $L$ . For example, the left plot in 1.1, shows the correlation between the neutron skin thickness of  $^{208}\text{Pb}$  and the slope of the symmetry energy as predicted by FSUGold model ([8]). With a precision of  $\pm 0.03\text{ fm}$ ,  $L$  is determined with  $\pm 12.1\text{ MeV}$ .

### 1.3.1 Neutron Star Radius

We mentioned that the slope of the symmetry energy  $L$  is strongly correlated to the neutron skin thickness of  $^{208}\text{Pb}$  and also to the radius of neutron stars  $R_{ns}$ . We can go deeper in the discussion stating that the maximum neutron-star mass and radius are uniquely constrained by the EOS ([9]). The maximum mass depends on the energy density dependence of the pressure, that must be high enough to oppose the gravitational collapse into a black hole. Moreover, stellar radii are strongly dominated by the pressure of degenerate nuclear matter near the saturation density. The connection between the radius of compact object and pressure is enclosed in the Tolman-Volkov-Oppenheimer equation (TVO) [10] and in the equation of state; assuming a particular EOS, it is possible to resolve the Volkov-Oppenheimer equation, finding the relation between neutron star mass and radius, or radius and pressure (formal proof in [11]). The pressure  $P_c$  is, in large part, determined by the symmetry energy of the equation of state, so there should be a strong correlation between  $L$  and the neutron star radius  $R_{ns}$ . In the end, different theoretical models [12] confirm the connection between  $L$  and  $R_{ns}$ , for example we show the covariance ellipses predicted by FSUGold model between the slope of the symmetry energy  $L$  and the stellar radii in figure 1.2

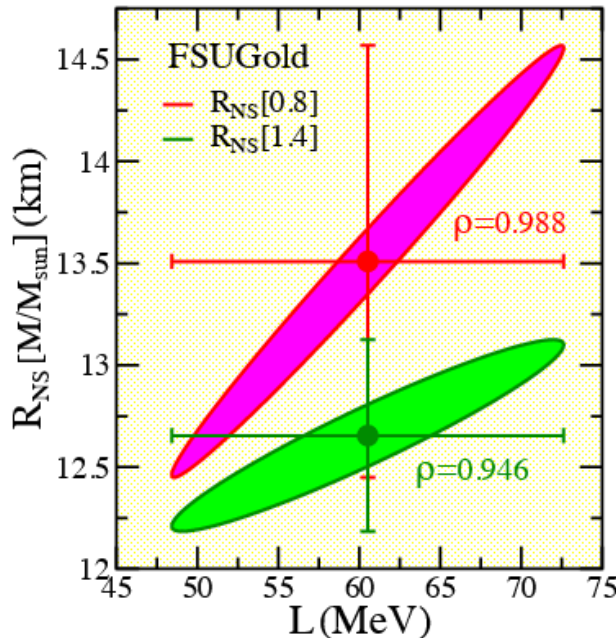


Figure 1.2: Covariance ellipses between slope of the symmetry energy and stellar radii, for 0.8 and 1.4 solar masses, predicted by the relativistic density model FSUGold.

From these consideration, astronomical observations of mass and radii of neutron stars represents important constrains on the EOS . Astronomical observations of the neutron star radius rely traditionally on photometric measurements, assuming that thermal emission of light from the surface follow a blackbody spectrum at uniform temperature. These measurement are affected by systematic uncertainties that are typically of a couple of kilometers. However, the situation is rapidly changing with the beginning of the gravitational wave detection. The first observation of the binary neutron star merger by the LIGO-Virgo collaboration (GW170817 event) opened a new path to measure the neutron-stars radius [13]. In fact, the gravitational wave generated by the merging of two neutron

stars depends on a property called tidal deformability; this parameter describes the tendency of a neutron star to deform in response of the gravitational field of its companion star, developing a mass quadrupole moment. This parameter  $\Lambda$ , is highly sensitive to the ratio of the stellar radius to the Schwarzschild radius:

$$\Lambda = \frac{2}{3} k_2 \left( \frac{c^2 R_{NS}}{GM} \right)^5 \quad (1.17)$$

In this expression,  $M$  and  $R_{NS}$  are the neutron star mass and radius, and  $k_2$  is the second tidal Love number [14], which is computed from the quadrupole component of the gravitational field induced by the companion. With the first detection, an upper limit  $\Lambda < 800$  was placed, corresponding to an upper limit of  $R_{NS}^{1.4} < 13.76$  km [15] for radius of a neutron star with 1.4 solar masses (see figure 1.3). Because of the strong correlation between  $R_{NS}$ ,  $L$  and  $\delta r_{np}$ , an indirect constraint on the neutron skin thickness of  $^{208}Pb$  was obtained:  $\delta r_{np} < 0.25$  fm. However, a more recent analysis [16] of GW170817 has placed a more stringent limit on the Tidal polarizability, with  $\Lambda_{1.4} = 190^{+390}_{-120}$ .

This limit is in slight tension with the larger values measured by PREX collaboration, suggesting that the symmetry energy, for slightly higher density as in neutron stars, decreases with respect to the typical density found in atomic nuclei. This increment and decrement may be an indication of the presence of phase transition in the interior of neutron stars.

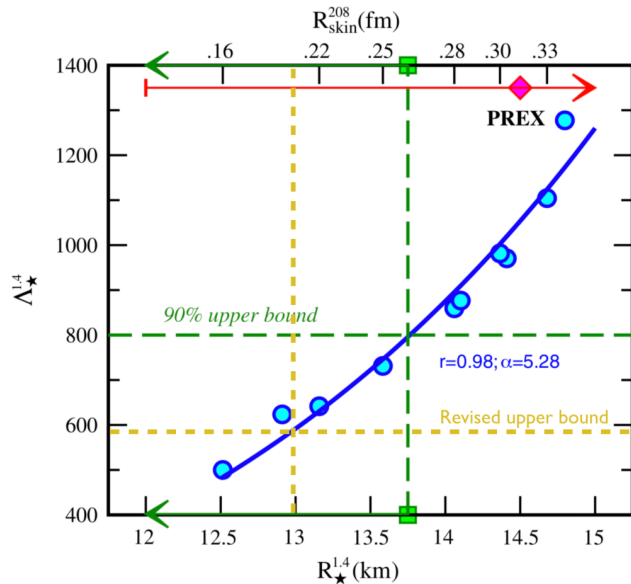


Figure 1.3: Polarizability  $\Lambda$  versus neutron star radius. The point are the prediction of different theoretical models. The first upper bound with 90% credibility is shown in the figure, with a blue dotted line, and the revisited upper bound, in yellow. On the x axis, two variables are shown, the predicted neutron star radius and neutron skin thickness of lead.

## 1.4 Transverse Asymmetry

The parity-violating scattering has numerous advantages for extracting the neutron-skin thickness of nuclei. However, the asymmetry to measure is rather small. To measure such asymmetries, it is necessary to reduce as much as possible the systematic effects, that can alter the result of the measurement. One of the main sources of background for the measurement of  $A_{PV}$  is a different process that concerns transverse polarized electrons. The different polarization of the electrons produce an asymmetry, called beam normal single spin asymmetry (BNSSA), or transverse asymmetry  $A_n$ . Since such asymmetries are typically one order of magnitude larger than the parity-violating ones, a small normal component of the beam polarization during parity-violating experiments can produce a systematic effect that changes the final result. The subject of this thesis is the measurement of

transverse asymmetry  $A_n$  for carbon target, performed at MAMI, the Mainz microtron accelerator. The choice of carbon target is due to the fact that the transverse asymmetry for  $^{12}C$  is well known and already measured at MAMI; the expected asymmetry is roughly 20 ppm, thus it is particularly suited for the commissioning of the new experimental setup. Such asymmetries are challenging because they require calculation of box diagrams with intermediate excited states [17]. After the determination on  $A_n$  for  $^{12}C$ , the next phase of the MREX experiment will be the determination of the transverse asymmetry for  $^{208}Pb$ . As already mentioned, this is mandatory to constrain the systematic effects in PV experiments. However, it is also interesting because in the last measurement performed by PREX [18] the transverse asymmetry for  $^{208}Pb$  target is compatible with zero, with a complete disagreement with the theoretical predictions. Since the theoretical prediction for hydrogen, helium, carbon and zirconium are in agreement with theory, a second, independent measurement of the BNSSA for lead is interesting, to confirm the measurement performed by PREX.

#### 1.4.1 Description of the Process

The Beam Normal Single Spin Asymmetry (BNSSA) arises from the interference of two scattering amplitudes (the exchange of one and two virtual photons) which has a close relationship to the time-reversal operator [17]. The kinematics of the experiment, involving the elastic scattering between an electron and  $^{12}C$  nucleus, is shown in figure 1.4.

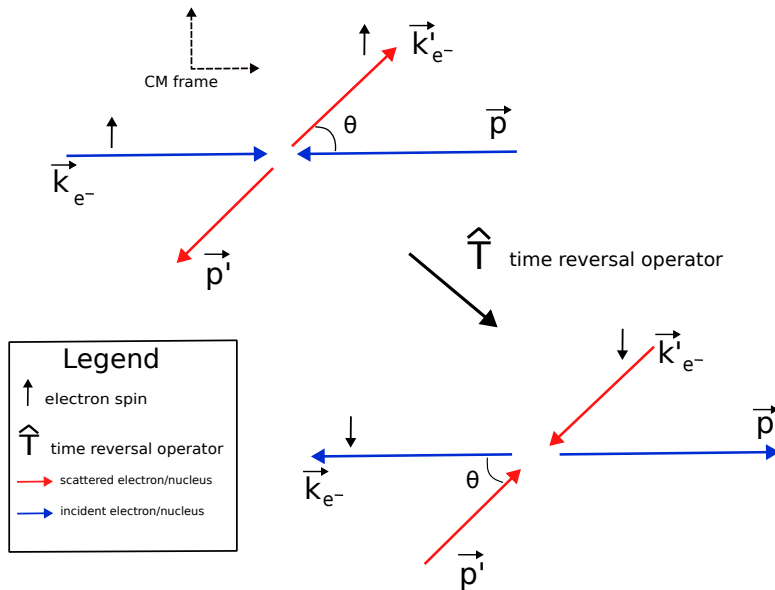


Figure 1.4: Scheme of the scattering process in the center of mass frame. In blue the incident electron and nucleus, in red the outgoing electron and nucleus. All the quantities are referred to the center of mass frame. The small arrow over the vector represent the electron spin, lying in the normal plane.

The transverse asymmetry is defined as the cross-section asymmetry due to the different transverse polarization state of the incoming electron:

$$A = \frac{\sigma_{\uparrow} - \sigma_{\downarrow}}{\sigma_{\uparrow} + \sigma_{\downarrow}} \quad (1.18)$$

it is useful to understand the reason why the presence of an asymmetry in the cross section is related to the time-reversal operator. Looking at the figure of the kinematics, we can compare the two situation before and after applying the time-reversal operator,  $\hat{T}$ . It is evident that:

- Before applying  $\hat{T}$ , we have the incoming electron with  $\vec{k}$  momenta and the nucleus with  $\vec{p}$  momenta. Applying  $\hat{T}$  will exchange the incoming electron and nucleus with the outgoing electron and nucleus.
- The  $\hat{T}$  operator flips also the spin of the incoming electron.

- Considering that the process is elastic, the kinematic is the same with and without applying the Time-reversal operator.

The time-reversal operator exchanges the two different cases of electron scattering with UP and DOWN polarized electron. Since a non-zero asymmetry is observed, between  $\sigma_\uparrow$  and  $\sigma_\downarrow$  (and therefore also in the amplitudes  $A_\uparrow$  and  $A_\downarrow$ ), and given that the  $\sigma_\uparrow$  and  $\sigma_\downarrow$  are connected by the time-reversal transformation, we can state that the asymmetry originates by the behaviour of the scattering amplitude when  $\hat{T}$  operator is applied to the system. Therefore is important to see more in detail the structure of the  $\hat{T}$ .  $\hat{T}$  is an anti-unitary operator that can be always decomposed as:

$$\hat{T} = U \cdot K$$

Where  $U$  is an unitary operator, while  $K$  is the complex conjugation operator that generates the complex conjugate of the coefficients in front of the state vectors. If we consider a ket describing a system, we have that:

$$Kc|\alpha\rangle = c^*K|\alpha\rangle \quad (1.19)$$

Now, let's consider the total amplitude of our system. We want to apply the  $\hat{T}$  operator. We assume that the amplitude of the system consist of two term, one real and one imaginary, which correspond to the two different scattering processes. Since the electromagnetic interaction conserve  $CP$  symmetry, also  $T$  is conserved. However the time reversal operator changes the relative sign between the real and complex terms of the scattering amplitude. Therefore, the value of the cross-section is changed when the time reversal operator is applied to the system, and this give rise to the asymmetry  $A_n$ . At the  $\alpha$  leading order, the two scattering processes that give rise to the asymmetry involve the one-photon-exchange (OPE) and two-photon-exchange (TPE) Feynmann diagrams, that are show in figure 1.5

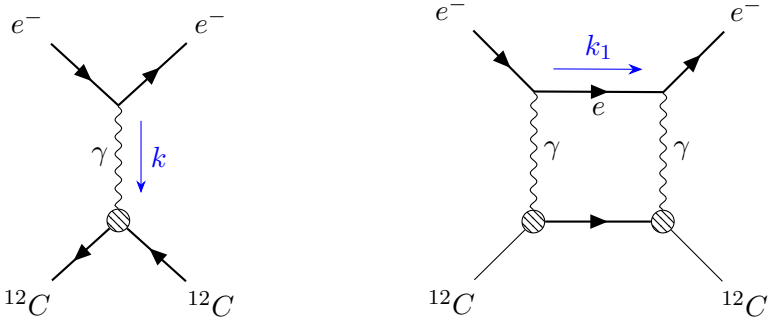


Figure 1.5: TPE and OPE diagrams in electron nucleus scattering.

The important quantity to compute the cross section is the scattering amplitude. The scattering amplitude is given by the two contributions: the exchange of a single virtual photon  $A_1$  and the terms given by the two photon exchange  $A_2$ . In general we can write that the total scattering amplitude  $S$  [17]:

$$S = \frac{e^2}{Q^2} \bar{u}(k') [m_e A_2 + A_1 \vec{P}] u(k) \quad (1.20)$$

Where  $\vec{P}$  is given by:

$$\vec{P} = \frac{\vec{p} + \vec{p}'}{2}. \quad (1.21)$$

$A_1$  term in the scattering amplitude correspond to the charge form factor of the nucleus:

$$A_1 = 2Z F_N(Q^2)$$

Where  $Q^2$  is the transferred momentum in the scattering process.

The first term of the scattering amplitude  $A_1$  is T-even, and it is purely real, so it is the imaginary part of the two photon exchange amplitude which gives rise  $A_n$ . In the end, the expression that connects the scattering amplitudes to the transverse asymmetry is given by:

$$A_n = -\frac{m_e}{\sqrt{s}} \tan\left(\frac{\theta_{CM}}{2}\right) \frac{\text{Im}(A_2)}{Z F_N(Q^2)} \quad (1.22)$$

Looking at this formula, the theoretical effort to compute the transverse asymmetry is given by the imaginary part of  $A_2$ . The imaginary part  $A_2$  is related to the two-photon exchange. To compute this quantity, we have to perform an integration over the internal momenta of the electron  $k_1$ . However theoretical calculations of this quantity are challenging, since at energies of  $\simeq 1$  GeV for the incident electrons, contributions from intermediate excited states become important. The various contribution of  $A_2$  are given by the sum of the elastic intermediate state and inelastic terms, which involve hadronic excitations. The inelastic intermediate states are studied and modeled in ([19], [17], [20]). It is beyond our scope to go into a detailed description, we only want to emphasize that in the theoretical calculation several approximations are made, for instance the prediction is reliable only for forward scattering angles, furthermore different assumptions of important variables are made due to lack of data, such as the Compton form factor for  $^{12}C$ , the Compton slope parameter and the use of the approximated Callavan-Gross relation. In summary, the theoretical prediction for the transverse asymmetry are reliable for small scattering angle, that correspond to lower values in transfer momentum  $Q$ ; the experimental data measure by PREX [18] for  $^1H$ ,  $^4He$ , and  $^{12}C$  at  $Q$  values of 0.31 GeV, 0.28 GeV and 0.1 GeV, respectively, are in agreement with the theoretical prediction. The measurement performed at MAMI for  $^{12}C$  [21] is with higher values of transfer momentum ( $Q = 0.2$  GeV) and shows a reasonable agreement with the theoretical prediction, considering also the systematic uncertainties associated to the poorly known Compton slope parameter. The model which describes the transverse asymmetry is:

$$A_N = C_0 \cdot \log\left(\frac{Q^2}{m_e^2 c^2}\right) \frac{F_{Compton}(Q^2)}{F_N(Q^2)} \quad (1.23)$$

Where  $F_N$  is the charge form factor,  $F_{Compton}$  is the Compton form factor of the nucleus, and  $C_0 = \frac{-m_e E_{Lab} \sigma_{\gamma p} MA}{8\pi^2 \sqrt{(2)Z}}$ , where  $\sigma_{\gamma p}$  is the proton photo-absorption cross section,  $A$  the mass number.

The theory presented so far is quite successful in describing the data, but it fails completely with  $^{208}Pb$  nucleus, as PREX reported a measurement of 0 transverse asymmetry [18]. This could suggest that theory fails to describe  $A_n$  for heavy elements; on the other hand it represents an unexpected improvement for the PV scattering experiment. It is important therefore to repeat independently the measurement of the  $A_n$  for  $^{208}Pb$ , to confirm or question the result reported by PREX.

#### 1.4.2 Concept of the Experiment

We have seen so far how the transverse asymmetry is related to the interference between two scattering amplitude, and the theoretical model used to describe the process. The goal from an experimental point of view is to measure this quantity. The challenge is to obtain a valid measure of  $A_n$ , which is of the order of 20 part per million (ppm), taking into consideration all the possible effects that can interfere. To measure  $A_n$ , the straightforward method is to prepare an electron beam, with polarized electron, and send it to a fixed target. The scattered electrons are then collected by a detector placed at a certain angle, with the transverse asymmetry obtained by:

$$A_N(Q) = \frac{N_\uparrow(Q) - N_\downarrow(Q)}{N_\uparrow(Q) + N_\downarrow(Q)} \quad (1.24)$$

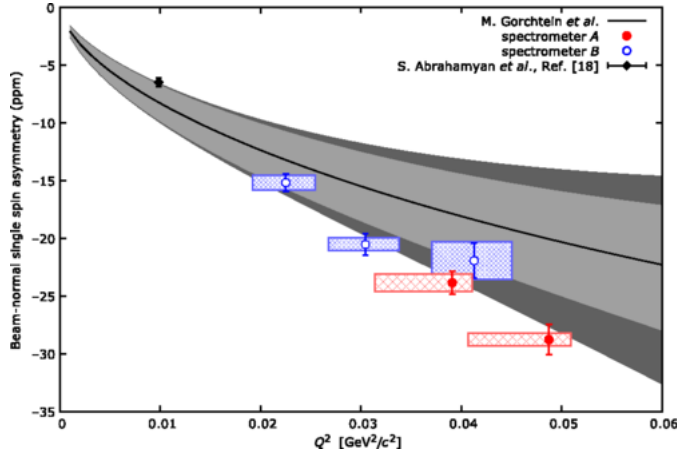


Figure 1.6: Transverse asymmetry measured at MAMI for  $^{12}\text{C}$  target [21]. Theoretical calculation for  $E_{beam} = 570 \text{ MeV}$  is shown.

In an experiment of this type, several requirements need to be satisfied, in order to measure  $A_n$  effectively:

- The accelerator must produce a polarized beam, stable over the time, with an high polarization percentage, in order to amplify the effect.
- The beam energy needs to be quite stable, and should not depend on the polarization state of the electrons. A change in the beam energy associated with the polarization state can lead to a different count rate for  $N_\uparrow$  and  $N_\downarrow$ , and would create false asymmetries that adds to the  $A_n$ .
- The beam must be correctly aligned with the target, with a stable position. If the interaction position changes with to the polarization of the electrons, it will produce another false asymmetry.
- The beam current should not depend on the polarization state of the electrons. If the beam source depends on the polarization, we will have a difference in the event rate and then another false asymmetry.
- It is necessary to reject possible double elastic scattering events, which may contribute to the total asymmetry.

All this demands can be satisfied with an accelerator that has stabilization devices with great precision and that can sustain high beam intensities. This last requirement is necessary to accumulate enough statistics to measure the transverse asymmetry with an accuracy about 1 ppm, in view of the future PV experiments.



# Chapter 2

## Experimental setup

The Mainz Microtron Accelerator (MAMI), where the experiment is set up and the transverse asymmetry is measured, is briefly described in this chapter. The description of the beam monitors used to measure the beam parameters is given a special consideration. Following an overview of the experimental hall, the detectors and the electronic devices used to acquire and process the data.

### 2.1 Overview of the Experiment

To measure the Beam Normal Single Spin Asymmetry, a polarized beam of 570 MeV is directed towards a  $^{12}C$  target that is 10 mm thick. The detectors are made up of two fused-silica bars coupled to 3 (detector B) and 8 (detector A) PMTs, which are used to gather the Cherenkov light released when an electron passes through the fused-silica. The detector are placed inside the two spectrometers of the A1 hall. Due to the high beam current ( $20\mu\text{A}$ ), which is above their operating limits, the standard detectors of the spectrometers are not employed in this experiment. The experiment aims to measure the cross-section asymmetry between the two electron spin orientations. The PMT signals are collected and digitalized by the **NINO** board, after a threshold selection, and sent to the A1 control room computer, where the DAQ program collect the data together with all the data coming from the beam monitors. The produced binary files are later analyzed by the analysis program, which is a significant part of the work done in the framework of the thesis. The data collected are divided in *events* made by 4 *sub-events* in sequence. Each event corresponds to a temporal window of  $\simeq 80\text{ ms}$ , where each sub-event is 20 ms long. This structure into sub-events reflects the polarization sequence of the beam. Unlike the majority of experiments in high energy physics, an event is not a single interaction, but is made by all the electrons interacting with the detectors during the specified time interval. The PMT counts and the beam monitor values are saved for each sub-event, along with their time length (measured in clock cycles by the NINO electronic board) and other values which are required to process beam monitor data. The general structure of the event is the shown in figure 2.1

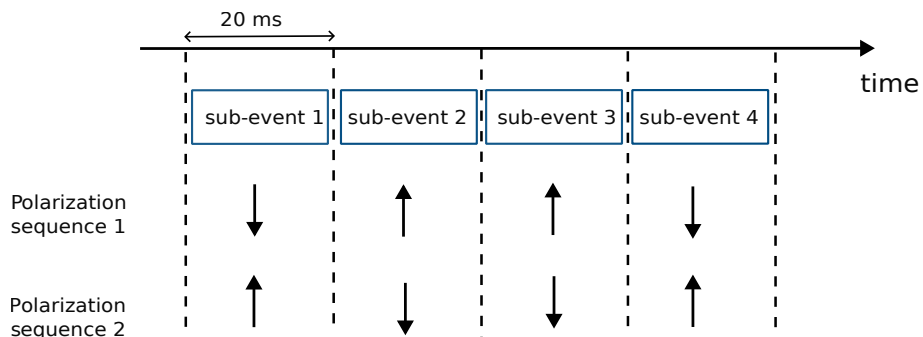


Figure 2.1: General structure of the event. The gate-length of each event is synchronized with the power grid frequency, to reduce possible effects of 50 Hz noise.

The particular choice of 20 ms for each sub-event is made to reduce undesirable effects relate to

the power grid frequency (50 Hz). The gate-length of each sub-events is synchronized with the period of the power grid frequency: this ensures that an entire oscillation of the current takes place within the same sub-event. This cancels out the 50 Hz noise and avoid to produce effects between nearby sub-events.

An event corresponds to a single measurement of  $A_n$ , defined as the asymmetry between the  $\uparrow$  and  $\downarrow$  sub-events. To avoid the creation of false asymmetries by correlated noise or other external sources the polarization states are concatenated following the two patterns  $\uparrow, \downarrow, \downarrow, \uparrow$  and  $\uparrow, \downarrow, \downarrow, \uparrow$ . Which sequence an event belongs to is decided using a De Bruijn sequence. A De Bruijn sequence of order  $n$  is defined as a cyclic sequence where every sub-sequence of length  $n$  appears only once. We have two different polarization pattern, the ones shown in the figure, that can be represented as 1 and 0. For this experiment, the De Bruijn sequence is of order  $n = 6$  bits, corresponding to all the possible sequences of 1 and 0 with a length equal to 6, which are 64 different sub-sequence. It is possible to demonstrate that the number of exactly  $N_{bruijn}$  sequences is:

$$N_{bruijn} = \frac{(k!)^{k^{n-1}}}{k^n}$$

If we substitute in the formula above  $k = 2$  and  $n = 6$ , we have a total of  $\simeq 67 \cdot 10^6$  different sequences. The seed of the De Bruijn sequence is generated with a pseudo random number generator, and the sequence is used to select between  $\uparrow, \downarrow, \downarrow, \uparrow$  and  $\downarrow, \uparrow, \uparrow, \downarrow$ . At this point it could be objected why so much care is taken in choosing randomly the two sequences. At a first glance is certainly easier to select one of the two polarization pattern and reproduce it for every sub-event. However, this would not protect from systematic effects that arise from electronic or beam noise with frequencies similar to the frequency of the polarization pattern. For instance electronic noise with  $f \simeq 10$  Hz could in principle increase the rates for one polarizations state and decrease the other one. The adopted solution to reduce effects of this type is to randomize the pattern selection. Besides this, there is another reason why a De Bruijn sequence is useful. During each polarization flip, we observe a short, transient reduction of the beam current. This reduction in the beam intensity has more influence on patterns where there are more inversion of the polarization respect to the other. With a De Bruijn sequence we ensure that we have a identical number of pairs of patterns, meaning that:

- 25% :  $\uparrow, \downarrow, \downarrow, \uparrow ; \uparrow, \downarrow, \downarrow, \uparrow$
- 25% :  $\downarrow, \uparrow, \uparrow, \downarrow ; \downarrow, \uparrow, \uparrow, \downarrow$
- 25% :  $\downarrow, \uparrow, \uparrow, \downarrow ; \uparrow, \downarrow, \downarrow, \uparrow$
- 25% :  $\uparrow, \downarrow, \downarrow, \uparrow ; \downarrow, \uparrow, \uparrow, \downarrow$

In the top rows we have 4 inversions, while in the two lower rows we have 5 inversions. Other details of the experiments are presented in this chapter. In the next section the operating principles of MAMI electron accelerator are discussed.

## 2.2 Statistical Uncertainty

We can quantify how the statistical error varies according to the amount of data available. With the assumption that  $N_{\uparrow, \downarrow}$  are gaussian distributed variables, we can compute the expected variance

$$Var[A_n] = \frac{1 - A^2}{N_\uparrow + N_\downarrow} \quad (2.1)$$

For a single measurement of the  $A_n$ . For multiple  $n$  measurements, the variance scales as  $\frac{1}{n}$ . Because  $A_n$  is expected to be smaller respect to 1, we can approximate the above formula:

$$V[A_n] = \frac{1}{2N \cdot n} \quad (2.2)$$

The error associated to the reconstructed asymmetry is the square root of the above quantity. If we impose that the error must be  $\leq 1\text{ppm}$  we can easily obtain that the quantity  $n \cdot N$ :

$$n \cdot N > \frac{1}{2} \cdot 10^{12}$$

We will see later that achievable rates  $N_{\uparrow,\downarrow}$  are in the range (20000,60000) counts per event for a carbon target. This number can not be increased at will by acting on the beam current. In the first place there is a limitation on the total charge that the beam source can produce; in addition, a beam with great intensity for an extended periods of time can damage the carbon target up to the risk of melting it. Another idea might be to increase the thickness of the target, to take advantage of the larger cross section. However, by doing so, the number of double scattering events would be increased. To avoid the problem of the double scattering, the nuclear physic community which deals with PV experiments respects the convention that the target thickness should be less than the 10% of the radiation length of the material.

## 2.3 MAMI

MAMI is the electron accelerator located in Mainz, which provides a continuous wave<sup>1</sup>, high intensity, polarized beam for nuclear physics fixed-target experiments. The concept of the Mainz microtron accelerator was developed in the early 1970s, when the researchers of the nuclear physics institute were investigating the possibility of generalizing the concept of the racetrack microtron (RTM), that consists in a linear accelerator (linac) and two deflection magnets ( $180^\circ$  magnet, see figure 2.2). The bending magnets make the particles recirculate several times in the linac, and each time they gain energy. MAMI is developed to produce a continuous beam, with energies above 1 GeV and beam intensities starting from 1 nA up to 100  $\mu\text{A}$ .

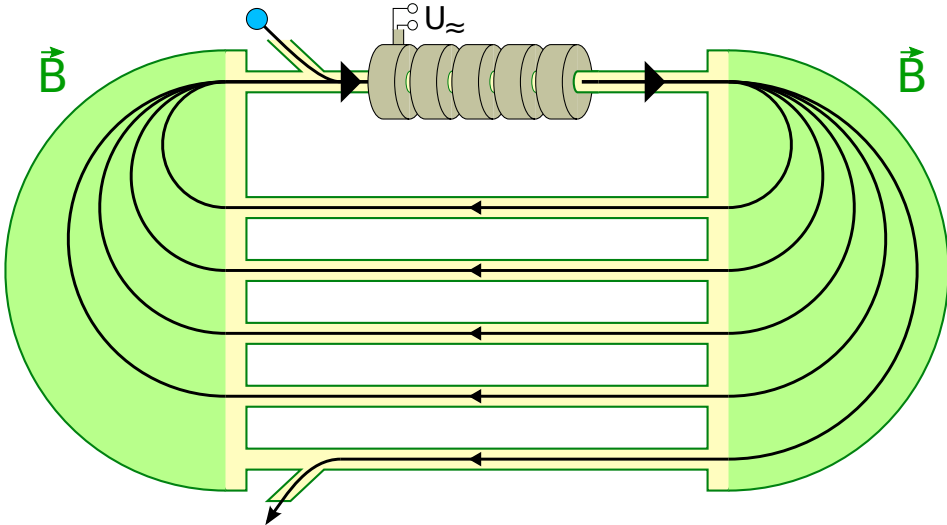


Figure 2.2: Racetrack Microtron. The particles are sent to the linac, and the two deflection magnets make the particles recirculate, until the momenta exceed the capability of the magnetic field.

A racetrack microtron is characterized by the energy gain per-cycle,  $\delta E$ , given by the high-frequency electromagnetic field (HF). The energy gain for a single acceleration cavity of the linac is:

$$\delta E = eU_{\text{Linac}} \cdot \cos(\phi)$$

---

<sup>1</sup>The electron beam is made by bunches of electrons, in sequence. In MAMI the separation between subsequent bunches is so small that it is not possible, with the available instrumentation, to distinguish it from a continuous flow of particles.

$U_{Linac}$  is the maximum voltage of the linac, and  $\phi$  is the phase of the beam relative to the maximum of HF. The beam consist in individual packets (bunches) of electrons, whose rate correspond to the frequency of HF. To be accelerated during each recirculation step, the electron bunches must arrive at entrance of the linac with the correct phase  $\phi$ . Therefore the electron time of flight per cycle must be an integer or a multiple of the HF period. The time of flight is made of two terms: the first is the time needed to travel in the magnetic field of two  $180^\circ$  bending magnets, equal to the cyclotron period; the second term is instead given by the straight sections, and remains constant for relativistic motion.

$$T = \frac{2\pi\gamma m_e}{qB} + \frac{L}{v} \quad (2.3)$$

where  $B$  is the magnetic field,  $q$  and  $m_e$  are the charge and mass of the electron, and  $L$  is the length of the straight section of the accelerator. The frequency is given by the formula:

$$f = \frac{qB}{2\pi\gamma m_e + \frac{LqB}{v}} \quad (2.4)$$

From these two equations two conclusion can be drawn:

- To accelerate slow electrons, with  $\gamma = (1, 10)$ , a magnetic field of 0.1 T is used, in order to work with frequencies of (2 GHz, 4 GHz), that are easy to control. However with higher energies, and with a small magnetic field, the bending radii is higher and uneconomical.
- For high energy electrons  $\gamma > 10$ , to reduce the size of the deflection magnets, it is useful to increase the magnetic field up to 1 T of more, with the same band of frequencies  $\simeq$  GHz.

This justifies the structure of MAMI: a cascade of microtrons to reach progressively higher energies, with the same acceleration frequency at each stage. In MAMI there is a sequence of 4 different microtrons, that are able to accelerate particle up to 1.6 GeV.

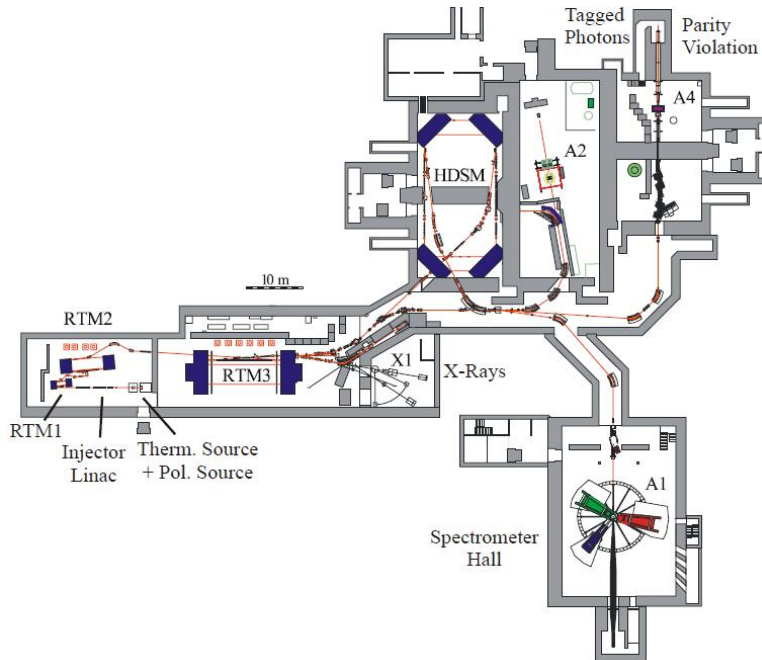


Figure 2.3: Scheme of the accelerator, with the different experimental halls. A third hall previously used for the A4 experiment, measuring the strange quark content of the proton, is now being used for the novel MESA accelerator and its experiments.

The first stage, shown in figure 2.3, is composed by two small microtrons. The first microtron, RTM1, accelerates the particles up to 14 MeV in 18 revolutions. Then the electrons are sent to the

RTM2, second microtron that can reach an energy of 180 MeV. After passing this first stage, the beam is directed towards the RTM3 (race track microtron 3), in the adjacent room, that is large microtron with an end point energy of 855 MeV. The sequence of RTM1, RTM2 and RTM3 forms MAMI-B, which is operating since 1990-91. A fourth stage, MAMI-C, was built and started operation in 2007. This fourth stage is made by 4 bending magnets, with a bending angle of 90°, and it is designed to achieve energies of 1.6 GeV. MAMI-C design is different from the other race-track microtrons, and it is not discussed, as it is not necessary for the experiment to reach such high energies.



Figure 2.4: Picture of the Racetrack RTM3 in MAMI-B. The Green square at the bottom is one of the deflector magnets, the other one is below the point where the photo was taken. The linac stage is on the left. The tubes at the center of the figure are the paths that the particle cross during the recirculation. The further away from the linac the greater the energy.

The operation principles of a microtron is simple to be described. First we consider the gyro-radius for relativist electrons of energy  $E$ , that is:

$$r = \frac{E\beta}{qcB} \quad (2.5)$$

To have a coherent conditions, we must have that the flight time  $\tau = \frac{\lambda}{c}$  of the first recirculation must be an integer multiple of the HF wavelength  $\lambda_{HF} = \frac{c}{f_{HF}}$ , as shown in equation 2.4. This means that:

$$\lambda = \tau c = \frac{2\pi cr}{\beta c} + \frac{Lc}{v} = \frac{2\pi E}{qB} + L = m\lambda_{HF}$$

For the subsequent recirculations, the flight-time at energies  $E_n = E_{n-1} + \delta E$  must be increased by an integer multiple of HF, too. This lead to a second equation:

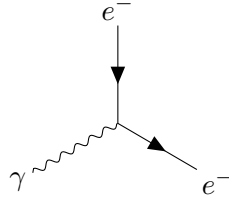
$$\frac{2\pi\delta E}{qB} = n\lambda_{HF}$$

The minimum gain per cycle is then determined only by the strength of the magnetic field and wavelength  $\lambda_{HF}$ . The system of these two equations controls the dynamic of the race-track microtrons, and determines the working point of the accelerator.

### 2.3.1 Polarized Beam

For the beam-normal single spin asymmetry a vertically polarized beam is necessary. At the MAMI electron accelerator it is possible to produce a vertically polarized beam with energy in the range 180 MeV – 855 MeV [22]. The procedure to orient the spin vertically is discussed in this section, and the measurement of the degree of polarization is explained.

The electron source used at MAMI is made by a strained GaAs/GaAsP super-lattice photo-cathode illuminated by circularly polarized light. To alternate the sign of the light polarization, a fast Pockels cell ([23]) is installed in the optical system of the electron source. The Pockels cell is a wave plate controlled by the electric field, that changes the helicity of the photons impinging on the electrons. A Pockels cell exploits the Pockels effect, that affects crystal with particular characteristics (lack of inversion symmetry). For this type of materials the refractive index is linearly dependent on the applied electric field. By controlling the refractive index, the polarization state of the incident light beam is altered. Since the angular momentum is conserved, the extracted electron carries the same helicity of the incoming photon:



$$(Jz)_\gamma = \pm 1 \quad (Jz)_{e^-} = \mp \frac{1}{2} \rightarrow \pm \frac{1}{2} \quad (2.6)$$

With the fast change of the Pockels cell it is possible to alternate the sign of the polarization. By the insertion of a  $\lambda/2$  plate between the laser system and the photo-cathode, the global polarization orientation of the electron beam can be reversed. This is useful because changes directly the sign of the asymmetry measured by the detectors, and allows to identify systematic errors. Usually, two sets of data are taken during an experiment, reversing the orientation of the  $\lambda/2$  wave plate. By comparing the results for the two sets of data, the influence of the optical system on the asymmetry measurement is estimated and is used to correct the final result of the asymmetry. However changing the orientation of the  $\lambda/2$  wave plate requires a certain amount of time and it is usually done for longer beam time. During the experiment described in this thesis, the  $\lambda/2$  wave plate orientation was fixed.

The beam degree of polarization achieved with the electron source is roughly  $P = 80\%$ . The degree of polarization reduces the measured asymmetry:

$$A_{measured} = P \cdot A_n$$

The electrons extracted by the circular polarized laser are longitudinal polarized. A combination of magnetic fields is needed to rotate  $\vec{P}$  from longitudinal to transverse orientation. For this purpose two devices are used: Wien filter and a double solenoid, located in the injection beam line, close to the the optical source, as show in figure 2.5

Looking at the picture, the longitudinal direction corresponds to the  $Z$  axis. The  $X$  axis is parallel to the second blue arrow, just after the Wien filter, and the  $Y$  axis is orthogonal to the page. The spin is initially rotated by  $90^\circ$  in the  $X$  direction, with the Wien filter; the subsequent double solenoid aligns the spin to the vertical direction, with another  $90^\circ$  rotation. Once the beam passes the double solenoid, the electrons go through the injector linac, the microtrons and arrive at experimental hall, where the target of the experiments is installed. During the acceleration stage, the spin follows the precession motion, as determined by the BMT equation, due to the various magnetic fields that they encounter during the travel. In our experimental setup, the magnetic field of the various bending magnets that constitute the microtron-cascade are always parallel to the polarization in vertical direction, so the cross product  $\vec{B} \times \vec{P} = 0$ , and the transverse polarization remains constant. Only the residual horizontal component precedes during the motion. For experiments with longitudinal polarization,

*bird's eye view*

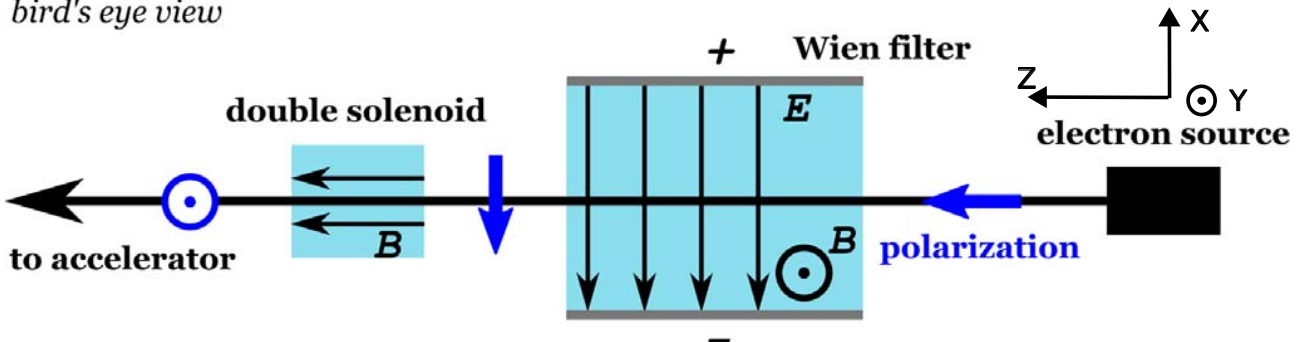


Figure 2.5: Beam line projection. This figure is taken from the paper [22]

after the first spin rotation of the Wien filter and the bending magnets, there is a further rotation determined by the motion of the particles during the acceleration and recirculation in the microtron. Considering this further contribution, the rotation made by the Wien filter is adjusted in such a way that the polarization has the correct alignment in the experimental hall. The rotation angles due to the various magnetic field are known from simulations and also directly measured for some energies: for a beam of 570 MeV the rotation angle is  $55^\circ$  with an accuracy of  $\pm 2^\circ$ . In our case, this further rotation has only a small effects on the residual horizontal component. This horizontal component is accurately minimized by MAMI operators at the beginning of the beam time, and its effects on the measurement are negligible.

MAMI was not developed for experiments with transverse polarization, so it is not possible to measure directly the transverse component. However the vertical polarization is deduced from the determination of the total beam polarization and the residual horizontal components.

### 2.3.2 Vertical Polarization Measurement

Three polarimeters are installed in MAMI: a Mott, a Møller and a Compton polarimeter. The Compton and Mott polarimeters are located before the injector linear accelerator (see figure 2.3), close to the beam source, where the 3.5 MeV electrons have gone through the Wien filter and the double solenoid. The Møller polarimeter, instead, is installed in the spectrometer hall, where the beam is delivered. The Møller polarimeter is sensitive to the longitudinal component of the polarization, while the Mott and Compton polarimeter are sensitive to the  $Z$  and  $X$  component. When the beam is polarized longitudinally, the total polarization is measured by the Møller polarimeter, in the spectrometers hall. The procedure for the polarization alignment is the following: at the beginning of the beam time the Mott polarimeter measures  $P_z$  for different settings of the double solenoid field, fixing the rotation angle of the Wien filter nominally at  $90^\circ$ . Changing the double solenoid field, the horizontal polarization component ( $P_x$ ) is minimized. A second minimization follows, using the Møller polarimeter and changing Wien filter rotation angles, leaving the double solenoid field fixed. In this way also the longitudinal component  $P_z$  is minimized. With the new Wien filter setting, another measurement is performed with the Mott polarimeter. With this procedure, the  $P_x$  and  $P_z$  components are completely minimized, and the beam polarization is parallel to the  $Y$  axis, in the end. At this point, the polarization is correctly aligned, and the experiments can start. The last polarimeter, the Compton, is not to obtain the vertical polarization, but can measure the variation of the degree of polarization during time, as explained in [22].

In the last measurement of  $A_n$  at MAMI [21] the Moller and Mott polarimeters were available. In this way, it is also possible to estimate the systematic uncertainty for the degree of polarization, which is the relevant contribution of the systematic uncertainty for the measurement of  $A_n$ . The value of systematic error for the previous experiment is about 1 ppm. For the experiment described in this thesis, the polarization was aligned to the transverse direction using only the Mott polarimeter, obtaining  $P = 0.79\%$ . The Møller polarimeter was not available, and we could not estimate the systematic uncertainty of the degree of polarization.

### 2.3.3 Mott Polarimeter

In this section we describe the theory of the Mott polarimeter. The Mott polarimeter exploits the asymmetry in the cross section due to the spin dependence. From the asymmetry we can measure the polarization of the beam. Let's suppose that we have an electron beam that is sent towards a nucleus of charge  $Ze$ . We know from theory [24] that the spin of the incident electron interacts with the electromagnetic field produced by the nucleus. The magnetic field seen by a particle with speed  $\vec{v}$  near a nucleus is:

$$\vec{B}_{nucleus} = \frac{-\vec{v} \times \vec{E}_{nucleus}}{c} = \frac{Ze}{mcr^3} \vec{L}$$

This magnetic field is coupled with the magnetic momenta of the electron  $\mu_e$ .

$$V = -\vec{\mu} \cdot \vec{B}_{nucleus} = \frac{Ze}{mcr^3} \vec{L} \cdot \vec{S}_{e^-} \quad (2.7)$$

The second equation represents the spin-orbit interaction potential. This term yields the polarization dependence of the cross section. Let's consider an incident particle that scatters from a nucleus at an angle  $\theta$ , as shown in the figure:

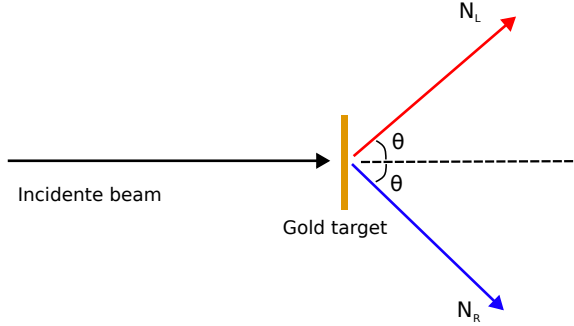


Figure 2.6: Scheme of the Mott scattering, the polarization is orthogonal to the plane,  $\vec{n} = \frac{\vec{k} \times \vec{k}'}{|\vec{k} \times \vec{k}'|}$ . The red and blue arrows represent two scattering events with the same  $\theta$ , but opposite  $\vec{n}$

The cross section can be modeled highlighting the dependencies on the polarization  $\vec{P}$ :

$$\frac{\partial\sigma(\theta)}{\partial\Omega} = I(\theta)[1 + S(\theta)\vec{P} \cdot \vec{n}] \quad (2.8)$$

In the equation above, the cross section is divided in two terms:  $I(\theta)$  represents the term that does not depend on the polarization, while the second term contains the dependence on the polarization, through is the Sherman function  $S(\theta)$ ; also called the asymmetry function [24]. The unit vector  $\vec{n}$  is normal to the scattering plane, and it is defined as:

$$\vec{n} = \frac{\vec{k} \times \vec{k}'}{|\vec{k} \times \vec{k}'|}$$

Where  $k$  and  $k'$  are the wave vectors associated with the incident and scattered electrons. The direction of  $\vec{n}$  is parallel to the angular momentum  $L$ , and depends on whether scattering is to the left or to the right. Let's suppose our initial beam has a polarization  $P$ , that can also be expressed as:

$$P = \frac{N_\uparrow - N_\downarrow}{N_\uparrow + N_\downarrow}$$

Where  $N_\uparrow$  and  $N_\downarrow$  are the number of electrons with spin up and spin down. The Mott polarimeter measures the number  $N$  of scattered electrons at a fixed angle  $\theta$ , in the two directions right and left

(figure 2.6). Using the equation (2.8), the scattered electrons to the left side  $N_L$  and to the right side  $N_R$  are equal to:

$$N_L = N_{\downarrow}[1 + S(\theta)] + N_{\uparrow}[1 - S(\theta)]$$

$$N_R = N_{\uparrow}[1 + S(\theta)] + N_{\downarrow}[1 - S(\theta)]$$

The asymmetry  $A(\theta)$  of the scattered electron between left ( $N_L$ ) and right ( $N_R$ ) is given by:

$$A(\theta) = \frac{N_L - N_R}{N_L + N_R} = \frac{N_{\downarrow}(1 + S(\theta)) + N_{\uparrow}(1 - S(\theta)) - N_{\uparrow}(1 + S(\theta)) - N_{\downarrow}(1 - S(\theta))}{N_L + N_R} =$$

$$= \frac{(N_{\uparrow} - N_{\downarrow})}{(N_{\uparrow} + N_{\downarrow})} S(\theta) = P \cdot S(\theta)$$

The last step of the equation gives the beam polarization in terms of  $A(\theta)$ , the asymmetry measured by the Mott polarimeter, and the function  $S(\theta)$ , the Sherman function. The Mott polarimeter in MAMI, installed after the double solenoid, measures the scattering asymmetry  $A(\theta)$  for electrons of 3.5 MeV with a thin gold target.

## 2.4 Experimental Hall Setup

MAMI experimental halls are named with the capital letter A followed with a number. In A2, for example, photo-nuclear reactions are studied to investigate the fundamental physics at the scale of nuclear dimensions. The experimental hall where the experiment described in this thesis is conducted is the A1 hall. We will describe briefly the main operating detectors that are installed and the details that are interesting for the transverse asymmetry measurement. In the A1 hall the beam is delivered with energy in a range starting from 180 MeV up to 1.6 GeV. Energy greater than 855 MeV are reached with the last acceleration stage HDSM, shown in figure 2.3. Because the electron energy of our experiment is 570 MeV, the beam passes only through the first acceleration steps, and is extracted from the RTM3 and directly sent to the A1 experimental hall, without going through the HDSM stage.

Inside the A1 hall three large magnetic spectrometers are placed on a circular rail-track around the target chamber (figure 2.7). They were designed and built in 1993 to perform high precision measurement of electron scattering in coincidence with other hadron detection, with high resolution in the determination of the particle momenta  $\frac{\delta p}{p} < 10^{-4}$ . The spectrometers develop vertically with a height of 15 m, and the scattered electrons and the other particles are deflected with respect to the scattering plane with the use of magnetic fields. The figure 2.8 shows the path of the particles scattered from the target. The spectrometers used for the transverse asymmetry measurement are the red and blue ones. There are multiple reasons why the particles are deflected in the vertical direction, that can be summarized in two points:

- reason of space: a horizontal setup would not fit in the dimension of the building; in addition this would not allow to rotate the spectrometers by a variety of angles
- reduce background and noise: in fact the high beam intensity at MAMI is a source of noise and background events which can be reduced by detecting the scattered particles away from the beam direction.

Once a particle is scattered in the acceptance region of the spectrometers, it is deflected by the magnetic field and passes through the drift chamber, which occupies the first third in height of the spectrometers. When the particle is at the height of the platform in the figure 2.8, it impinges on a layer of plastic scintillator, and after that a Cherenkov detector measures the particle speed  $v$ . In figure 2.9 the spectrometer A internal, taken during the installation of detector A, is shown. The determination of both the particle speed  $v$  and momenta (drift chamber) allows particle identification.

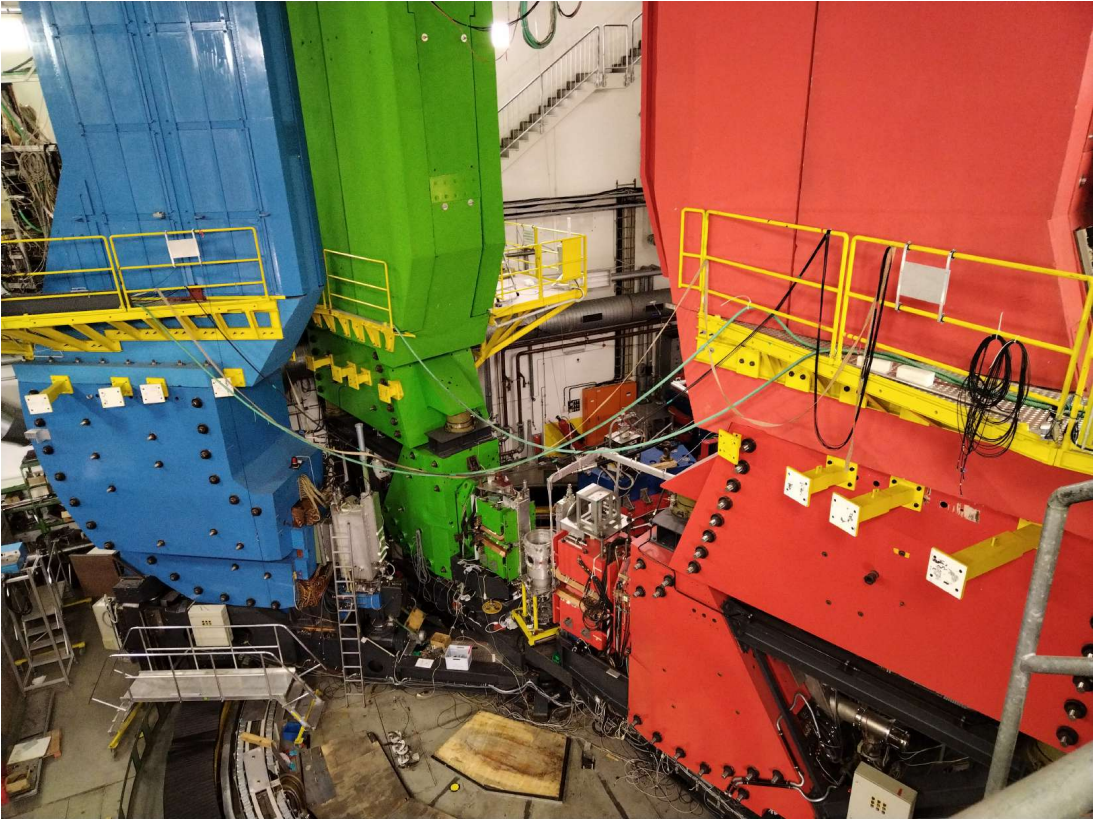
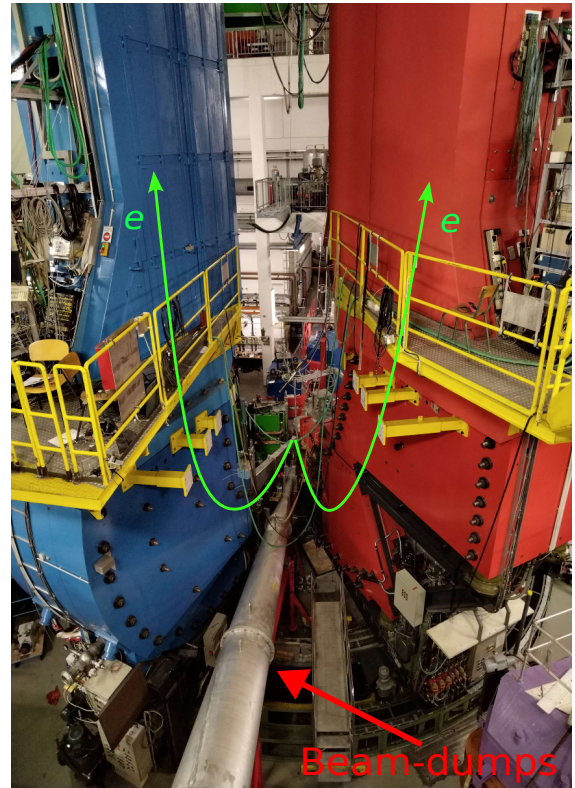


Figure 2.7: Picture of the A1 spectrometers hall, the spectrometers red and blue are used during this experiment. At the center of the picture is possible to observe the scattering chamber.

Figure 2.8: Image of the spectrometers of A1 hall. The spectrometers can be rotated using a system of rail-tracks that are visible at the bottom of the image. The electrons are scattered and then deflected in the vertical direction by the magnetic field (green lines). This picture is taken from behind the target. The target is roughly at the center of the image where the two green lines join. The electron are coming from the opposite direction, with respect to the spectrometers.



Despite the possibilities offered by the already existing setup, for the beam time of interest none of these components was used directly in the estimation of  $A_n$ . The reason is due to the high intensity of the beam that is used in the experiment, which is far from the optimal operating conditions of

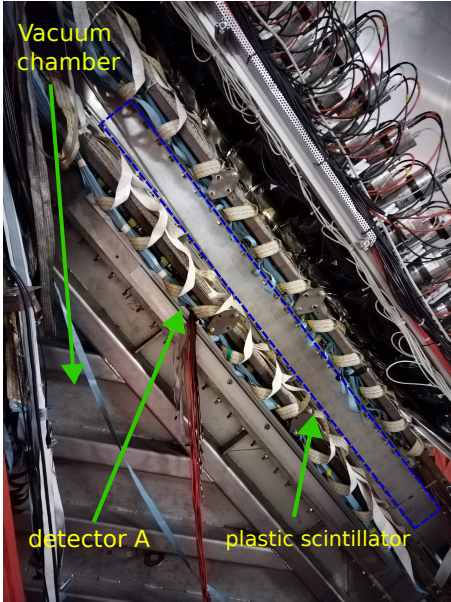


Figure 2.9: Internal of the spectrometer. This image was taken during the installation of the detector A inside the red spectrometer, that is accessible from the platforms visible in the picture 2.8

the components, that are suited for rates lower than the ones expected for beam normal single spin measurements (for carbon target 1 MHz, while for lead target 500 kHz). The spectrometers are used indirectly, for the alignment of scattered electrons to our detection system.

## 2.5 Detector Description

In this section we will describe the electronics and the detectors used to measure the transverse spin asymmetry. For this experiment we are going to measure the transverse asymmetry at one fixed angle, corresponding to a transferred momentum of  $Q = 0.2 \text{ GeV}$ . The electrons detection is made via two thin blocks of fused-silica that are coupled to PMTs. When a scattered electron hits the fused-silica (refractive index  $n = 1.45$ ) Cherenkov light is emitted. The emitted Cherenkov light can extract one electron in the photocathode, which will be amplified by the PMT dynode structure. This sequence of event triggers the PMT and produce an output signal.

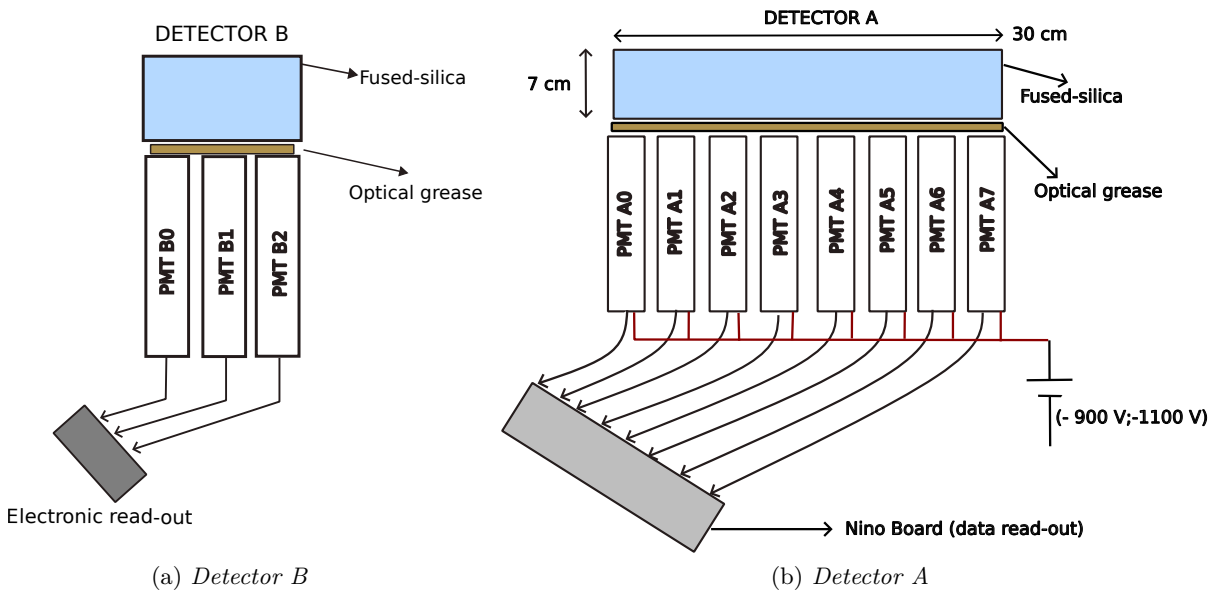


Figure 2.10: Detector A and B scheme. Each PMT is coupled to the same fused silica bar. The PMTs located at the edges of the fused-silica bars are expected to measure lower rates with respect to the PMTs located near the center. The output signals have negative voltage and are read out by the NINO board.

In the experiment two detectors are installed and read-out independently. The detector A is placed at an angle of  $+\theta$ , while detector B is placed at  $-\theta$ . We expect to measure the same absolute value of the transverse asymmetry, with an opposite sign due to the different orientation. The two detector are made by 3 PMTs and 8 PMTs coupled with two blocks of fused-silica, as shown in 2.10. These two detectors are placed inside the spectrometers presented in 2.8, between the top of the drift-chamber, which occupies the first third in height of the spectrometer, and just below the panel of scintillator. During the experiment, the drift chamber of the spectrometers is turn off, and also the PMTs coupled to the spectrometer scintillators are not powered. The scattered electrons will be detected only via the Cherenkov detectors in figure 2.10. As mentioned above, the scattered electron are deflected in the vertical direction by the magnetic field of the spectrometer. It is important to mention the differences between the new and the old electronic setup. In the old electronic setup the output signal of the PMTs was integrated during the time interval of each sub-event, and therefore the single scattered electron could not be counted. The advantage of this method is that the electronics is simpler. However, this old method is affected by a baseline noise and it is not good for the future experiments with lead target, where the expected rates are lower than the rates on carbon. With the new electronics, the single electrons are counted, and this will enable the future measurements with lead, improving the accuracy.

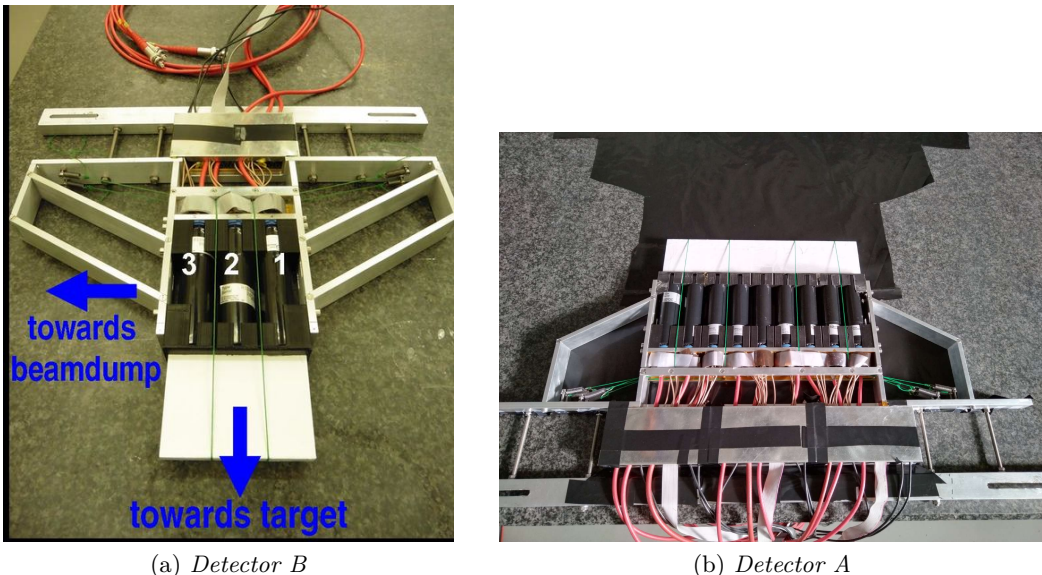


Figure 2.11: Picture of the two detector taken in the clean room. The white blocks are the fused silica bars that produces the Cherenkov light, the cylinders below are the PMTs, triggered by the passage of the particle.

Here we report the characteristic of the two detector that are relevant for the data analysis:

- detector B size:  $7 \text{ cm} \times 10 \text{ cm} \times 1 \text{ cm}$
- detector A size:  $7 \text{ cm} \times 30 \text{ cm} \times 1 \text{ cm}$
- Number of dynodes of the PMT: 12
- The Power voltage for the PMT in negative, in the range of  $(-900 \text{ V}, -1100 \text{ V})$
- refraction index  $n$  of the fused-silica is 1.45.
- maximum gain of  $22 \cdot 10^6$ .

The PMTs are coupled to the fused-silica with an optical grease suited for ultraviolet light. The PMTs positioned at the center of the fused-silica bar have an effective area coverage larger than the PMTs at the edge and their rates are expected to be higher compared with the other PMTs.

## 2.6 Beam Monitors

In MAMI, several monitors are placed along the beam line to check the beam quality and measure parameters such as current intensity, energy and relative position of the beam. This section summarizes the operating principles of the monitors installed at MAMI. For a complete description, refer to the following paper [25]. The monitors available at MAMI are constituted by resonant cavities. With the resonant cavities it is possible to measure the various quantities, with the underlying physical principle that the passage of charged particles through these cavities excites some electromagnetic resonant modes<sup>2</sup> (see figure 2.12) which can be detected and analyzed by an analog circuit, and related the beam parameters.

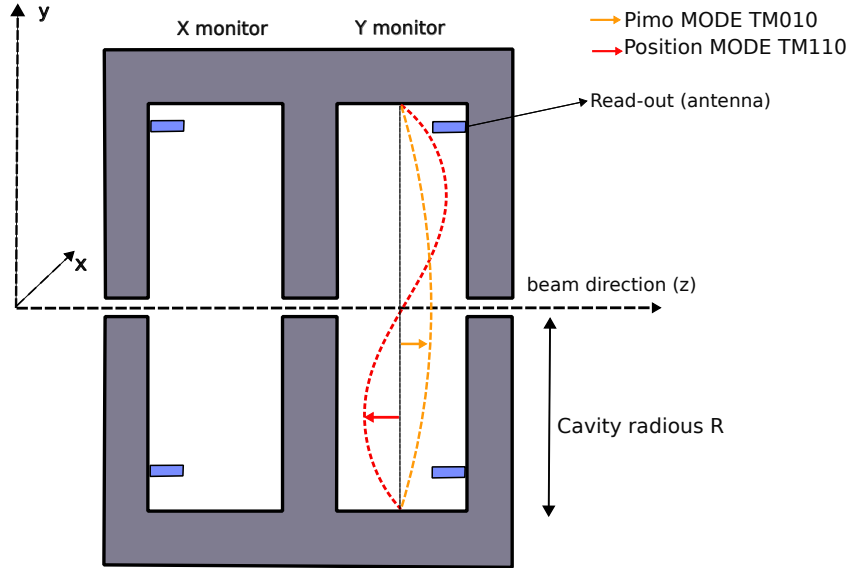


Figure 2.12: Scheme of the Cylindrical cavities installed at MAMI. In red we have the  $TM_{110}$  mode, used to measure the position of the beam, in yellow the  $TM_{010}$  mode, to measure the intensity of the beam.

Before going into the details, it is necessary to define some quantities that will be used later in the discussion. We define the shunt-impedance  $r_s$  as:

$$r_s = \frac{|V_{\parallel}|^2}{P} \quad (2.9)$$

Where  $P$  is the power absorbed by the cavity when a particle excites one of the resonant mode, and  $V_{\parallel}$  is defined as the effective voltage experienced by a charged particle along a straight line, which can be computed as:

$$V_{\parallel} = \frac{1}{q} \int_{s_0}^{s^1} \vec{E}_s \cdot d\vec{s}$$

The shunt impedance is a measure of the interaction strength between a cavity and a charged particle, and can also be expressed using the  $Q$  value of the cavity, the maximum energy stored  $W$  and the frequency of resonance  $f_r$ :

$$r_s = \frac{|V_{\parallel}|^2 Q}{2\pi f_r W}$$

When the beam travels through the cavity, the particles lose energy that excites the mode. The power  $P_{HF}$  extracted from the beam is related to the beam current:

---

<sup>2</sup>TM mode, where the magnetic field is completely transverse respect to particle momenta

$$P = i^2 r_s \quad (2.10)$$

Where  $i$  is the beam current. An antenna is used to decouple part of the energy from the cavity and send it to a circuit which produces an analog output signal. Indicating with  $\kappa$  the coupling constant of the antenna, the previous relation needs to be modified introducing a new factor  $\frac{\kappa}{(1+\kappa)^2}$ . In a cylindrical resonator, the type installed at MAMI, the resonance frequencies of the different oscillation modes are expressed by the formula:

$$f_{m,n,p} = \frac{c}{2\pi\sqrt{\epsilon_r\mu_r}} \sqrt{\left(\frac{x_{m,n}}{R}\right)^2 + \left(\frac{p\pi}{L}\right)^2}$$

The constant in the formula are:

- $c$  is the light speed.
- $\epsilon_r, \mu_r$  are the magnetic and dielectric constant of the material.
- $x_{m,n}$  it the n-th zero of the m-th Bessel function.
- $R$  and  $L$  are the radius of the cylindrical cavity and his length.

This formula can be obtained solving the Maxwell equations with cylindrical boundary condition. If the frequency of the beam bunch is equal to the resonant frequency  $f_{m,n,p}$  of the cavity, a TM mode is excited. At MAMI high quality monitors are installed, with a  $Q \simeq 10000$ , implying that  $\frac{\delta\nu}{\nu} \simeq 10^{-4}$ . This means that the frequency of the beam bunch must be very close to the frequency of the resonant cavity. At MAMI the frequency used for all the resonators is 2.449 532 GHz or a multiple of it. The beam bunch frequency is the same, and it is controlled by the MAMI-master oscillation signal, that is the reference signal for all the MAMI monitors. Depending on the  $TM$  mode excited, we have a different signal in the cavity, so a different signal collected by the antenna. The relevant quantity that is detected is the power  $P_{HF}$  absorbed by the antenna, that is proportional to the power loss  $P$  of the beam. For the  $TM_{010}$  mode, the power absorbed by the antenna is:

$$P_{HF} = i^2 r_{010} \frac{\kappa}{(1+\kappa)^2} \quad (2.11)$$

Where  $\kappa$  is a coupling constant between the electromagnetic field of the cavity and the antenna. The power absorbed by the antenna is directly dependent on the beam current. With the beam current in the range of 1 nA to 100  $\mu$ A, the output power ranges from pW to mW. Therefore the signal is processed in close proximity of the installed monitors. In the signal processing, the input signal of the antenna is coupled to the master-oscillation signal, so the output signal is given by the formula:

$$U = \sqrt{P_{HF}} \cos(\phi - \phi_{LO}) \quad (2.12)$$

where the phase  $\phi$  is the phase of the resonant mode or the phase of the beam bunch, while the phase  $\phi_{LO}$  is the phase respect to the master-oscillation signal, and can be adjusted by a phase shifter in the circuit. The output voltage signal can be read out with the oscilloscope or digitalized and saved with other devices. To measure the beam intensity is important to minimize  $\phi - \phi_{LO}$  (see figure 2.13), to maximize the signal amplitude.

The measurement of the  $x, y$  position follows in principle the same procedure. In this case the  $TM_{110}$  is acquired, because for this mode the  $r_{shunt}$  is proportional to the beam position on the  $x, y$  plane. The power absorbed by the antenna can be written:

$$P_{HF} = i^2 r_{110} \frac{\kappa}{(1+\kappa)^2} Kx^2 \quad (2.13)$$

The output signal, that is read by our setup, is proportional to the square root of the absorbed power:

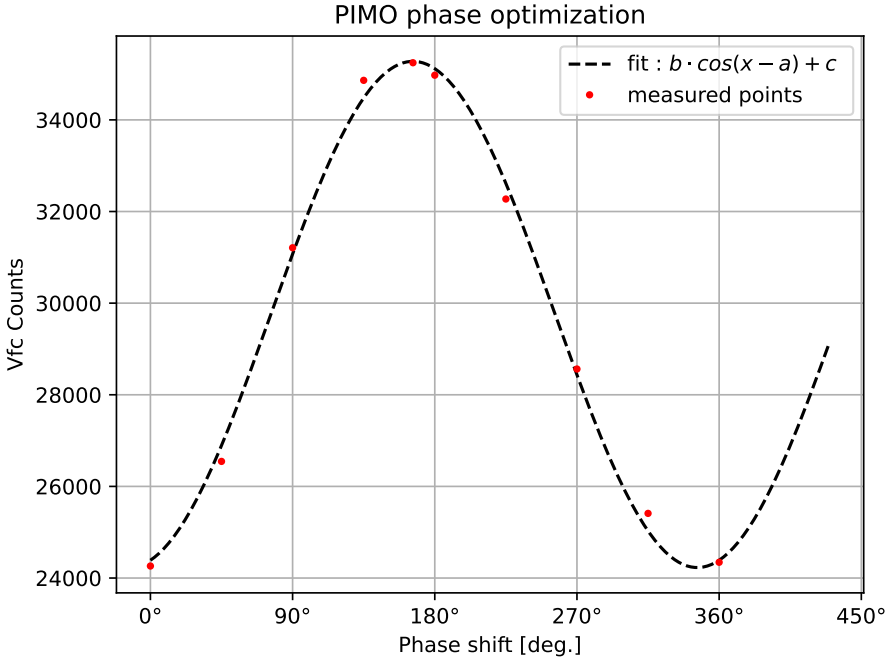


Figure 2.13: Plot of the output signal versus phase  $\phi$ . The phase optimization was done selecting the working point in correspondence of the peak.

$$U = \sqrt{P_{HF}} = \text{constant} \cdot i \cdot x \quad (2.14)$$

The beam parameter are obtained by inverting the above formula

$$x \propto \frac{\sqrt{P_{HF}}}{i} \quad (2.15)$$

Where the exact conversion coefficients are not known, and are determined during the calibration phase, at the beginning of the beam time. To measure the beam energy, a different approach is used. The energy monitor (ENMO) consists of 2 cavities in the RTM3. One is located in the last recirculation pipe, the other one on the part of the beam line, where the acceleration takes place. The two monitors are synchronized to the master oscillation and measure the phase of the bunches of electrons. During their travel from the first cavity to the second cavity, the beam passes through the magnet and does one half turn. If the energy is slightly higher, the radius of the turn will be slightly larger. This means that there is an extra time between the two bunches, that can be measured as a small phase shift in the 570 MeV recirculation. From this it is possible to obtain a value for the difference of the actual energy from the nominal energy.

### 2.6.1 Beam stabilization

The beam stabilization is an essential component of the experiment. The values of  $A_n$  that we want to measure are in the order of 10 ppm, so it is important to reduce other contributions that can be related to variations in the beam parameters. The beam stabilization at MAMI is achieved with a control program. The beam monitors constantly measure the beam parameters and the control program receives the measurements from the monitors and calculates consequently the corrections to be performed. The beam position in the transverse plane is constantly adjusted by the magnets in the beam line. For the beam current and energy, the control program acts on the laser of the beam source and the klystrons in the three racetrack microtrons described in section 2.4. Two types of stabilization are made by the control program: the first is made to avoid long term drifts by pulling back the beam back to nominal conditions every  $\simeq 10$  s. Simultaneously, a fast stabilization prevents fast fluctuation, reacting quickly to every disturbance of the beam.

## 2.7 Electronics

### 2.7.1 Voltage to Frequency Converter

Some beam parameters are needed in order to take into account possible effects in the measurement of the transverse asymmetry. The relevant data are the position in the  $(x, y)$  plane, the incident angles on the target, the current and energy of the beam. All these values are collected using the existing monitors. To collect the data from the monitors, single and multichannel, synchronous voltage-to-frequency converters (AD7742) are used. These devices contain an analog modulator that is able to convert the input voltage into an output pulse train, whose frequency is proportional to the input voltage.

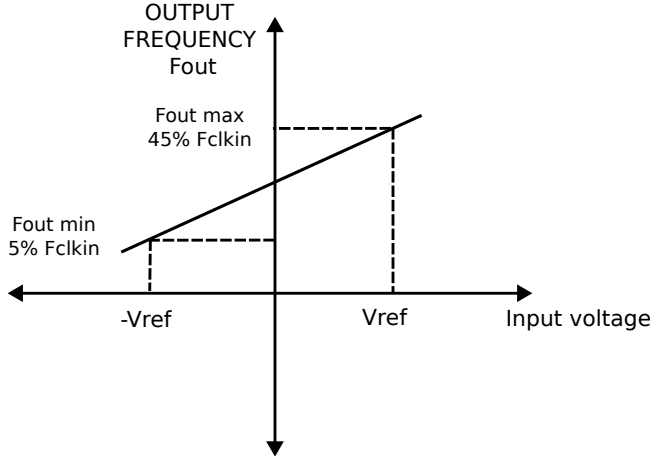


Figure 2.14: Frequency versus Voltage

The VFCs are powered with an external voltage of 5 V. They measure an input voltage in the range of  $(-V_{ref}, V_{ref})$ . An external clock signal, with a frequency  $F_{CLKIN} = 5.88 \text{ MHz}$  is created externally and synchronous to the gate-length. The analog input signal is sampled with by a switched capacitor, with a rate that is equal to  $F_{CLKIN}$ . The comparator produces a certain number pulses, and the frequency of the output signal is proportional to the input voltage, with  $-V_{ref}$  equal to  $5\% \cdot f_{CLKIN}$  and  $+V_{ref}$  equal to  $45\% \cdot f_{CLKIN}$  [26] (see figure 2.14). The data are acquired counting the number of pulses from the comparator, which are proportional to the frequency, so we can substitute to  $f$  the number of pulses, and we end up with the equation 2.16

$$V_{in} = V_{ref} \left[ 2 \cdot \frac{N_{pulses} - 5\% N_{CLKIN}}{40\% N_{CLKIN}} - 1 \right] \quad (2.16)$$

### 2.7.2 Master Board

The VFCs described in the previous section are measuring the beam parameters along the beam line. A figure of the beam line is in section 3.3.2, where the various position of the monitors is shown. The data collected by the VFCs are firstly acquired by the master board, in figure 2.15, and then sent to the A1 computer, which will produce the data package. The VFCs are synchronized by the master board clock, with a frequency of 5.88 MHz. This is also the reference frequency for the VFCs output signal.

The *onewire* is a special bus which will be used in future for temperature measurement in the VFC, to check if there are temperature drift and effects on the outputs signals. The master board sends also the gate length signal to the MAMI source, where the polarized beam is generated, and to the detectors, needed to communicate and synchronize the sub-events. For the experiment with the lead target, the master board will also control one of the magnets (*wobbler 16*, in figure 3.6). With the lead target, the beam position must be constantly changed so that the beam hitting point on the target varies continuously, to avoid melting. The master board is synchronized to the power grid,

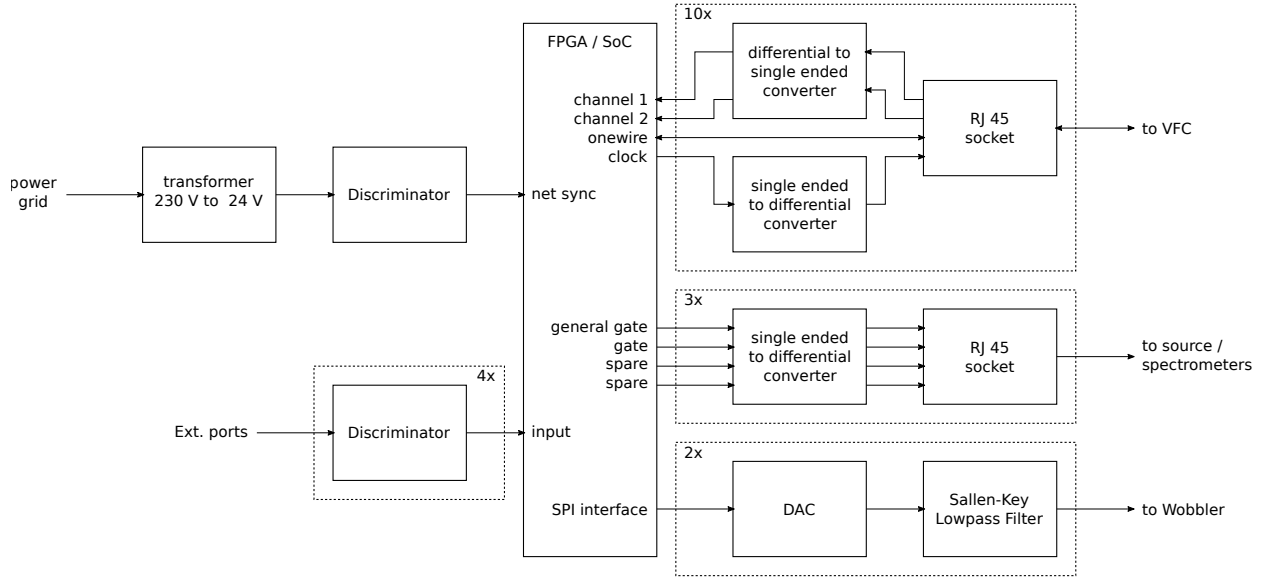


Figure 2.15: Scheme of the master-board, the device that coordinates all the electronics for the experiments, and send the data to the computer in the control room.

is order to reduce possible systematics effect connected to the 50 Hz frequency, as discussed in section 2.1.

### 2.7.3 Nino Board

The NINO board shown in figure 2.16 is our data acquisition system for the PMT counts (see paper [27]). It is made by 32 analog input channels and it is powered with  $\pm 5$  V. Each input channel receives a differential signal from the detector, and has an attenuation circuit that reduces the amplitude of the input signal. After passing the attenuator, the signal is sent to the input stage of the NINO chip, a current-to-voltage converter, that produces an output signal whose pulse-width is proportional to the total charge of the input signal.

After passing the input stage, the signal goes through a block of 4 cascaded operational amplifiers that act as a discriminator with a programmable threshold. The NINO chip can handle signals coming from 8 different channels and there are 4 NINO chips on each NINO board.



Figure 2.16: Nino Board, The input channels are at the bottom of the figure.

The signal that arrives to the discriminator is proportional to the input charge of the signal coming from the detector, so in the end the NINO board is sensitive to the input charge. The discriminator threshold can be set in the range of (10 pC, 100 pC). The output signal after the discriminator and the amplification block is a LVDS (low voltage differential signaling) with a fixed shape, and a width that is proportional to the input charge. Regarding the data acquisition system, two values are import to control the discriminator threshold and the attenuator, and are named *Thr* and *Att*, respectively. The NINO chip is designed in such a way that the *Thr* value is shared by 4 adjacent channels. On the contrary each channel has its own value of *Att*. Acting simultaneously on *Thr* and *Att* is possible to define a global threshold for each channel, individually. These two parameters are set in the DAQ program, using 12 bit DACs, corresponding to an interval of (0; 4095). *Thr* selects the threshold of the discriminator. The *Att* value controls the input voltage of attenuator: the higher is the value of *Att*, the lower is the attenuation of the signal. Two Nino board are used in the experiment, one for detector A and one for detector B. For the experiment discussed in this thesis, we will use only 8 channels for detector A and 3 channels for detector B, since this is the number of the input signals coming from the two detectors. For the future experiments more channels will be used, splitting the analog input signal in 4, and sending it to 4 different input channel of the board. This is useful because changing individually the attenuation value, we can define 4 different thresholds for the same signal and compare different values of threshold, to study how the noise affects the measurement, finding the best compromise between signal to noise ratio. The *Thr* and *Att* selection is explained in chapter 3.

# Chapter 3

# Detectors Test, Alignment and Calibration.

In this chapter we discuss the electronic test that have been carried out in the laboratory, and the calibrations needed in order to calculate, from the raw data, the quantities needed for the analysis. The test in the lab consisted in checking the photo-multipliers tubes and the data acquisition electronics. The calibrations consist of determining the scaling factors required by the analysis program, to convert the raw data collected by the *VFCs* to data in physical units. The important beam parameters are the impact point coordinates of the beam  $X, Y$ , the beam energy  $E$ , the beam current  $I$  and the scattering angles  $\theta_x$  and  $\theta_y$ . In the end, we discuss the auto-calibration procedure, which eliminates undesirable effects caused by the presence of an offset in the PMTs counts.

## 3.1 Nino Board

In this section we study the characteristics of the Nino board, which digitizes the signal from the PMTs. The NINO board has two parameters: *Thr*, that controls the discriminator and *Att*, which controls the attenuator circuit. These parameters are part of the settings of the DAQ program which controls the NINO board. Because the values of *Thr* and *Att* are defined in arbitrary units, it is desirable to find a conversion formula to obtain the value of the threshold in physical units, as mV. Because of the NINO sensitivity to the input charge, it is not simple to define a unique value for the threshold in mV, because the input charge of the detector signal depend on the shape, amplitude and time length. For example, signal with a large time and a small amplitude can generate the same charge with respect to narrow signal with high voltage amplitude. Despite this, some data have been acquired by the A1 collaboration, with which it is possible to define a raw conversion function from attenuation units to threshold. The idea behind is to generate, with a wave generator, signals with fixed time length and shape, varying only the amplitude, and use them as input of the NINO board. The data available were collected following this procedure. Unfortunately, these data were taken with an input signal shape that different from the signal shape of our experiment. We are aware that the conversion formula obtained with these data is only a rough estimation, however it can be useful to get an idea of the threshold values, in mV.

The data shown represent the values of the amplitude of the input signals (in mV) versus the values of *Att*, and are taken for a fixed value of  $Att = 750$ . The function used for the conversion is obtained from the fit of the data, the function used is the following:

$$Threshold \text{ [mV]} = \frac{a}{(att - b)^3} + c \quad (3.1)$$

The parameters of the formula are estimated using the function *curve-fit* of the python library *scipy*:

- $(a = -802.1 \pm 1.1) \cdot 10^6 \frac{\text{mV}}{\text{[arb.unit]}}$
- $b = 282.51 \pm 0.06 \text{ [arb.unit]}$

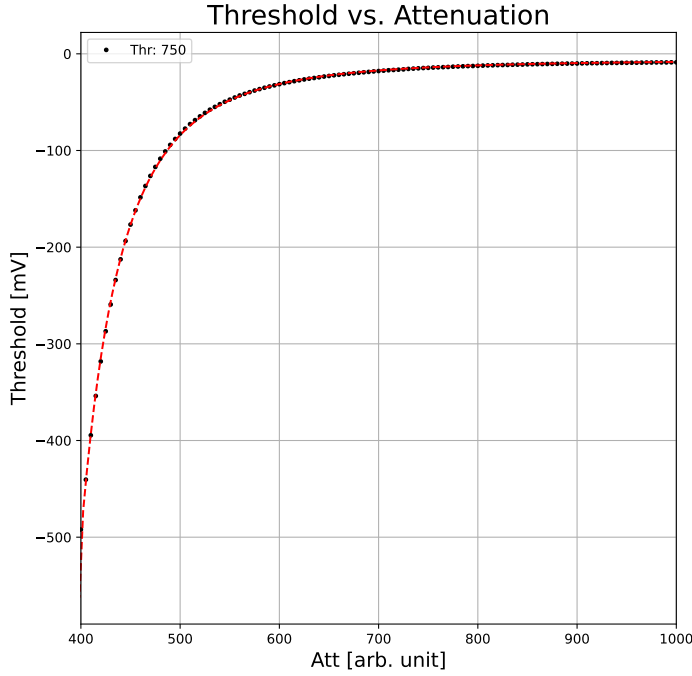


Figure 3.1: Threshold dependence versus attenuation. The input signals have a fixed shape and time length. The data are collected following this procedure: with a fixed amplitude of signal, the  $Att$  is set to 4000, the maximum, and decreased progressively, until the NINO board starts missing some pulses. All the data are acquired with a fixed value of  $Thr = 750$ .

- $c = -6.147 \pm 0.009 \text{ mV}$

As we can see, the relation between threshold and  $Att$  is not linear. Around the values 400 - 700 we observe large variability. For values higher than 700, the threshold is low and almost constant. This mean that the attenuation, controlled by the attenuator in the input channel of the NINO board, is reduced progressively as  $Att$  increases.

### 3.2 Detector Test

Before the beam time, some test with the two detectors were performed, to check that the PMTs were still working after some years of inactivity, and that the new electronics was able to count properly the pulses and store the data. For this studies, we didn't have a radioactive sources to employ. Anyway the signal shape using radioactive sources is expected to be different from signal of the 570 MeV electrons used in the experiment. The typical energies of nuclear decay are in the order of  $E \simeq 1 \text{ MeV}$ , with consequently only a small production of Cherenkov light, difficult to detect. A different approach is followed, using cosmic rays rate as a probe. The cosmic rays are able to produce Cherenkov light in the fused-silica bars, since the refractive index is  $n = 1.45$ , and a particle emits Cherenkov light when its  $\beta = \frac{v}{c}$  is more than  $\frac{1}{n} = 0.69$ . The principal component of the cosmic rays at sea level is made by muons, produced in the electromagnetic and hadronic showers in high atmosphere. The energy of the muons reaching sea level is about 4 GeV,  $\beta$  for these particles is:

$$\beta_\mu = \frac{p}{E} = \frac{\sqrt{E^2 - m_\mu^2}}{E^2} \simeq 0.99 \quad (3.2)$$

The muons are relativistic and their speed is over the threshold for Cherenkov light production. Knowing that the expected number of event for cosmic rays is about  $1 \frac{\text{event}}{\text{cm}^2 \text{min}}$  we can compute the expected values for the number of events. We decided to take 1 minute long acquisition for both the

two detectors, this leads to 70 expected events for detector B and 210 events for detector A. These values are a rough estimate, because the effective area seen by each PMT is less than the total area of the fused-silica bar. The rates measured in the laboratory are  $\simeq 60$  for detector B and  $\simeq 100$  for detector A. The first step is to select a good work point for the threshold. So, fixing the value of the threshold parameter for the NINO board, we took several acquisitions, each of them one minute long, increasing the attenuation (figure 3.2). We powered the PMTs with a negative voltage around  $-1000$  V, as suggested in the data-sheet, and covered the Cherenkov detector with a shielding blanket, to avoid ambient light simulating a signal.

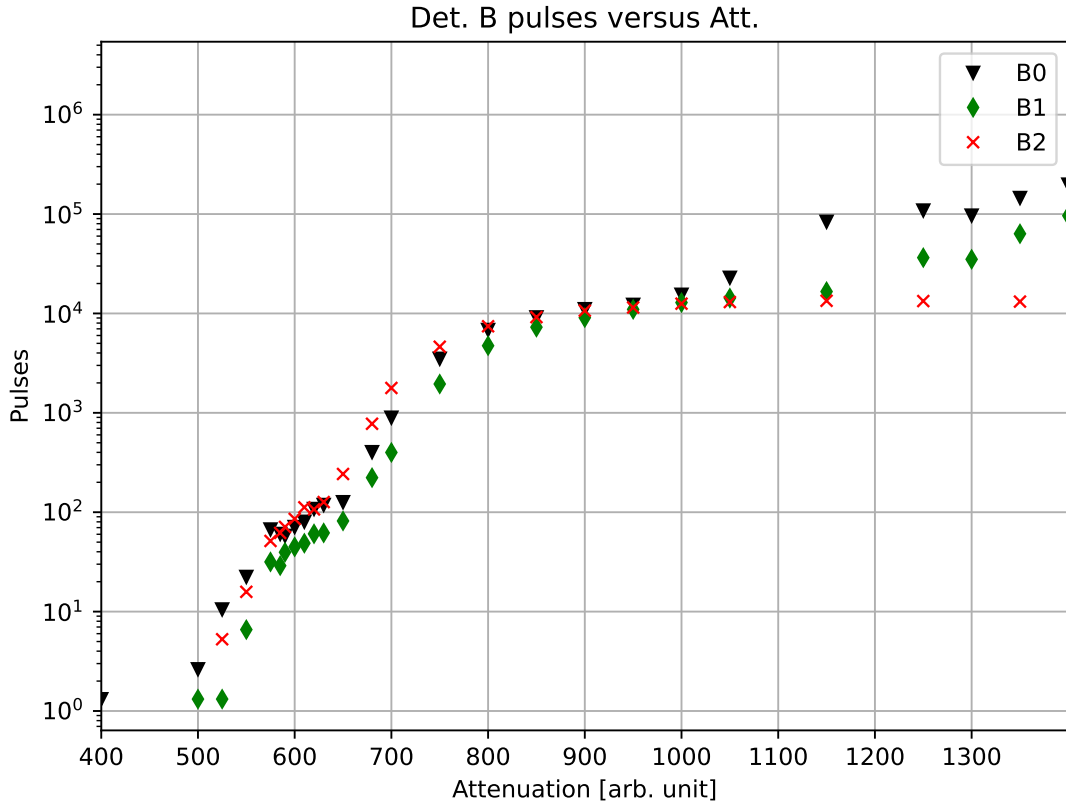


Figure 3.2: Attenuation scan for Detector B.

We observed a small knee, around the zone of  $580 - 600$  of  $Att$ , where the number of counts was almost constant, roughly equal to the number of expected events from muons hitting the detector. Then we observe a big edge for attenuation = 700. Looking at the plot 3.1, we assume that the attenuation values are so high that electronic noise is no longer rejected, in fact the counts grow enormously. The  $Att$  was set at 600 as a starting point for the experiment. Once the attenuation is set, we have studied the statistical fluctuation of the counts. 10 acquisitions, each of them 1 min long are collected and reported in table 3.1.

These data are interesting, we can check if the counts are following the theoretical distribution of the events expected for cosmic rays at sea level. If the PMTs are working well, we know that the number of counts should be Poisson-distributed:

$$Pdf(\mu, k) = \frac{\mu^k}{k!} e^{-\mu} \quad (3.3)$$

The variance of the Poisson distribution is equal to the mean of the counts, and we expect the same behaviour also for the sample mean and the sample variance, the values are computed and reported in table 3.2

We report also the correlation  $C_{ij}$  between the PMTs. The result are fine: we are able to see a positive correlation between adjacent PMT, and as expected the correlation is lower in the case of the more distant. This is explained by the lower probability that the photons of Cherenkov radiation

$n^{\circ}$ acquisition	B0	B1	B2
1	58	60	62
2	62	55	59
3	61	59	70
4	73	66	70
5	68	66	56
6	59	52	64
7	69	74	77
8	48	49	57
9	70	54	58
10	60	61	66

Table 3.1: Detector B counts for 10 acquisition of 1 min long, with  $Att$  equal to 600.

PMT	$\mu$	$\sigma^2$	Correlation $C_{ij}$
1	62.8	54.4	$C_{11} = 0.66$
2	59.6	57.2	$C_{23} = 0.65$
3	63.9	47.0	$C_{13} = 0.35$

Table 3.2: Mean, variance and correlation coefficient for detector B and PMT in overlap.

light up at the same time PMTs that are far away from each other. We can test that the data follow a Poisson distribution using the well-known Gosset test, defined as:

$$\chi^2_{n-1} = \sum_{i=1}^n \frac{(Obs_i - Exp_i)^2}{Exp_i} \quad (3.4)$$

where  $Obs$  are the observed counts, and  $Exp$  are the expected counts. We report the results for detector B in table 3.3. The test shows that there is good agreement with the hypothesis that the counts are Poisson-distributed.

Pmt:	1	2	3
$\chi^2_9$	8.52	8.45	6.37

Table 3.3: Gosset test for detector B

At this point, to convince oneself that the detector B is measuring signals given by the passage of cosmic rays, and not only noise, a fourth PMT (a spare component left in the lab) was used. This other PMT was coupled to a small block of fused silica ( $5\text{ cm} \times 5\text{ cm}$ ), and was placed in overlap with detector B, roughly in correspondence of B2. A first check was to look for coincidence signals at the oscilloscope, between detector B and the PMT in overlap.



Figure 3.3: Coincidence signal between PMTs B0 and B2 acquired with the oscilloscope.

Then we have acquired 10 acquisition one minute long, as before, measuring the counts of detector

B and a PMT in overlap. Unfortunately, the DAQ is not designed to take coincidences, so a different procedure was followed to check if the PMTs are triggered by the same passage of particles. The correlation coefficient between the PMT in overlap and the detectors is a good statistic for this purpose: if a positive correlation between the counts is observed, then a certain number of signals is triggered by the same passage of particles. The result for detector B are reported in table 3.4:

<i>n</i> <sup>o</sup> acquisition	B0	B1	B2	<i>Ov</i>
1	63	57	72	28
2	55	51	64	18
3	62	53	75	27
4	71	62	75	33
5	68	59	49	23
6	57	55	63	18
7	70	64	64	24
8	50	69	69	25
9	65	62	62	19
10	74	71	77	28

Table 3.4: Detector B counts for 10 acquisitions of 1 min long, with PMT *Ov* in overlap.

The sample mean, the variance and the correlation between the detector B and the PMT in overlap are reported in table 3.5. The result for the Gosset test are reported in table 3.6.

PMT	$\mu$	$\sigma^2$	Correlation
1	63.5	58.9	0.49
2	60.3	43.3	0.38
3	67.0	71.1	0.65

Table 3.5: Mean, variance and correlation coefficient for detector B and PMT in overlap.

A positive correlation is measured for all the PMTs of detector B. This indicates that a certain amount of signal are detected simultaneously.

	B0	B1	B2	PMT in overlap
$\chi^2_9$	8.95	6.44	10.96	9.52

Table 3.6: Gosset test for detector B and the PMT in overlap, for the 10 acquisition in table 3.4

The same procedure was followed also for detector A (see figure 3.4). We analyzed 4 signal at a time, because during these lab test we had only one NINO board, with only 4 channels available. The tests for the set of PMTs (A7,A6,A5,A4,A3) showed good result: the distribution of the counts was in agreement with the expected and the correlation coefficient between nearby PMTs and the PMT in overlap was different from zero and positive. For the set of PMTs (A2,A1,A0), some issues have emerged. Primarily the counts did not vary during the scan in *Att* and this has made impossible to identify a value for the *Att*. To study the behaviour of the counts, once again 10 acquisitions were acquired, and are reported in table 3.7.

$n^\circ$	acquisition	A2	A1	A0	$Ov$
1		91	51	50	27
2		86	61	50	7
3		58	48	45	18
4		95	62	41	29
5		69	60	50	21
6		85	57	45	19
7		66	51	46	28
8		74	51	48	22
9		77	43	45	17
10		62	44	50	29

Table 3.7: PMTs A2,A1,A0 counts for 10 acquisition of 1 min long.

The mean, variance and correlation between the PMTs counts is reported in table 3.8:

PMT	$\mu$	$\sigma^2$	Correlation
2	76.3	160	$C_{21} = 0.55$
1	52.8	47.5	$C_{10} = -0.10$
0	47.0	9.6	$C_{20} = -0.22$
$Ov$	21.7	48.2	

Table 3.8: Mean, variance and correlation coefficient for detector A and PMT in overlap.

The variance  $\sigma^2$  for A0 and A2 are quite different from the expected mean  $\mu$ . The Gosset test for this data are reported in table: 3.9

Pmt:	A2	A1	A0	PMT in overlap
$\chi^2_9$	19.6	8.30	1.90	39.5

Table 3.9: Gosset Test for PMTs A2,A1,A0 of detector A.

The expected error for the result of this test is  $\sigma = \sqrt{2 \cdot (n - 1)} \simeq 4$ . In this case we are observing 3 values that are more than  $3 \cdot \sigma$  far from the expected value. If we look at the correlation matrix :

pmt:	$Ov$	0	1	2
$Ov$	1	-0.18	-0.21	-0.06
0	-0.18	1	-0.10	-0.22
1	-0.21	-0.10	1	0.56
2	-0.06	-0.22	0.56	1

Table 3.10: Correlation coefficient between the PMTs (A2,A1,A0) and the PMT in overlap.

We observe negative correlation between the pmts, something not expected. After some investigations, we find out that the program which controls the NINO board had a bug: the program partially overwrote some detector B settings for detector A as well. Since detector B has only three pmt's, the problem affected the PMT's with the same numbering as detector A. After fixing this issue we repeated the same test, without finding any problem.

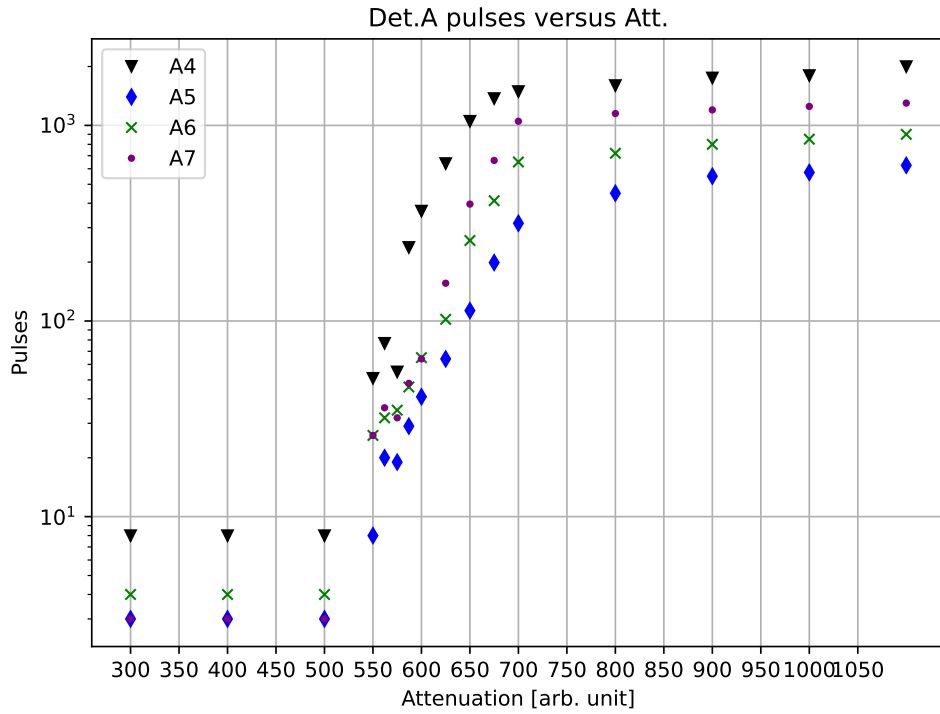


Figure 3.4: Attenuation scan for Detector A, for the pmt 4-5-6-7

### 3.3 Calibration

For the transverse asymmetry on  $^{12}C$  represent an ideal test for the new electronic system. Previous measurements of the  $A_n$  have been performed at MAMI for carbon target ([21]). For this experiment, the red spectrometer is placed at the angle of  $+22.5^\circ$ , and the blue one at  $-22.5^\circ$ , with respect to the longitudinal direction. For these two angle, we have the same kinematics and  $Q^2$  values of the previous measurement. The  $Q^2$  value was measured for a low current beam ( $I = 5\text{ nA}$ ) with the spectrometers detectors. The  $Q^2$  values are reported with and without rejecting the inelastic scattered electrons. The inelastic scattered electrons are rejected imposing an energy threshold.

det. <i>A</i> :	$Q^2 = 0.041 \text{ GeV}^2$	without Cut
det. <i>A</i> :	$Q^2 = 0.039 \text{ GeV}^2$	with Cut
det. <i>B</i> :	$Q^2 = 0.041 \text{ GeV}^2$	without Cut
det. <i>B</i> :	$Q^2 = 0.041 \text{ GeV}^2$	with Cut

The  $Q^2$  values are the same of the last measurement performed at MAMI, and are measured with and without rejecting the inelastic electrons.

#### 3.3.1 Alignment of the Scattering Plane.

The scattered electrons are deflected upward by the magnetic field inside the spectrometers A and B. However, the spectrometer detectors and systems are not directly used to measure the transverse asymmetry, due to the high current intensity, which would damage the electronics. Consequently, the scattered electrons are measured by the detectors A and B, described in section 2.5, which are installed between the drift chamber and the scintillator panel (see figure 2.9) of the spectrometers. At the start of the experiment, the scattered particles must be aligned to the fused-silica bars. This procedure is performed using a low current mode of the beam ( $I = 5\text{ nA}$ ). For this mode the spectrometer systems can be used to detect the particles. Since the position of our detector A and B inside the spectrometers is known, we can use the Cherenkov detector to visualize where the electrons. Changing

the configuration of the magnetic field, the electrons trajectory is oriented in such a way that is intersects the detectors A and B. For detector A the scattered electron beam has been aligned to pass over the fused silica in correspondence of PMT A7, therefore this PMT measures higher rates. For detector B the same procedure was done, aligning the scattered beam in correspondence of PMT B0. Once the alignment is done, we turned off the spectrometers system, performing the other necessary calibrations with the detector A and B.

### 3.3.2 Beam Monitor Calibration, XY Monitor

The values measured by the beam monitors are digitalized by the VFCs. The analysis program converts the raw counts in voltage values with the formula shown in equation 2.16. For the calibration of the XY position monitors, special targets are used. In the target frame (see figure 3.5) there are two targets made by three carbon wires that are mounted at a known distance from each other, horizontally and vertically aligned.

The distance between the center of the two external wires is measured, to be  $d_{horizontal} = 2.38$  mm for the horizontal wires and  $d_{vertical} = 2.33$  mm for the vertical wires. The procedure to measure the scaling factor used to convert from the raw-data in V to  $\mu\text{m}$ , is the following: we ask MAMI operators to gradually shift the beam position, in the horizontal direction horizontal wire target and in the vertical direction for the vertical target. The beam position is changed by varying the magnetic field produced by the *Wobbler 16* magnets (see figure 3.6). During the position shift, the detectors measure the rate of scattered electrons, that increases when the beam hits one of the three wires and decreases when the beam is centered between two wires. We plot the detector counts versus the XY monitors values, in voltage, and we estimate the position of the two external peaks. This values can be used, together with the distance  $d_{horizontal}, d_{vertical}$  already measured, to compute the scaling factors. This procedure is repeated for  $X21/Y21$  and  $X25/Y25$  monitors. We plot the PMT rate versus the  $X25, X21, Y25, Y21$ , given in V. To identify the three peaks of the carbon target, we fit the data using a gaussian model (see figure 3.7). The mean  $\mu$  represents the center of the wire, given in V. We assume that the beam travels in a straight line beginning at the *Wobbler 16* magnet, that in our convection is the origin of coordinate system, with the  $z$  axis oriented toward to the target (left direction in the beam scheme).

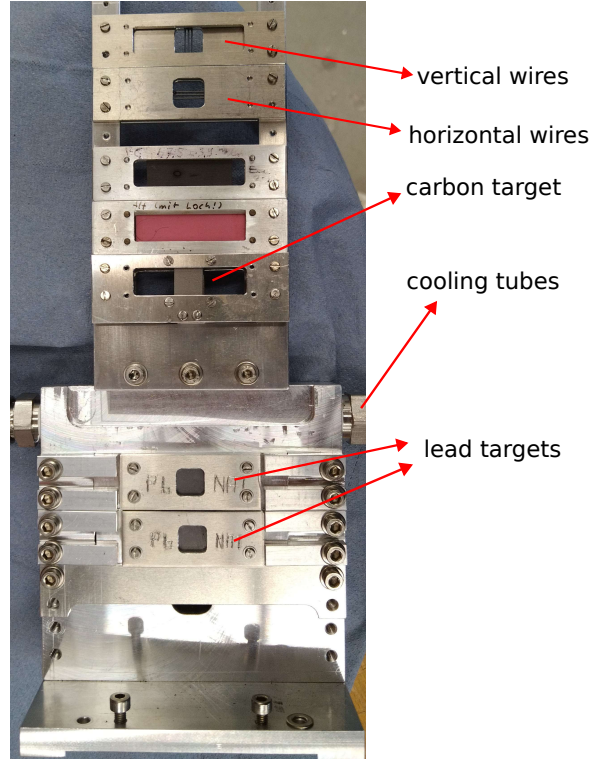


Figure 3.5: Target frame, on the top the three carbon wires that are used to calibrate the positions monitors. Then the carbon target and two lead targets.

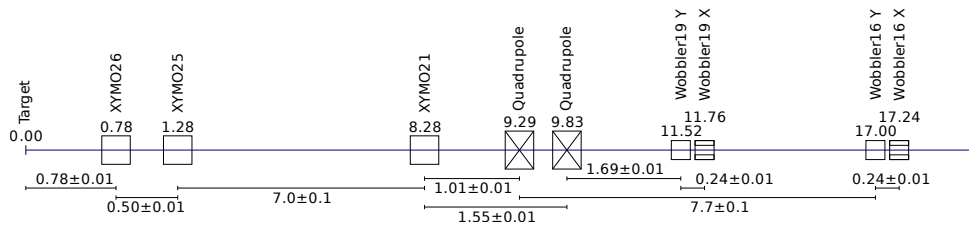


Figure 3.6: Beam line scheme.

The Beam parameters are measured by the Monitors  $X/Y_{21}, X/Y_{25}$ , which are located at some

distance with respect to the target. For the  $Y_{25}$  monitor (the procedure is the same for the others) the beam  $y$  position is described by:

$$Y_{beam} = m \cdot (Z_{Y25})$$

Where  $Z_{Y25}$  is the longitudinal distance between the *wobbler16* magnet and the  $Y_{25}$  monitor. From the scheme 3.6, the longitudinal distance between  $Y_{25}$  monitor and the *wobbler16* magnet is 1.57 m. The Position on the target is given by  $Y_{target} = m \cdot Z_{target}$ . The scaling factor is given by:

$$c_{Y25} = \frac{d_{vertical}[\text{mm}]}{Y_{target}} \quad (3.5)$$

where  $c_{Y25}$  indicates the scaling factor of the monitor. This procedure is repeated for all the monitors, and the scaling factor  $c_{Y25}$ ,  $c_{Y21}$ ,  $c_{X25}$ ,  $c_{X21}$  are measured. The analysis program uses these quantities to compute the beam position on the target, and from that the incident angles with respect to the  $X$ ,  $Y$  directions, which are needed for the analysis.

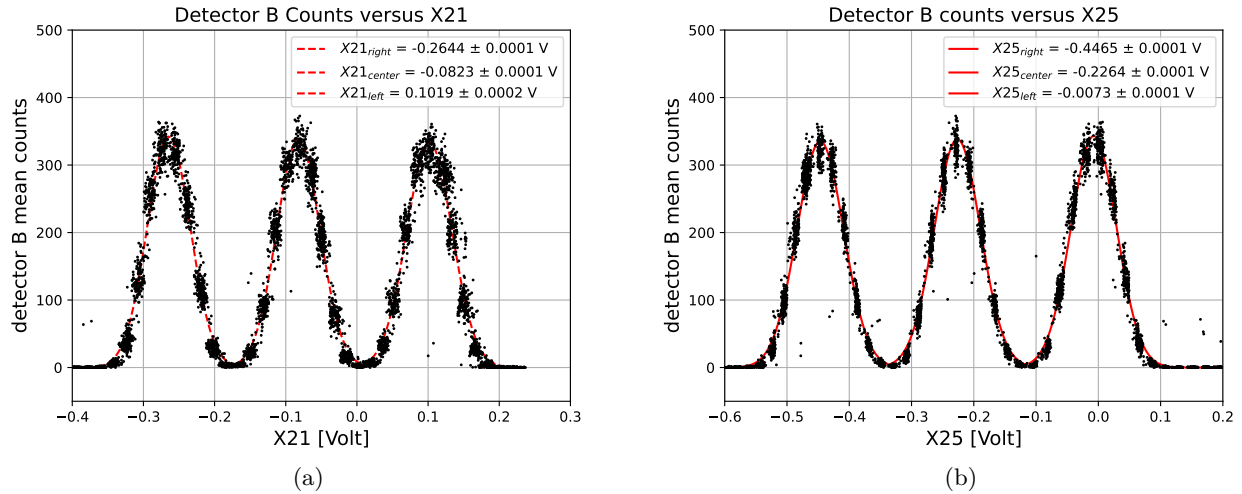


Figure 3.7: Plot of the averaged count of detector B, with the slow variations of the beam position in the horizontal direction. The three peaks occur when the beam is aligned with the center of the wire. The values on the X axis are in V

The analysis program calculate  $X$  and  $Y$  values in  $\mu\text{m}$ , combining the values measured by the two monitors (see figure 3.8).

The functions used are implemented considering a reference system with the origin coincident to the center of the target, and the  $Z$  axis oriented towards the *Wobbler16* magnet. The beam trajectory is described by the following equation:

$$\begin{aligned} y &= m_y \cdot z + q_y \\ x &= m_x \cdot z + q_x \end{aligned}$$

$q_x$  and  $q_y$ , that are the intercepts, are the desired quantities. Imposing in the above equations the passage through the points  $(Z_{25}; X_{25})$  and  $(Z_{21}; X_{21})$  (identical procedure for  $Y$ ) we can resolve the system for  $q_x$ , obtaining:

$$q_x = \frac{Z_{25} \cdot X_{21} - Z_{21} \cdot X_{25}}{Z_{25} - Z_{21}} \quad (3.6)$$

the solution for  $q_y$  is identical. The scattering angles  $\theta_x$  and  $\theta_y$  are instead related to the slope  $m$ , knowing that  $\tan(\theta) = m$ . The angles are given by the formula:

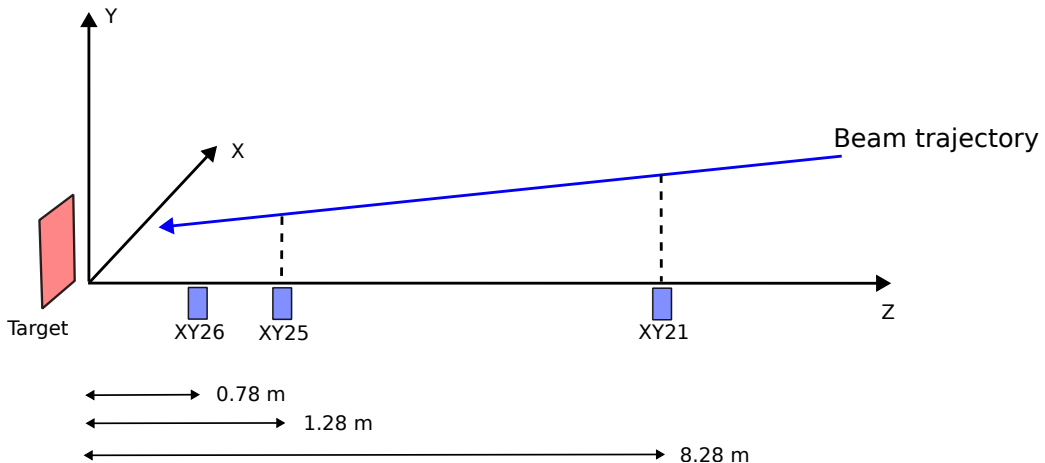


Figure 3.8: Figure of the beam trajectory, the position  $X$  and  $Y$  are measured by the monitors (blue boxes). Assuming a linear motion of the particles, the hitting positions on the target are computed.

$$\theta_x = \frac{X_{25} - X_{21}}{Z_{25} - Z_{21}} \quad (3.7)$$

To check that the functions are well implemented, we plot in figure 3.9 the PMTs counts versus the  $X$  beam position on the target. the distance between the two external peaks, reported in the plot, is in agreement with the expected distance  $d_x = 2.38$  mm.

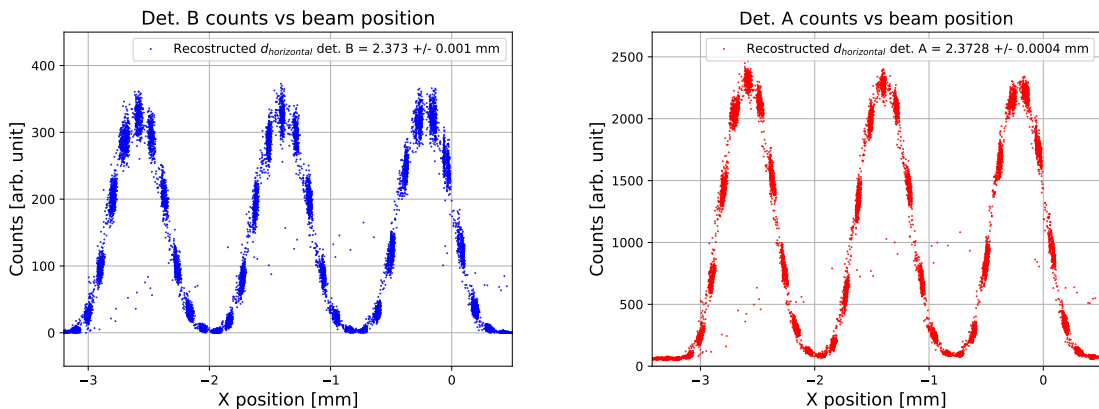


Figure 3.9: Plot of the PMT Count versus the  $X$  and  $Y$  positions given in mm.

For brevity, we report only the plot for the  $X$  position. The result for  $Y$  are analogous.

### 3.3.3 Current (PIMO) Calibration

Other two calibration parameters required are about the energy and the current of the beam, and are measured with PIMO (current monitor) and ENMO (energy monitor). In the analysis, the current is given in  $\mu\text{A}$  and the beam energy in keV.

The relation between the values measured in V units and the real values in  $\mu\text{A}$  and eV is linear:

$$I(\mu\text{A}) = mI(V) + q$$

For the current monitor, the two coefficients are determined raising the beam current from 10  $\mu\text{A}$  to 22  $\mu\text{A}$  in several step. For each step we compare the nominal values of the current with the values measured in V, the values are shown in figure 3.10

with a linear fit,  $m$  and  $q$  are determined. These parameters are added in the standard configuration file, where the analysis program loads all the coefficients needed to process the data.

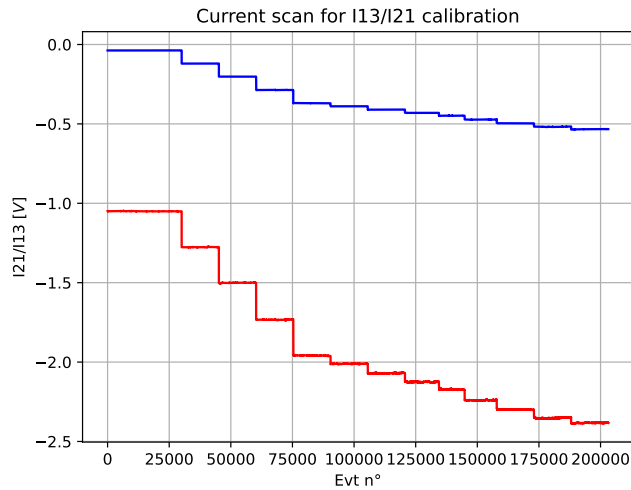


Figure 3.10: Current scan for the calibration, each step correspond to a run with a different beam current. The  $x$  axis represents the number of the event analyzed, and each event is 80 ms long.

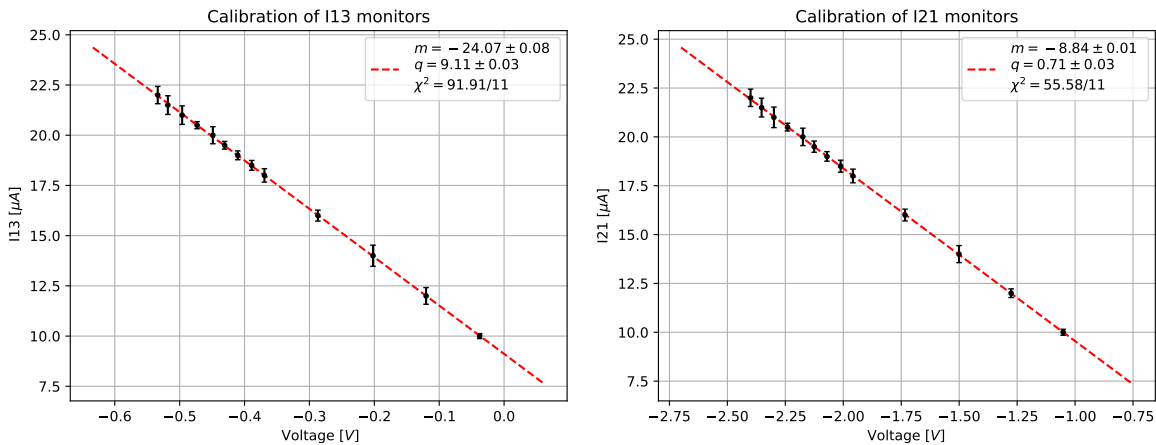


Figure 3.11: Calibrations plots for PIMO I21 and PIMO I13, the errors are multiplied by 25.

The coefficients measured with the fit are shown in the figure 3.11. The errors shown in both the plots are given by the sampling standard deviation formula, applied to each step in plot 3.10. The error  $\sigma_{vfc}$  is related to uncertainty of VFCs and beam monitors, and is propagated to the  $y$  axis. Yet, we are underestimating the error associated with the nominal beam current  $I$ , whose accuracy is not known. We suspect that is not negligible compared to  $\sigma_{vfc}$ .

### 3.3.4 Energy Monitor (ENMO) calibration.

The ENMO calibration is performed in a different way from the other monitors. exploiting the polarity signal which controls the beam polarization at the source of the acceleration. The MAMI operators use the signal to create artificially a difference in the beam energy that is correlated to the beam polarization, with the last two sub-events having a higher energy with respect to the first two. The energy difference is nominally 22.6 keV. Since the nominal difference is known, the scaling factor which convert from V to keV is easy to compute. The energy difference between the sub-events  $\delta E$  (with  $E_{18}$  being the energy monitor) is defined as:

$$\delta E = \frac{E_{18}[2] + E_{18}[3]}{2} - \frac{E_{18}[0] + E_{18}[1]}{2}$$

The measured values of  $\delta E$  are shown in an histogram in figure 3.12. Three runs, collected with different currents of the beam, were collected. As the output voltage signal from the XY monitor, also the energy monitor is proportional to the current, as mentioned in equation 2.15. The relation between energy  $E$  keV and the signal amplitude of the energy monitor  $UV$  is given by:

$$E [\text{keV}] = c_E \cdot \frac{U [\text{V}]}{i} \quad (3.8)$$

So, if we invert the relation, we have that:

$$c_E = \frac{E}{U} \cdot i \quad (3.9)$$

This is the formula to compute the conversion factor for the energy monitor. The beam current was set to 0, 15  $\mu\text{A}$  and 20  $\mu\text{A}$ . The run with zero current is useful to check presence of an offset.

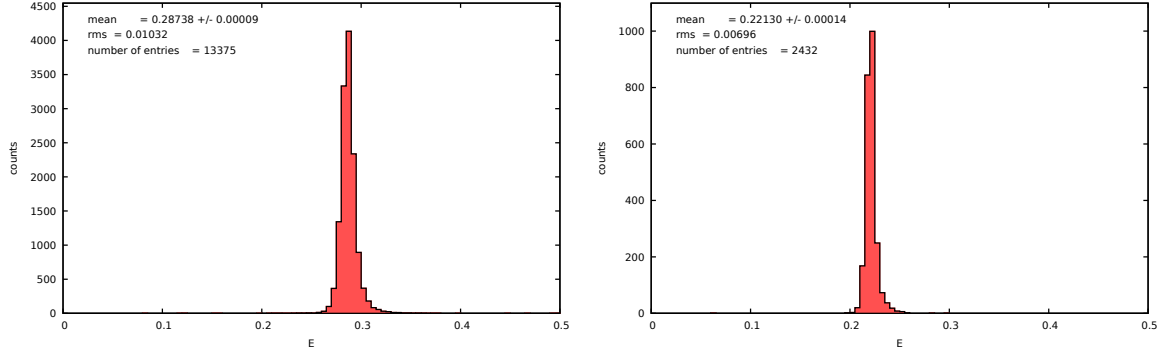


Figure 3.12: Histograms or  $\delta E$  with the beam current 20  $\mu\text{A}$  on the left and 15  $\mu\text{A}$  on the right.

To study the dependence on the current, a linear fit is done (see figure 3.13). The  $c_E$  conversion parameter is obtained taking the coefficient parameter  $m$  from the fit and substituting in the expression:

$$C_E = \frac{22.6 \text{ keV}}{m}$$

From this we obtain the value  $c_E = +1595.2$  necessary to convert from Voltage units to keV.

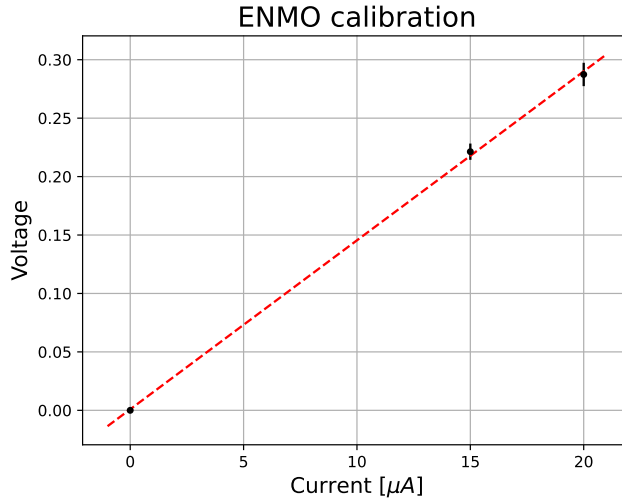


Figure 3.13: Calibration of ENMO monitor, plot of the ENMO voltage values versus the current.

To check the procedure, in figure 3.14 we plot  $\delta E$  given in physical units. For 15  $\mu\text{A}$   $\delta E = 23.519 \pm 0.014 \text{ keV}$  and for 20  $\mu\text{A}$   $\delta E = 22.600 \pm 0.007 \text{ keV}$ .

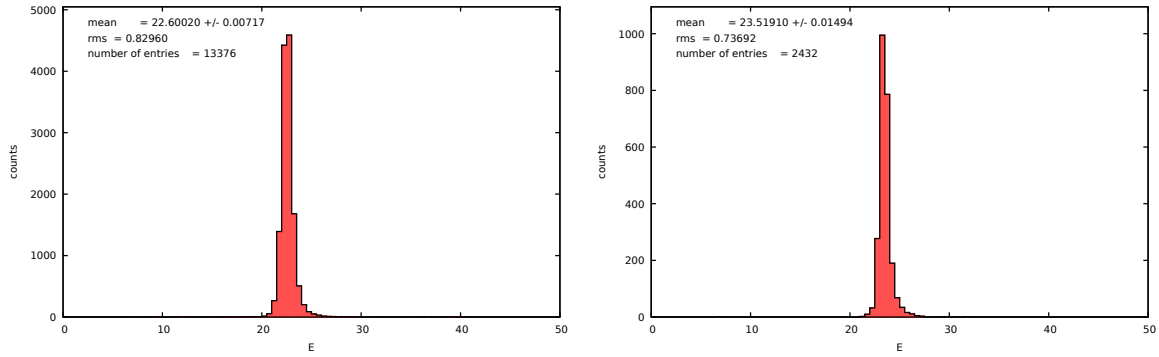


Figure 3.14: Plot for the physical quantities computed in the data tree, for two different current of the beam (on the left 20  $\mu\text{A}$ , 15  $\mu\text{A}$  on the right)

### 3.3.5 Calibration of the PMTs

Several scans in attenuation of the NINO board were performed on the beam, to choose the best working point for the PMTs of the detectors. The same procedure used in the laboratory was followed: with a beam intensity of 10  $\mu\text{A}$  we acquired data runs one minute long, varying the attenuation.

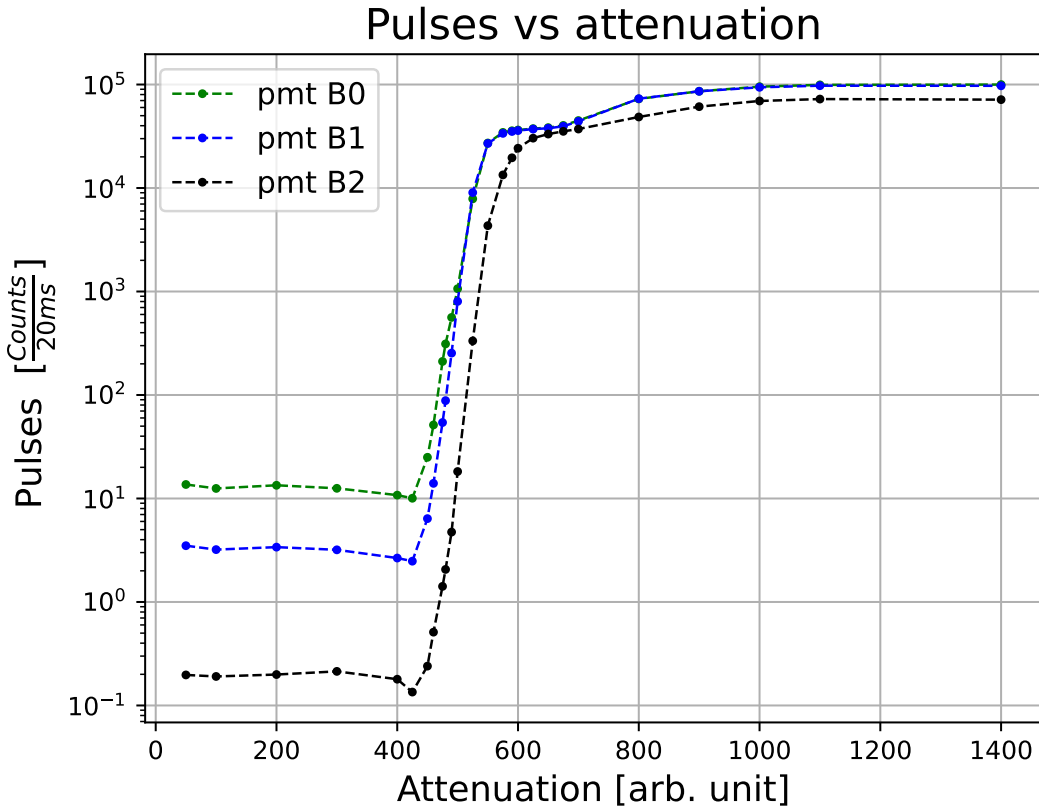


Figure 3.15: Scan in attenuation of the NINO board, with 10  $\mu\text{A}$ . Each point represents the averaged of the counts made on all sub-events of a single data run. Each data run is 1 min long, which correspond to 3000 sub-events.

The PMTs counts in 3.16 and 3.15 are visualized in a different way. It is preferable to visualize the increment of number of signals that pass the threshold selection of NINO board. For this reason, we want to differentiate the data showed in the plots. This procedure consist in computing the difference between the counts at a certain point and the previous one, and dividing by the increment in attenuation, in equation 3.10.

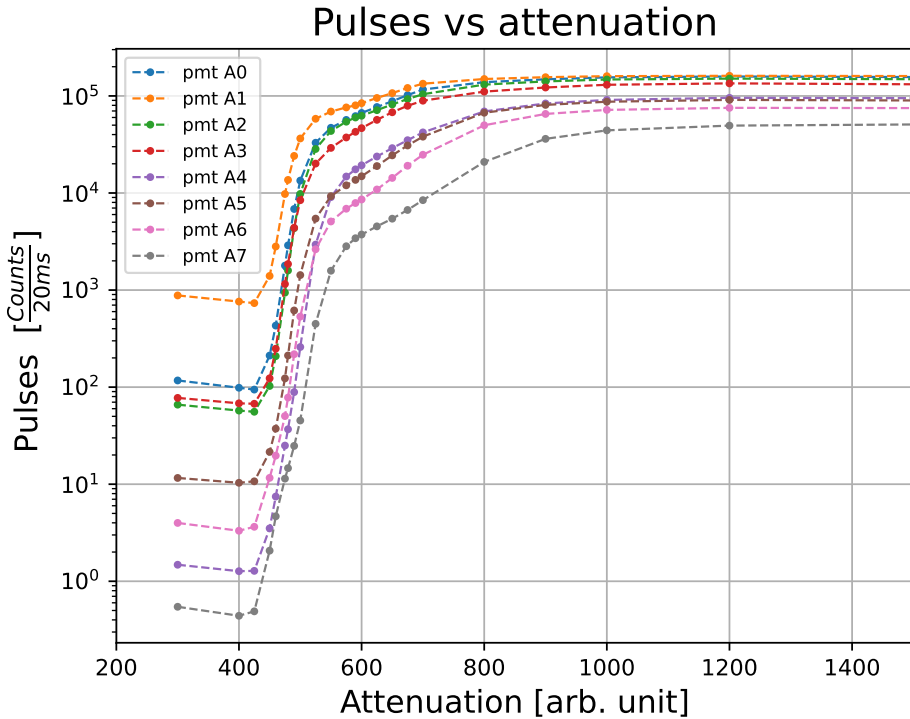


Figure 3.16: Scan in attenuation of the NINO board, with  $10 \mu\text{A}$ . Each point represents the averaged of the counts made on all sub-events of a single data run. Each data run is 1 min long, which correspond to 3000 sub-events.

$$\text{Spectra} = \frac{N(\text{att}_i) - N(\text{att}_{i-1})}{\text{att}_i - \text{att}_{i-1}} \quad (3.10)$$

With this formula we compute  $\frac{\partial N}{\partial \text{att}}$ , the discrete derivative of the data shown in figure 3.16.

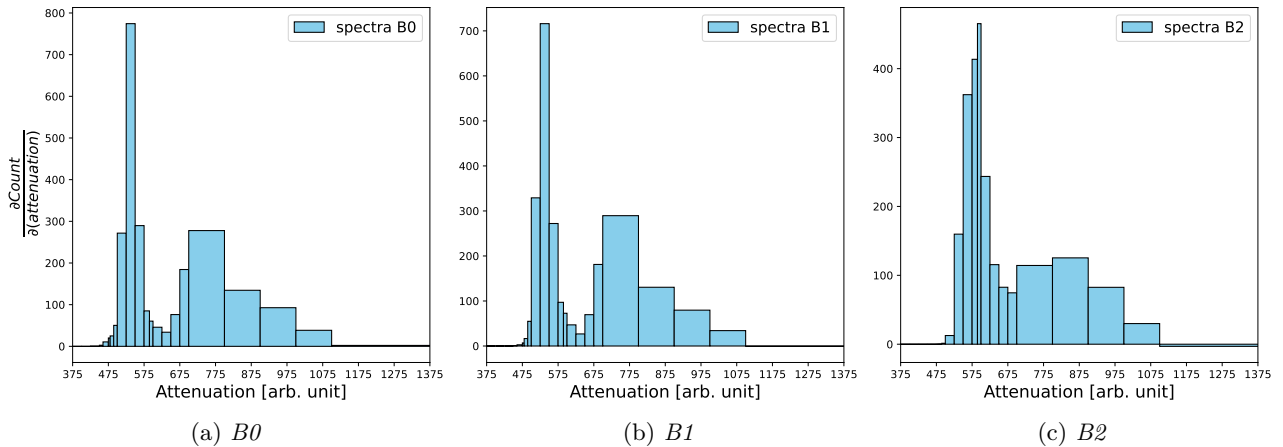


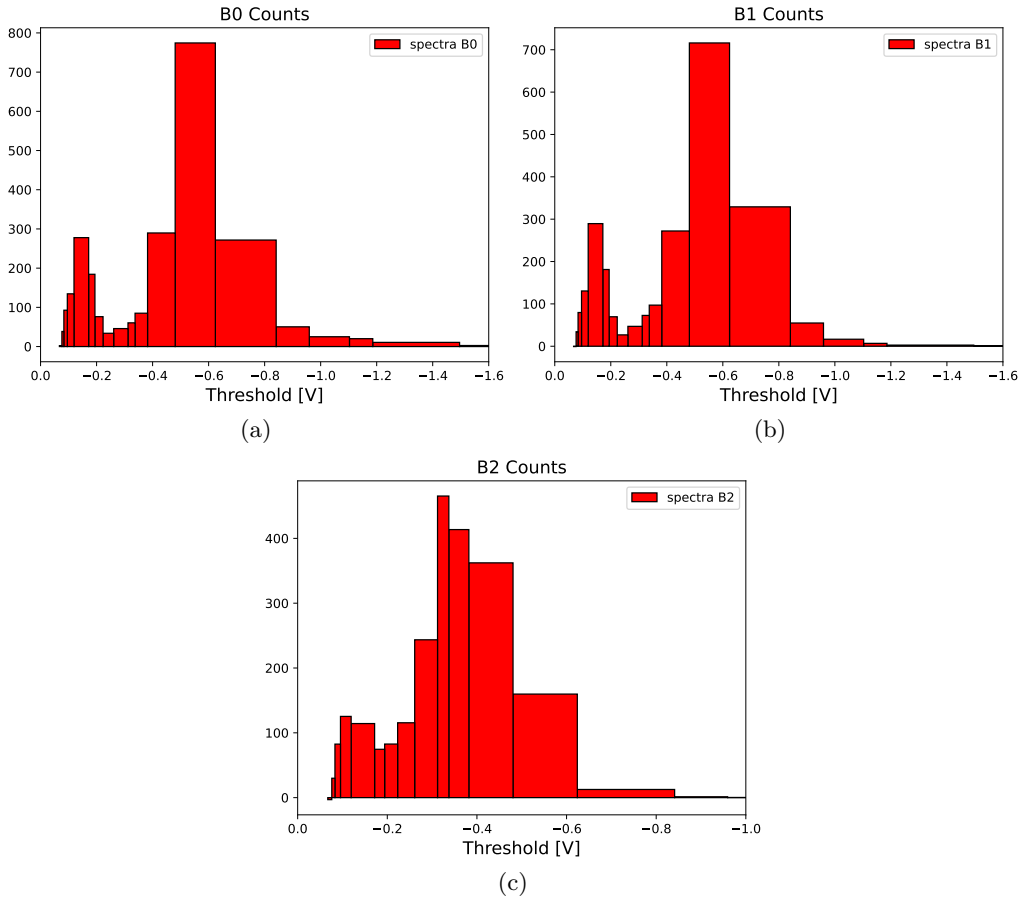
Figure 3.17: Reconstructed spectra for Detector B

These plots are used to identify a good point to select the attenuation values. If we look at the plots 3.1, we can see that the physical threshold does not scale linearly with changing the  $Att$  value, and for high values of  $Att$ , the threshold falls quickly at zero. Looking at the signal spectra, we identify the first peak as the electron signal. The other peak (on the right), correspond to very low threshold values, and it is identified as background noise. We selected the values of the attenuation between the peaks of the two distributions, maximizing the signal acceptance and trying to reject the background as much as possible. Our discussion so far is sufficient to carry out the calibration of the PMTs and

take data to measure the asymmetry. However, we would like to identify the physical threshold in mV instead of attenuation unit. We can use the conversion function that we discussed in figure 3.1:

$$f(att) = \frac{a}{(x - b)^3 + d}$$

We point out that the parameters of this function have been obtained from data that have not been acquired during this thesis work, moreover the threshold value in the program that controls the NINO board is slightly different (we always used 600, the data are taken with 750), therefore the values in volts need probably to be rescaled by some factor, but for our discussion we are interested in a raw estimation of the signal peak: With this conversion, we show the same plots in 3.17, with the values in the x-axis in V now.



We now see clearly two peaks, the signal and the background, that are reversed respect to figure 3.17. We discuss now a simple model that we used to describe how the PMT Counts vary when we raise the attenuation. From the plot 3.17, we assume that the two peaks are described by two gaussian distributions. Now if we think about the probability for a signal to pass the selection, this quantity is equal to the probability of being in below the attenuation value. Using now the fact that the probability are given by the cumulative of the gaussian distribution (probability of being in the right tail) it is straightforward to deduce:

$$P(\text{signal} > thr) = \Phi(x) = \frac{1 + \text{Erf}\left(\frac{x - \mu}{\sqrt{2}\sigma}\right)}{2}$$

Considering that we have the sum of two gaussian distribution, we end with:

$$N(att) = \frac{n_1 + n_2}{2} + \left(\frac{n_1}{2}\right)\text{Erf}\left(\frac{x - \mu_1}{\sqrt{2}\sigma_1}\right) + \left(\frac{n_2}{2}\right)\text{Erf}\left(\frac{x - \mu_2}{\sqrt{2}\sigma_2}\right) \quad (3.11)$$

This model is used to fit the data shown in figure 3.16. The result is shown in figure 3.18, the parameters obtained from the fit are reported below:

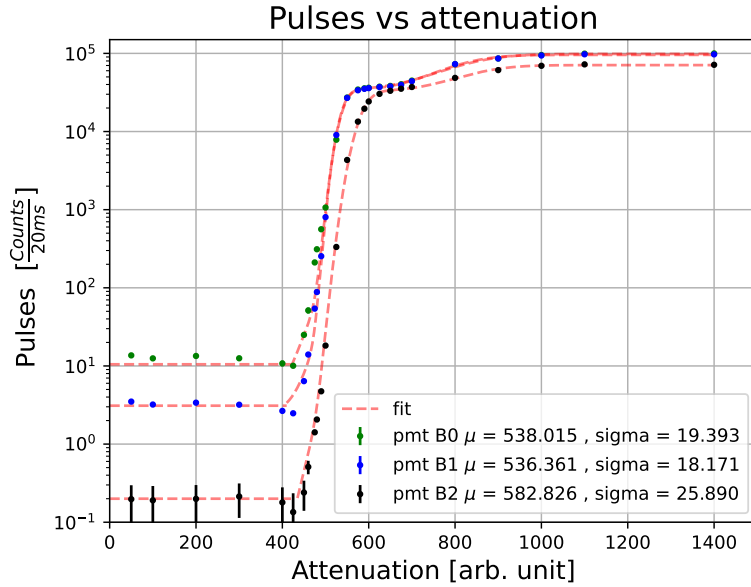


Figure 3.18: Best fit for the data of counts versus attenuation, for detector B.

PMT	$\mu_1$	$\sigma_1$	$\mu_2$	$\sigma_2$	n1	n2
B0	538.0 +/- 1.3	19.4 +/- 1.1	798 +/- 8	103 +/- 4	34277 +/- 662	64244 +/- 1538
B1	536.4 +/- 0.9	18.2 +/- 0.7	783 +/- 5	89 +/- 2	34053 +/- 475	61636 +/- 1109
B2	582.8 +/- 1.2	25.9 +/- 1.0	824 +/- 8	88 +/- 6	32880 +/- 758	37930 +/- 1245

Table 3.11: Best fit result for the model defined in equation 3.11

From these result we measure the mean  $\mu_1$  and  $\mu_2$  for the signal and the background given in attenuation units. The correct value of attenuation is set between the two observed peaks, in order to reject the background and take only the signal coming from the scattered electrons. The same procedure was followed also for the detector A, the plots are not reported, for brevity. With this procedure, the *Att* value has been selected. The values are reported in table 3.12

PMT n°	B0	B1	B2	A0	A1	A2	A3	A4	A5	A6	A7
Att	600	600	625	600	590	600	600	600	590	600	600

Table 3.12: Attenuation settings for both the detectors.

### 3.3.6 Auto-calibration Procedure

In this section we present the last calibration technique needed. The auto-calibration is a special operation mode of the MAMI accelerator, during which the beam current is made to vary in a controlled way. Through these special runs is possible to measure again the current scaling factor, already discussed in section 3.3.3. Furthermore, it is possible to study the linearity of the PMTs: during the auto-calibration, the beam current is raised from 9  $\mu\text{A}$  to 11.125  $\mu\text{A}$  in step of 0.125  $\mu\text{A}$ , as shown in figure 3.19

From a linear fit of the PMTs counts vs. current intensity the angular coefficient and the offset are measured. The offset is particular important because give rise of a possible systematic error that influence the final asymmetry result. It is simple to demonstrate this, if a relation of the type  $N = mI + N_0$  holds. Consider the following quantity:

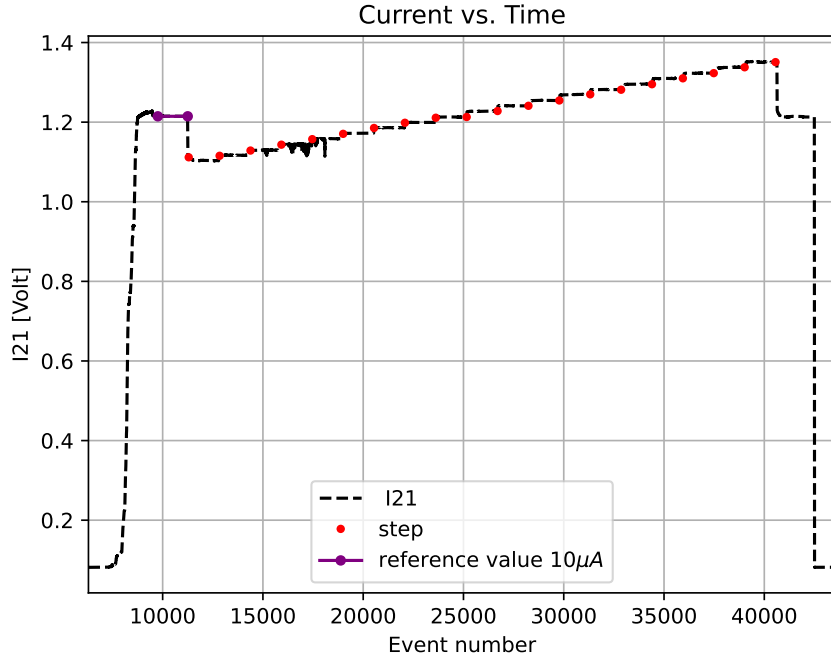


Figure 3.19: Auto-calibration: in this plot we have the voltage value of I21 monitor. The current is first stabilized around 10  $\mu\text{A}$ , then it is raised from 9  $\mu\text{A}$  (the step lower down) to 11.125  $\mu\text{A}$  in step of 0.125  $\mu\text{A}$ .

$$\bar{N} = \frac{N_{\uparrow} + N_{\downarrow}}{2}$$

we can express  $N_{\uparrow}$  and  $N_{\downarrow}$  in this way using the asymmetry  $A_n = \frac{N_{\uparrow} - N_{\downarrow}}{N_{\uparrow} + N_{\downarrow}}$ :

$$\begin{aligned} N_{\uparrow} &= \bar{N} + A_n \bar{N} \\ N_{\downarrow} &= \bar{N} - A_n \bar{N} \end{aligned}$$

Now we suppose that  $\bar{N}$  is linear dependent on the current in the way we defined above, so:

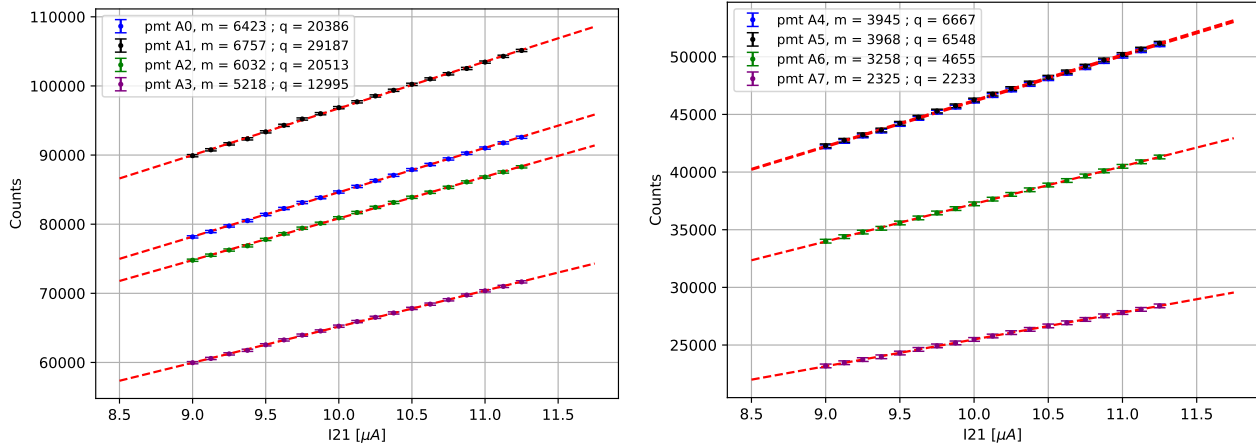
$$\begin{aligned} N_{\uparrow} &= mI + N_0 + A_n(mI) \\ N_{\downarrow} &= mI + N_0 - A_n(mI) \end{aligned}$$

We are supposing that the offset  $N_0$ , we assume that the present offset does not contribute to the asymmetry, i.e. it is not correlated to the signal of the scattered electrons, but is due to processes of another type, therefore in the previous formulas only the  $mI$  counts must be multiplied by the asymmetry  $A_n$ . Therefore if we substitute everything in the definition of the transverse asymmetry:

$$A' = \frac{N_{\uparrow} - N_{\downarrow}}{N_{\uparrow} + N_{\downarrow}} = \frac{A_n(2mI)}{(2mI) + 2N_0} = A_n \frac{1}{1 + \frac{N_0}{mI}} = A_n \cdot c \quad (3.12)$$

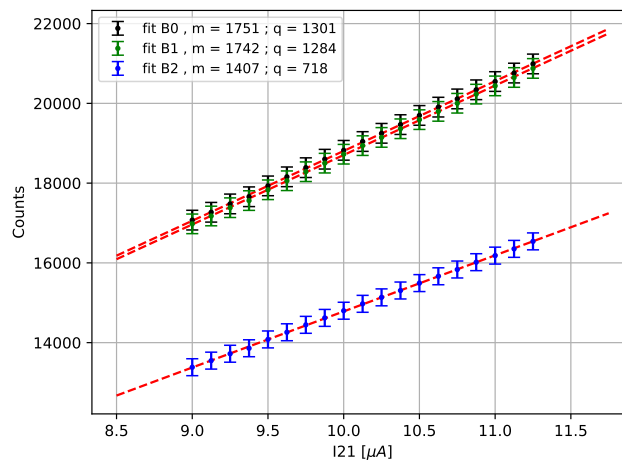
In the last passage we learn that the presence of an offset can decrease the reconstructed asymmetry. So it is important to determine quantitatively  $N_0$  and  $m$  in order to be able to correct for this effect. The strategy used is quite simple: every three hours of production data, we asked MAMI to start the auto-calibration program. With all the auto-calibration runs, we estimate  $N_0$  for each PMT, separately. Then all this quantities are saved in a file so that the analysis program can retrieve the parameters and subtract them from the PMT counts. In this way every three hours the PMT are

corrected, taking care also of the possibility that the the linearity of the PMTs can change after hours of use of the PMTs (for example it can decrease the efficiency). With a linear fit we can estimate the angular scale coefficient and the offset to convert from I21 voltage values to physical values of the current. The procedure is repeated for the 8 auto-calibration acquisition we had during the beam time, so we can also take care of possible time variations.



(a) Current scan for detector A, the error are multiplied by a factor of 20.  
(b) Current scan for detector A, the error are multiplied by a factor of 20.

Figure 3.20: PMT Rates vs current (from I21 monitor), linear model is used to fit the data.



(a) Current scan for detector B, the error are multiplied by a factor of 20.

Figure 3.21: PMT Rates vs current (from I21 monitor), linear model is used to fit the data.

The figures shown in 3.20 and 3.21 are referred to the data acquired for the first auto-calibration run; the values of slope and offset measured during the first auto-calibration are in table 3.13. These data are valuable because we can compute  $c$ , the factor that appears in equation 3.12:

Ignoring the presence of the offset leads to two consequences: the reconstructed asymmetry is lower, on average  $\simeq 10\%$  less than expected, and the counts are overestimated. Because the error depend on the PMT counts, as seen in equation 2.2, this two effect combined add up and decrease the accuracy of the asymmetry measurement. The value  $c$  reported in the chapter 5 can be compared with  $c$  in table 5, computed as the ratio between  $\frac{A_{notcorr}}{A_{corr}}$ , where  $A_{notcorr}$  stands for the asymmetry result not corrected for the offset and  $A_{corr}$  are the result with offset corrected.

PMT	$m [\mu\text{A}^{-1}]$	Offset	c
B0	1750	1301	$0.930 \pm 0.003$
B1	1742	1283	$0.931 \pm 0.003$
B2	1406	717	$0.951 \pm 0.003$
A0	6423	20385	$0.759 \pm 0.002$
A1	6756	29187	$0.698 \pm 0.003$
A2	6032	20513	$0.746 \pm 0.002$
A3	5218	12995	$0.800 \pm 0.002$
A4	3945	6666	$0.855 \pm 0.002$
A5	3967	6547	$0.858 \pm 0.002$
A6	3258	4655	$0.874 \pm 0.002$
A7	2325	2233	$0.912 \pm 0.002$

Table 3.13: Angular coefficient and offset obtained for the auto-calibration. The third column is contains the estimation of  $c$ , as defined in equation 3.12

### 3.4 Data Tree Implementation

We now discuss briefly the structure of the data that is implemented in the analysis program, important to clarify how data analysis will be developed. The base class that is implemented in the analysis program is the *Event* class. As we mention above in section 2.1, we do not intend to keep track of the single scattered electron, instead we analyze time series of 80 ms, in which we simply count all the electrons detected in this time interval. The work-flow of the analysis program is load the binary file collected during the beam time, parsing one event at a time and processing the raw-data from the beam monitors and the detectors (see figure 3.22).

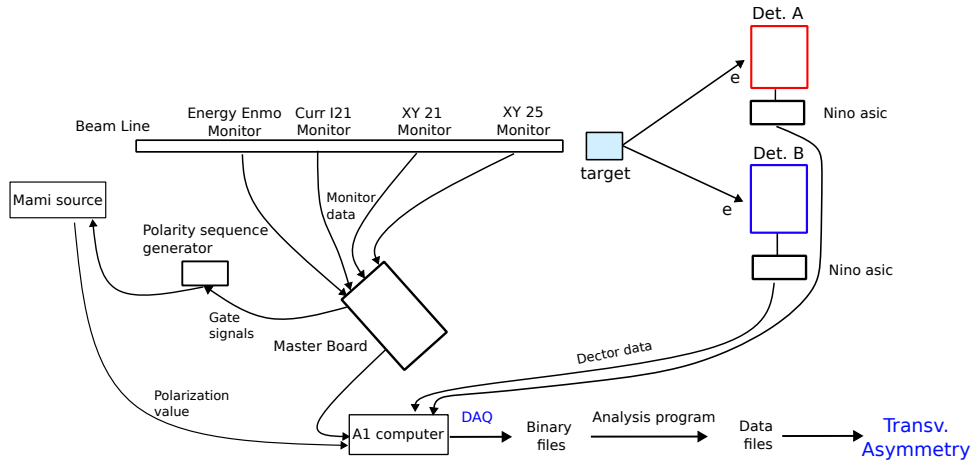


Figure 3.22: Scheme of the data flow.

During the execution of the program data files in *.txt* are generated and filled with the processed data ready. The output data-file can be analyzed with any software package, such as root or python, to get the value of the asymmetry  $A_n$ . Referring to the figure 2.1, we remind that every event is divided into 4 sub-events. For each different sub-event a precise state of the polarization is defined, +1 for  $S = \uparrow$  and -1 for  $S = \downarrow$ . Every sub-event is 20 ms long; during this time interval master-board receives all the data coming from the monitors and the detectors and sent them to the data-acquisition program (DAQ) that produces the binary-files, which are the input of the main analysis program. It is important to note that for each sub-event, a single measurement is acquired from the beam monitors, which is intended as a time average of the various signals on the 20 milliseconds of sub-event duration. The sampling rate is then equal to 50 Hz. This structure of the data is quite specific. The main reason for this setup is connected with the need to avoid as much as possible that the variations of intensity, position and energy of the beams induce an effect that add to  $A_n$ . Considering only small time series, it is assumed that the beam is quite stable, in order to reduce undesired effects. Nevertheless, the

contribution of these effects, which are indicated for brevity as false asymmetries, is considered in the final model. Several values are saved with the number of scattered electrons, for each event. The general structure of the data tree, with the important quantities, is reported here figure 3.23

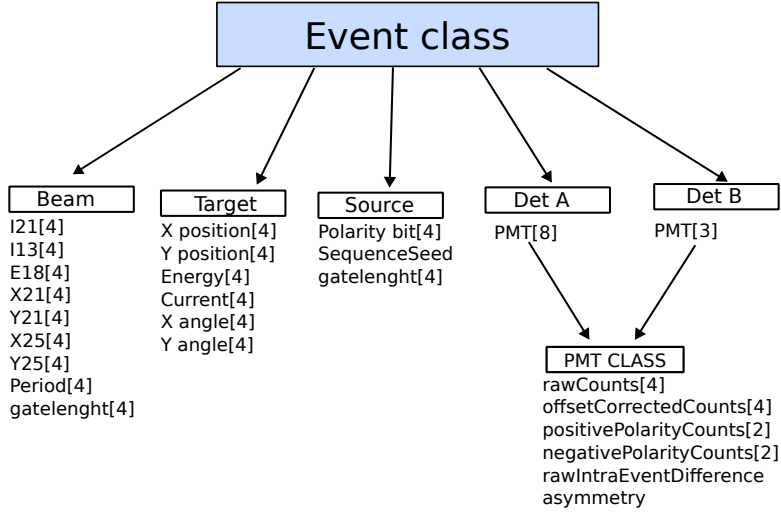


Figure 3.23: Scheme of the Event class, the structure of the data tree is explained in the appendix.

The analysis program reads the binaries files, converts from binary to decimal values and computes the beam parameters from the raw data of the monitors, filling the data tree shown in the figure. We have 5 different classes, that are contained in the main *Event* class. The asymmetry values are stored in the two separated classes, *Det A* and *Det B*. The analysis program read and analyze one event at a time, can produce also histograms for a fast visualization of the data, and generates the final output files in *txt* format for the data analysis.

## Chapter 4

# Asymmetry on Carbon and Rates on Lead Target.

Once the calibrations are completed, the data are analyzed, to determine the transverse asymmetry on  $^{12}C$ . In this chapter we outline the steps involved in pre-selecting the data and in analyzing the asymmetry of the two detectors. The amount of data collected during the experiment is 23 hours of beam time, which corresponds roughly to 1 million of events.

A section is dedicated to the measurement with lead target; through these measurement, we calculate the amount of statistics needed to measure the transverse asymmetry on  $Pb$  with an accuracy of  $\simeq 1 ppm$ . Finally, we discuss the problem of the false asymmetries, that could influence the final result, trying to calculate their contribution directly.

### 4.1 Model for Fitting the Data

One of the problems of the measurement is to take into consideration the various contributions that can change the value of the asymmetry measured by the experimental apparatus. The PMTs counts, and consequently the measured asymmetries, can be affected by the variation of the beam parameters during the time. These effects are summarized in the list below:

- variation of the  $(x, y)$  impact position of the beam on the target
- the variations of the incident angles  $\theta_x$  and  $\theta_y$  on the target.
- the uncertainty associated with the energy of the beam, a change in the energy associated with the polarization of the beam leads to different rates for the cross section.
- the uncertainty associated with the current of the beam, in particular a difference in the efficiency of the source in producing electrons polarized in the two opposite directions.

All these quantities, which we will indicate in general with  $\delta q$ , could be correlated to false asymmetries, which influence the measured values of  $A_n$ . Furthermore,  $A_n$  is expected to be small, in the order of ten part per million, and beam variations can not be neglected. Correcting directly the false asymmetries that arise from these uncertainties is a difficult task, and it is easier to adopt a different strategy rather than the analytical/numerical calculation of each of them. Knowing that the beam parameters produced by MAMI are quite stable over the time, we can assume that the measured asymmetry are well described by a linear model as the following:

$$A_{tot} = A_{physical} \cdot P + \delta_I + A_x \delta x + A_y \delta y + A_{\theta_x} \delta \theta_x + A_{\theta_y} \delta \theta_y + A_E \delta E \quad (4.1)$$

$A_{physical}$  is the aim of the experiment,  $A_x$  and  $A_y$  are the coefficients induced by the variation of the position of the beam,  $A_{\theta_x}$  and  $A_{\theta_y}$  are the coefficients associated to angles,  $A_E$  is the coefficients associated to the beam energy and  $P$  is the polarization percentage. This is a first order approximation, which is valid for small variation of the beam parameters  $(\delta x, \delta y, \delta \theta_x, \delta \theta_y, \delta E)$ . We must clarify now

what we mean with  $\delta x, \delta y, \delta\theta_x, \delta\theta_y, \delta E$ . Recalling the event structure, that we discussed in section 2.1, we have a sequence of 4 different sub-events, with a polarization pattern that is randomly selected between  $\uparrow, \downarrow, \downarrow, \uparrow$  and  $\downarrow, \uparrow, \uparrow, \downarrow$ . During the 20 ms of time length of each sub-event, the beam monitors provide a single measurement of the beam parameters, and the data are saved in the data tree. The task of the analysis program is to use this raw data to calculate the relevant parameters for the analysis. Because we are working with asymmetries, the absolute values of the parameters listed above is not relevant, instead what is relevant are the differences between different polarization states of the beam. Assuming this,  $\delta x, \delta y, \delta\theta_x, \delta\theta_y, \delta E$  are defined by equation 4.2:

$$\begin{aligned}\delta x &= \left( \frac{x_{\uparrow}(1) + x_{\uparrow}(2)}{2} \right) - \left( \frac{x_{\downarrow}(1) + x_{\downarrow}(2)}{2} \right) \\ \delta y &= \left( \frac{y_{\uparrow}(1) + y_{\uparrow}(2)}{2} \right) - \left( \frac{y_{\downarrow}(1) + y_{\downarrow}(2)}{2} \right) \\ \delta E &= \left( \frac{E_{\uparrow}(1) + E_{\uparrow}(2)}{2} \right) - \left( \frac{E_{\downarrow}(1) + E_{\downarrow}(2)}{2} \right) \\ \delta\theta_x &= \left( \frac{\theta_{x,\uparrow}(1) + \theta_{x,\uparrow}(2)}{2} \right) - \left( \frac{\theta_{x,\downarrow}(1) + \theta_{x,\downarrow}(2)}{2} \right) \\ \delta\theta_y &= \left( \frac{\theta_{y,\uparrow}(1) + \theta_{y,\uparrow}(2)}{2} \right) - \left( \frac{\theta_{y,\downarrow}(1) + \theta_{y,\downarrow}(2)}{2} \right) \\ \delta I &= \frac{I_{\uparrow} - I_{\downarrow}}{I_{\uparrow} + I_{\downarrow}}\end{aligned}\tag{4.2}$$

Each  $\delta q$  represents the variation of one of the parameters of the beam within an event, so. One may wonder why the model doesn't contain a parameter  $A_I$  to describe the false asymmetry due to the current. We can show theoretically that the values of  $A_I$  is equal to 1. Starting from the definition of rate  $\Gamma$ :

$$\Gamma = \frac{dN}{dt} = \frac{I_0}{e} \sigma \frac{n_t V_t}{S}\tag{4.3}$$

where  $I_0$  is the beam current,  $e$  is the elementary charge,  $n_t$  is the number density of the target,  $V_t$  the target volume and  $S$  is the surface of the beam. Using 4.3, the total asymmetry  $A$  is given by the equation 4.4.

$$A = \frac{\frac{dN_{\uparrow}}{dt} - \frac{dN_{\downarrow}}{dt}}{\frac{dN_{\uparrow}}{dt} + \frac{dN_{\downarrow}}{dt}} = \frac{\sigma_{\uparrow} I_{0\uparrow} - \sigma_{\downarrow} I_{0\downarrow}}{\sigma_{\uparrow} I_{0\uparrow} + \sigma_{\downarrow} I_{0\downarrow}}\tag{4.4}$$

Let's suppose now that the false asymmetry associated to the current is given by  $A = A_I \cdot \delta I$ . Now, the formula in the model is slightly different

$$A = \frac{\sigma_{\uparrow} - \sigma_{\downarrow}}{\sigma_{\uparrow} + \sigma_{\downarrow}} + \frac{I_{\uparrow} - I_{\downarrow}}{I_{\uparrow} + I_{\downarrow}} = \frac{2(\sigma_{\uparrow} I_{0\uparrow} - \sigma_{\downarrow} I_{0\downarrow})}{2\sigma_{\uparrow} I_{0\uparrow} + 2\sigma_{\downarrow} I_{0\downarrow} + \sigma_{\uparrow} I_{0\downarrow} + \sigma_{\downarrow} I_{0\uparrow}}\tag{4.5}$$

Now, the asymmetry in the cross section is expected to be of the order of  $10^{-6}$ . If we approximate  $\sigma_{\uparrow} \simeq \sigma_{\downarrow}$ , the two formula above are equal. In the end we have the equation 4.6.

$$A_{tot} = A_n + \frac{I_{0\uparrow} - I_{0\downarrow}}{I_{0\uparrow} + I_{0\downarrow}} = A_n + \delta I\tag{4.6}$$

This is a direct consequence of the fact that the luminosity is proportional to the beam current, so we don't need to add a new parameter to the model.

## 4.2 Data Pre-selection and Fit

After all the calibration are performed, the analysis program is ready to produce the data-files suitable to analyze the asymmetry data for Carbon. Before proceeding with the linear fit, however, it is

necessary to visualize the data to check that there are no anomalous behaviors. In fact the data can contain moments of loss of the beam current and sudden interruptions, loss of the beam polarization and even setting errors by MAMI operators can affect the experiment. Carbon data were taken from November 2nd to 4th, and consist of 28 runs, each 1 hour long. The first step is to observe the PMT counts and the current trend, in order to be able to identify sudden interruptions of the beam, outliers and to check the behaviour. In figure 4.1 we show the trend over time for the of series runs.

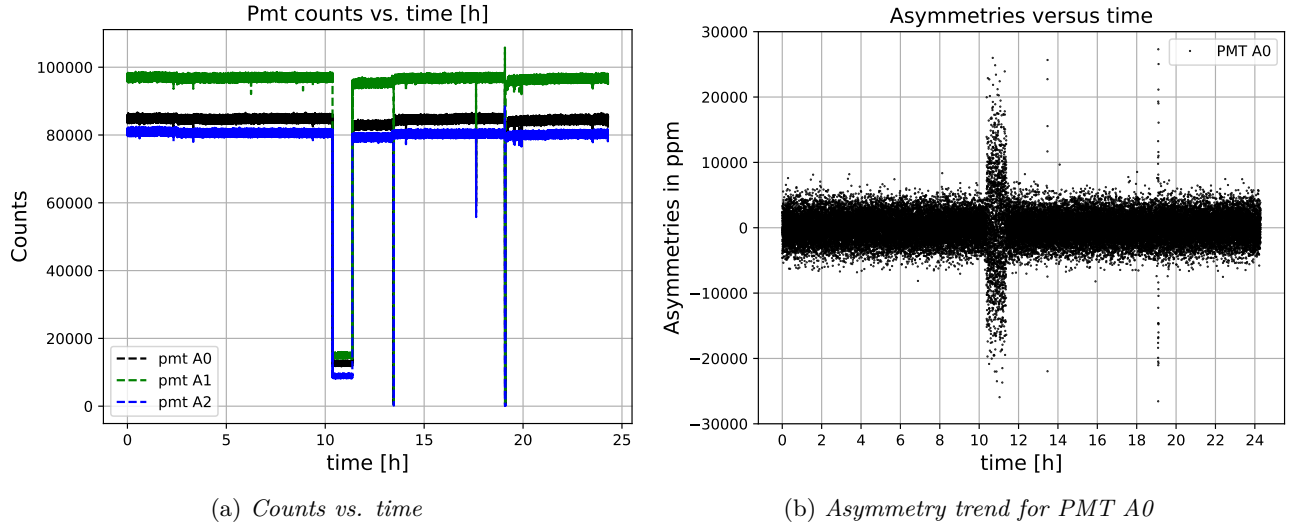


Figure 4.1: On the left, counts versus time for all the runs acquired during the beam time. On the right the measured asymmetry versus time. The conversion from event number to time is made knowing that each event correspond to 80 ms. A total of 22 hours of beam was collected.

This plot show that after 10 h of data acquisition the PMT counts (see plot (a) in figure 4.1) dropped rapidly. For the beam current there is not a corresponding decrease in beam intensity. Also the  $x, y$  position (4.2) and the energy monitor of the beam do not show unexpected behavior, so we reject the possibility that the beam was not properly aligned to the target. For all the PMTs of this suspicious data run, the counts are equal to the offsets measured with the auto-calibration run. This indicates that there was a failure in the data acquisition program, which controls the NINO board. These data are rejected completely from the analysis. In plot 4.1 we observe abrupt variations of the asymmetry at 13.5h and 19h, while other variations are less appreciable. These data correspond to loss of the beam intensity for a short periods of time, and are rejected as outliers.

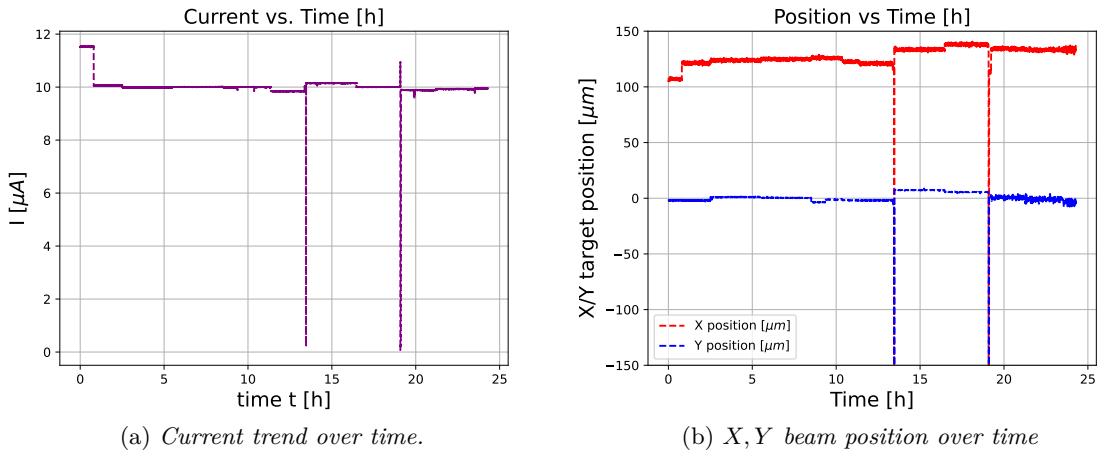


Figure 4.2: On the left, current trend versus time for all the runs acquired. On the right the X and Y position versus time.

Now we focus our attention on the correlated-difference values. These quantities, are used as independent variables for the fit, as explained before, are defined as

$$\delta x = \frac{(X_{up,1} + X_{up,2})}{2} - \frac{(X_{down,1} + X_{down,2})}{2}$$

and are calculated within each single event, to identify the differences with respect to the various quantities such as position, energy, etc., which correspond to different states of polarization. For each of these quantities a correspondent histogram is shown in figure 4.3. These plots are useful to quantify the stability of the beam: we expect that all the correlated differences are distributed around zero, which implies that there is no systematic difference when the beam has one polarization state with respect to the other. The mean  $\mu$  and the standard deviation  $\sigma$  of the distributions are reported in the table (4.1)

Every histogram is generated with 100 bins. For the current asymmetry, we discovered that the values of the VFCs resistance, which controls  $V_{ref}$  value, was set too high. The resolution of this monitor is low, compared to the others, as we can see in the corresponding histograms, where the data are distributed around isolated peaks. This suggest to increase  $V_{ref}$  of the VFCs, for the incoming experiment, to achieve a precision comparable with the other monitors.

Beam Parameters	$\mu \pm \sigma_\mu$	<i>sigma</i>
$X[\mu m]$	$3.1 \cdot 10^{-3} \pm 6 \cdot 10^{-3}$	0.17
$Y[\mu m]$	$2.4 \cdot 10^{-4} \pm 1.3 \cdot 10^{-3}$	0.04
$\theta_x[\mu rad]$	$2.2 \cdot 10^{-8} \pm 2.9 \cdot 10^{-7}$	$1.9 \cdot 10^{-5}$
$\theta_y[\mu rad]$	$-2.7 \cdot 10^{-9} \pm 9.6 \cdot 10^{-8}$	$6.5 \cdot 10^{-6}$
$E[keV]$	$0.0018 \pm 0.0005$	0.38
$I[ppm]$	$-1.23 \pm 0.06$	50.4

Table 4.1: Beam parameters table, in the second column the mean  $\mu$  with the standard deviation  $\sigma_\mu$  of the mean is shown. The third column is  $\sigma$ , the standard deviation of the distributions in figures 4.3.

Looking at the values of the mean and the corresponding error  $\sigma$  reported in the plots legend, we observe that the means of  $X, Y, \theta_x, \theta_y, E$  are compatible with 0. These results are encouraging: we are not able to identify a systematic difference between polarization +1 and -1. A systematic difference would have produced a value  $\mu$  shifted from zero, and a corresponding effect on  $A_n$ . With our assumption that the false asymmetries are well described by a linear model, observing that  $\mu$  is small and compatible with zero for all the parameters, together with the evidence that  $\delta q$  are distributed symmetrical around zero, leads to the cancellation of all the false asymmetries, as can be seen in equation 4.7 :

$$\bar{A} = A_n \cdot P + \overline{\delta I} + \overline{\delta_x} A_x + \overline{\delta_y} A_y + \overline{\delta_{\theta_x}} A_{\theta_x} + \overline{\delta_{\theta_y}} A_{\theta_y} + \overline{\delta_E} A_E = A_n \cdot P + \overline{\delta I} \quad (4.7)$$

We will discuss later, when we will introduce the fit results, whether our assumption reflects the reality. We assume that the only false asymmetry that has an effect is  $\delta I$ :  $\overline{\delta I} = -1.23 ppm$ , and we will subtract that to the final result:

$$A_n = \overline{A_{tot}} - \overline{\delta I}$$

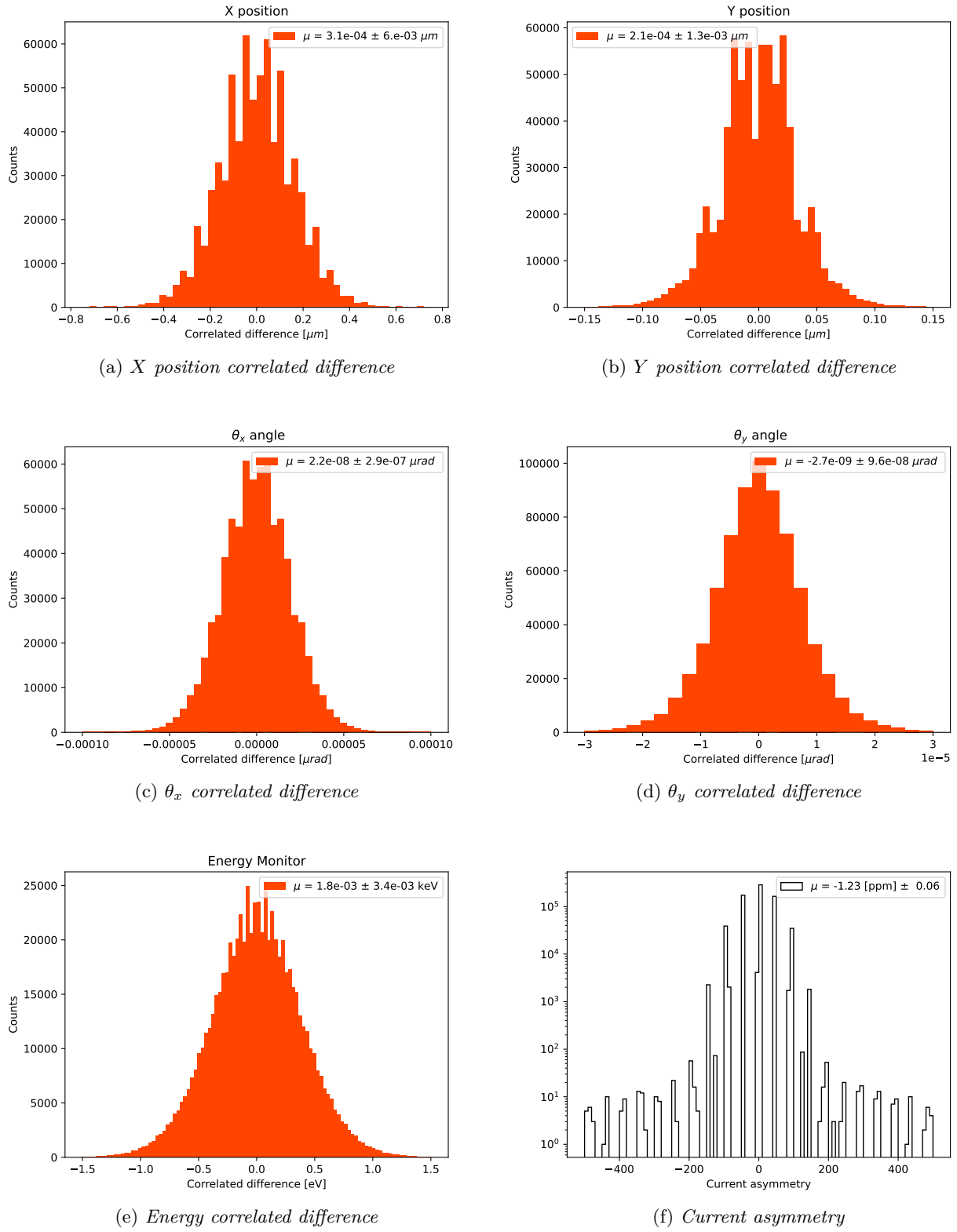


Figure 4.3: Histogram for the beam parameters.

### 4.3 Polarization Loss

After discussing the removal of the outliers, now will discuss in details the issue regarding the polarization of the beam. To observe a transverse asymmetry, it is essential to have a correctly polarized beam. Unfortunately, we found out that part of the data were acquired by mistake with a non-polarized beam. The reason is that during the second night of the experiment, MAMI operators who controls the quality of the beam, switched from polarized beam to non-polarized, unintentionally. These wrong data were acquired during the night of 2nd December and we discovered this problem only the next day. We had no indication of how many hours of beam were lost. Since this happened during the night, nobody could save the polarization measurement, and identify the runs affected by this problem. This issue introduces a big systematic error that decreases the measurement of  $A_n$ . To proceed in the analysis, it is important to identify the runs sharing this problem, otherwise the measurements are affected by a bias that is not possible to disentangle from other systematic effects related to the electronics system of the experiment. All the stabilization monitors were active and the data apparently show the same behaviour of the data with the correct polarization. We can not proceed with an arbitrary cut of the data, because there is the risk to cut off also good data or perform an incomplete removal. The next phase of the analysis is focused on describing a method used to identify the data taken with unpolarized beam and remove them from the analysis.

The procedure to identify the runs without polarization rely on the estimation of the correlation coefficient of the PMTs counts. For every event we have two type of polarization sequence. The polarization  $P$  of each sub-event is identified with  $+1$  and  $-1$ , that correspond to up and down  $P$ . This values are part of the data tree, and form a sequence  $p_i$  of the type:  $+1 - 1 - 1 + 1$ , where  $i$  is the index to the  $i$ -th sub-events analyzed. If the actual  $P$  is different from zero, we expect a difference in the number of scattered electrons between sub-events with different  $p_i$ , caused by the transverse asymmetry (see table 4.2).

sub-event	1	2	3	4	5	6	7	8
Polarity	+1	-1	-1	+1	+1	-1	-1	+1
PMT B0	101	99	98	102	100	99	97	103
Other PMT	...	...	...	...	...	...	...	...

Table 4.2: Example of the Polarity sequence and PMT counts that are saved in the analysis program. The values of the PMT counts given are for example.

This leads to a positive/negative correlation between the sequence  $p_i$  and the PMT data. In case of  $P = 0$ , the expected values for the correlation should be zero. We applied this strategy with the hope to identify the blocks of data with  $P = 0$ , also using the knowledge that the polarization was turned off at some point during the night. The correlation  $c$  between  $p_i$  and the PMT sequence  $N_i$  of counts is measured every  $t = 1h$ , corresponding to 45000 events. We plot the averaged correlation for detector A and B, and the correlation of the two detectors together (with the reverse sign for detector B) in figure 4.4.

If we observe that  $c$  is compatible with zero, we have an indication of the block of runs to be removed from the analysis. The values are reported in figure 4.4. The errors for each point are computed with the formula:

$$\sigma_c = \sqrt{\frac{1 - c^2}{N - 2}}$$

The plots show the expected values for the correlation coefficient, computed with a simple simulation, using the values of  $A_n = 22.5\text{ppm}$  and  $P = 0.79$  as an input. The simulation results are obtained following these steps:

- A sequence of the type  $+1, -1, -1, +1$  is generated, long 45000 events.

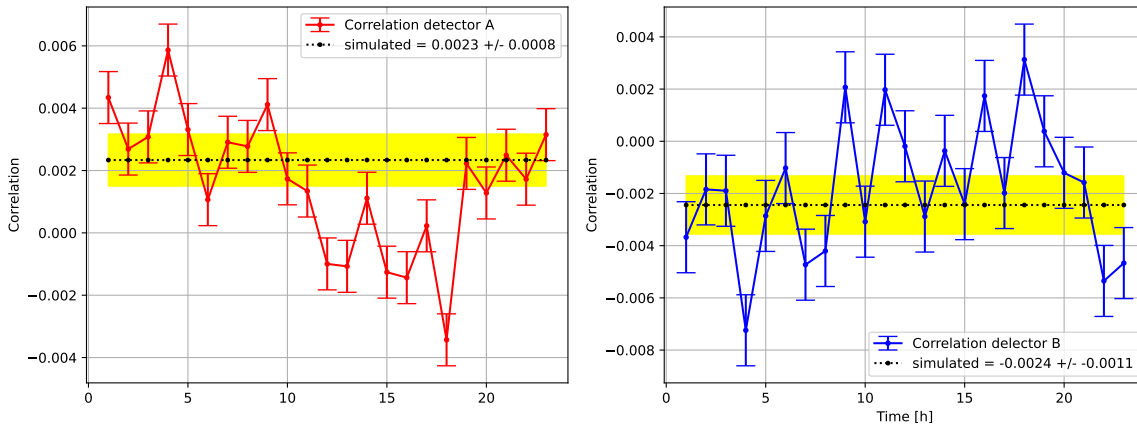


Figure 4.4: Correlation between the polarization sequence and the asymmetry data. The correlation are measured for each data run, 1 h long.

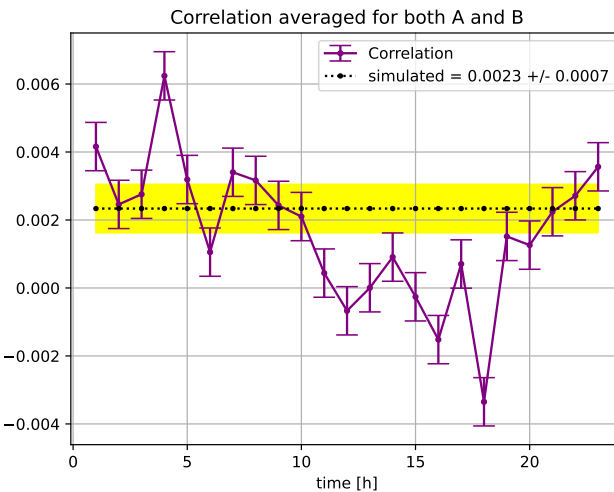


Figure 4.5: Correlation between the polarization sequence and the asymmetry data. The plot shows the overall result for the two detector combined, reversing the sign of the asymmetries of detector B, together with the values expected from a Monte Carlo simulation. In yellow the error band computed with the Monte Carlo.

- For each sub-event of the previous sequence, the PMT counts are generated: the counts are sampled from a gaussian distribution with  $\mu$  and  $\sigma^2$  equal to the values measured for both the detectors. To reproduce the correlation with the polarity sequence, the values are shifted accordingly by a factor  $\mu \cdot A_n \cdot P$
- The previous step is repeated 25 times, and for each iteration we compute and save the correlation between the polarity sequences and the counts.
- From the values saved, we compute the mean  $c$  (the dotted line in plot 4.4) and  $\sigma_c$ .

Looking at the plots, we observe for detector A a block of runs where  $c$  is compatible with 0, in contrast with the values expected from the simulation. Due to the higher error, the corresponding plot for detector B is not clear to interpret, however the plot on the right with the overall results for A and B confirms the evidence for A. This let us to identify the block of runs that show a behaviour compatible with  $P = 0$ . it is important to check that validity of this method seeing if the corresponding asymmetry is compatible with 0 (see figure 4.6).

The asymmetry values for this block of runs show an unexpected behaviour. For both detectors we observe negative values. The weighted mean for the two detector is :

- $A_B = -7 \pm 5$  ppm

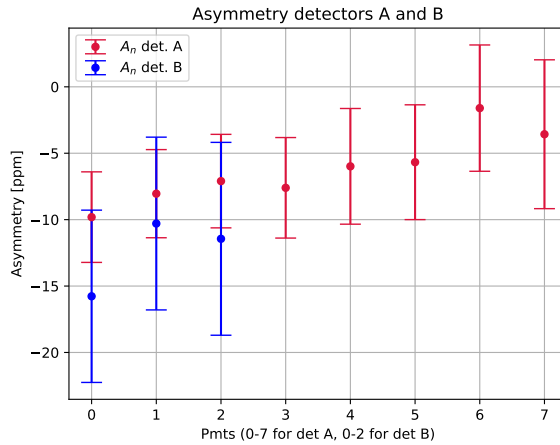


Figure 4.6: Raw-asymmetry computed for the block of runs with  $P = 0$ . Except for one PMT of detector A, all the values are compatible with 0 in  $1\sigma$ .

- $A_A = -5 \pm 2$  ppm

The values are not compatible with zero, but are compatible with each other. Therefore it is reasonable to not include this data in the main analysis, because we observe a negative asymmetry for both the detectors that is not compatible with the presence of a polarized beam.

#### 4.4 Fit with a Linear Model

Now we study the distribution of the asymmetries measured by the two detectors. Our main assumption is that the measured values are following a normal distribution, around the physical value  $A_n$ . We have produced several histograms for the measurements of every PMT (see figure 4.7,4.8). The data without polarization are not included in the histograms. For every histogram we use a gaussian function to fit the data, the reduced  $\chi^2$  is reported in table 4.3. We see a good agreement with the hypothesis of normally distributed data.

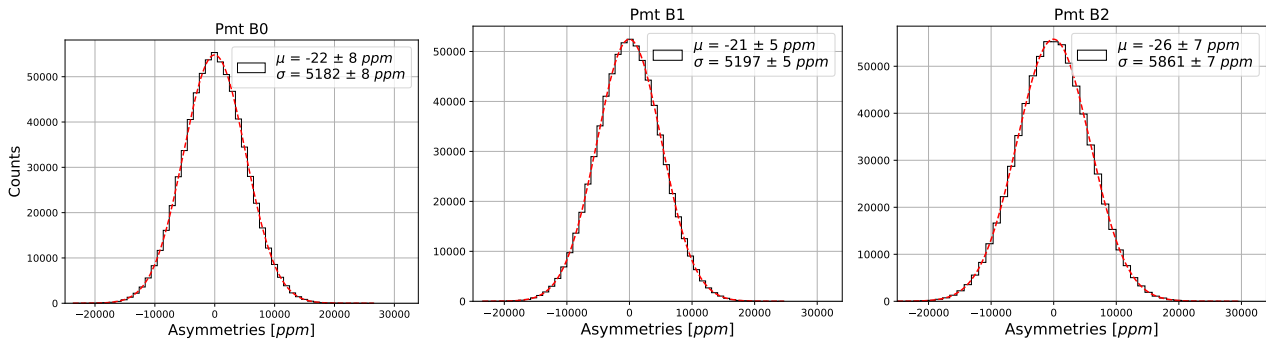


Figure 4.7: Histogram of the Asymmetry for Detector B. The Asymmetries are corrected removing the data without polarization. The raw asymmetries are multiplied by  $\frac{1}{P}$

Recalling equation 2.2, where we assumed that  $A$  is a normally distributed variable, now we can confirm our initial assumption. To extract the asymmetry  $A_n$  from the data, we assume a linear model where the asymmetries depend on the beam parameters, in the way we discussed in section 4.1. The false asymmetries are described with 5 parameters, that are  $A_x, A_y, A_{\theta_x}, A_{\theta_y}, A_E$ .

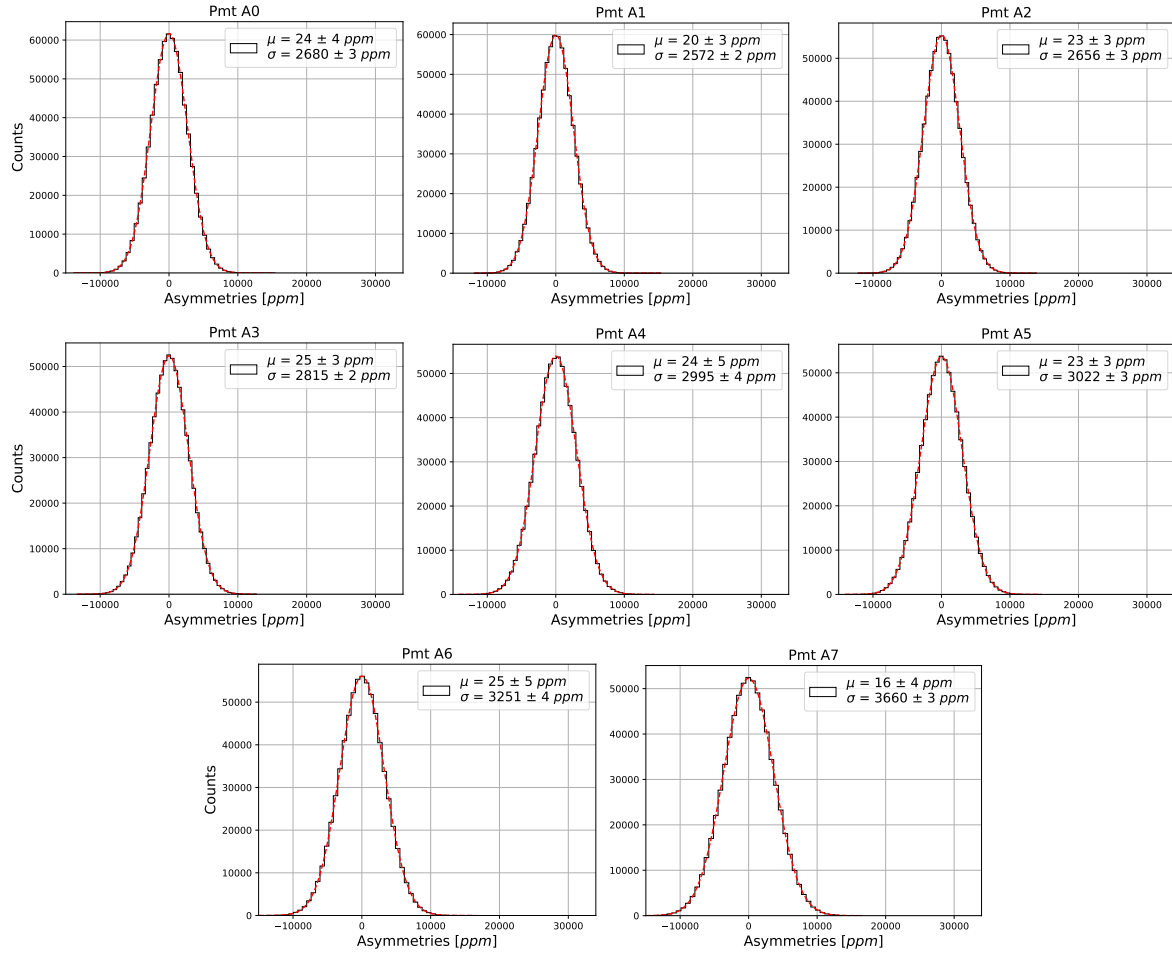


Figure 4.8: Histogram of the measured asymmetries of detector A. The Asymmetries are corrected removing the data without polarization. The raw asymmetries are multiplied by  $\frac{1}{P}$

Pmt	reduced $\chi^2$
B0	$1.2 \pm 0.2$
B1	$0.9 \pm 0.2$
B2	$1.2 \pm 0.2$
A0	$1.2 \pm 0.2$
A1	$0.7 \pm 0.2$
A2	$0.7 \pm 0.2$
A3	$0.9 \pm 0.2$
A4	$1.4 \pm 0.2$
A5	$0.7 \pm 0.2$
A6	$1.1 \pm 0.2$
A7	$1.7 \pm 0.2$

Table 4.3: Reduced  $\chi^2$  for the gaussian fit of the asymmetry data.

Before proceeding with the fit, it is interesting to study how  $A_n$  evolves increasing the data size. This can be seen by plotting the averaged values  $\bar{A}_n$  as the number of events increases, where the average is made on all data collected from time  $t = 0$  up to time  $t = t_1$ , as shown in figure 4.9.

These plots are useful to check that the asymmetries converge to a certain value, and that there are no steep variations that could be related to the presence of remaining outliers. We observe that the sign of the asymmetries for the two detectors are opposite, in agreement with what we expect from the different kinematics, with the sign of the asymmetry given by the sign of the projection of the cross product  $\vec{k} \times \vec{k}'$  along the axis orthogonal to the scattering plane. For detector A the cross product projection is positive, while for the detector B it is negative. The data are analyzed both

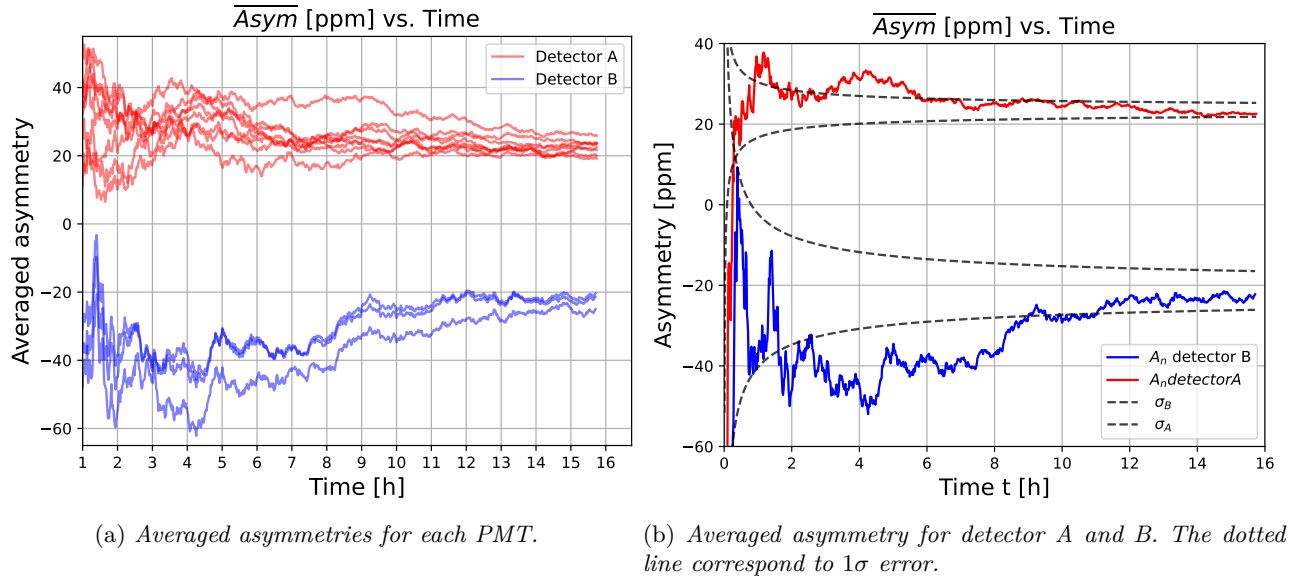


Figure 4.9: Plot of the Asymmetry versus time. The plot show the average over all the events collected from  $t = 0$  to  $t = t_1$ . Each line represents  $A_n$  measured for PMT (in blue detector B and in red detector A). The values are corrected for the beam polarization, multiplying by  $\frac{1}{p}$ . No further correction is applied.

using python libraries, and with a fit program implemented in the framework of this thesis. To analyze the data with python, it is used the *curvefit* function implemented in the python library *scipy*. We also implemented a dedicated program to interface directly to the analysis program, the fit program, that is written in *C++* code. The fit program implements the ordinary least square algorithm (OLS), a well known algorithm used in linear regression. The OLS algorithm is a basic algorithm, easy to implement and robust. In linear regression it is assumed that :

$$y = \vec{x} \cdot \vec{\beta} + \epsilon \quad (4.8)$$

$\vec{x}$  are the independent variables,  $\vec{\beta}$  are the parameters and  $\epsilon$  is a noise parameter, that is supposed to be gaussian (however, the robustness of the OLS algorithm allows relaxing this request). Another important assumption is that the linear variables are not correlated. This last requirement is particularly important, as correlated data can not be processed with either of the two algorithms used. Before proceeding with the fit, it is necessary to verify this assumption. The correlation matrix for the beam parameters is reported in a table 4.4.

	$X$	$Y$	$\theta_x$	$\theta_y$	$E$	$I$
$X$	1	-0.02	-0.99	0.06	0.04	-0.03
$Y$	-0.02	1	0.01	-0.65	0.01	-0.02
$\theta_x$	-0.99	0.006	1	-0.005	-0.05	0.03
$\theta_y$	0.06	-0.65	-0.05	1	-0.003	0.03
$E$	0.04	0.005	-0.05	-0.003	1	0.26
$I$	-0.03	-0.02	0.03	0.03	0.26	1

Table 4.4: Correlation coefficient between beam parameters.

The correlation between  $(\theta_x, X); (\theta_y, Y)$  are high compared to the other correlation coefficients.

The plots in figure 4.10 confirm the linear dependence between the parameters. For the  $\theta_x$  versus the  $X$  position the data are distributed on a line, with complete anti-correlation. For the  $\theta_y$  versus  $Y$ , the data are distributed following parallel lines, that have the same angular coefficient but different offsets. The lines are equally spaced, meaning that the beam parameter  $\delta Y$  is translated, for a fraction of the events, by a multiple of some quantity  $\delta \theta_y$ . With the linear fit we estimate that

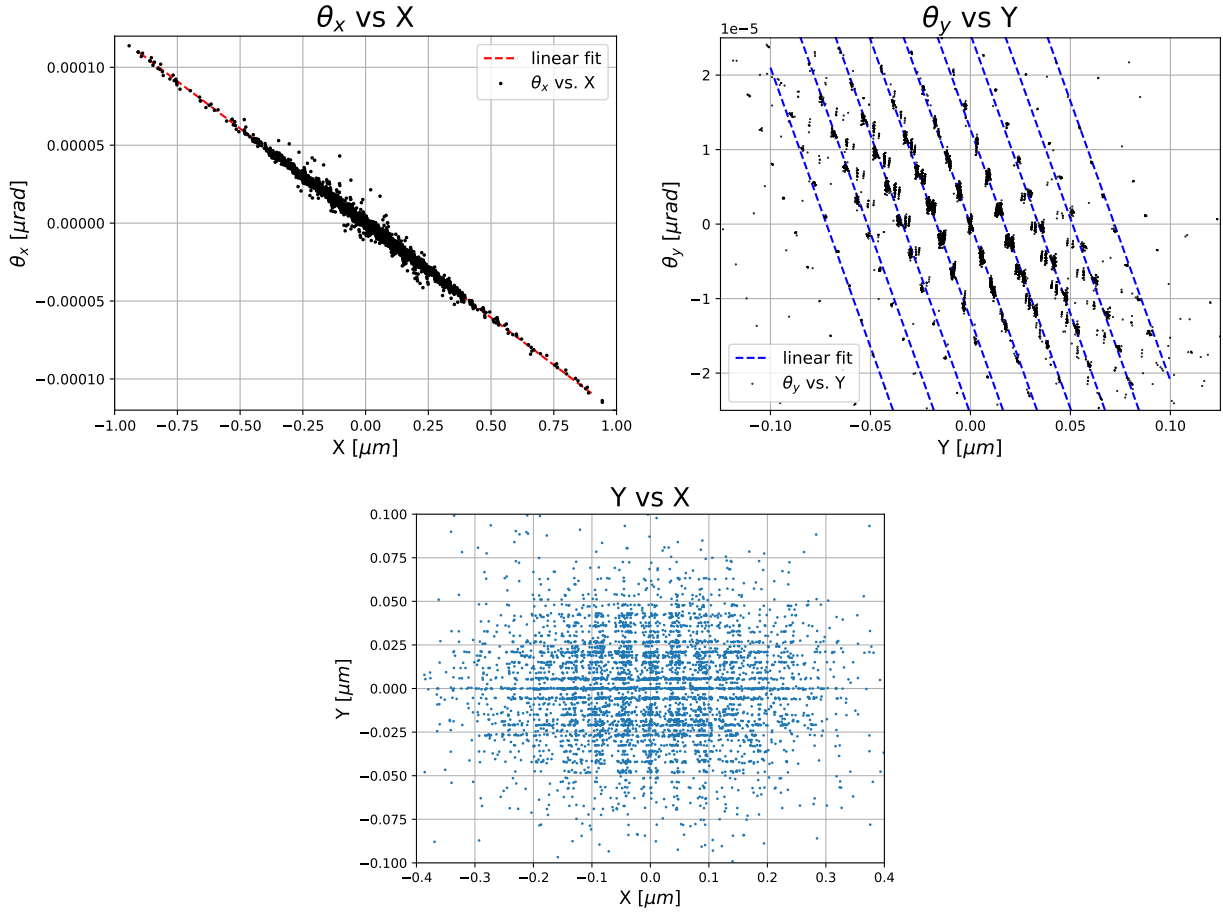


Figure 4.10: Correlation plots of positions and angles.

$\delta l_y = 0.017 \pm 0.001 \mu\text{m}$ . This effect could reproduce the data structure that we observe in plot *b* of figure 4.10.

It is clear that we have to modify the model to fit the data. We decided to include as linear independent variables only :  $I, X, Y, E$ . Plotting the asymmetry  $A$  versus each of the measured beam parameters is helpful for a better visualization of the data, particularly to see how the asymmetry depends on them.

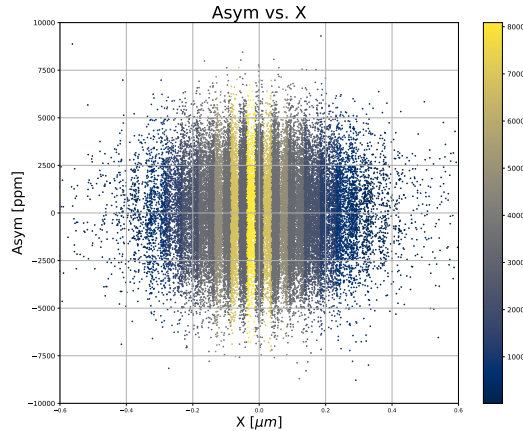


Figure 4.11: Detector A asymmetries versus X beam position. Because of the statistical uncertainties, it is not possible to visualize a linear dependence in the data. Each dot is colored depending on the density of points.

Unfortunately, the statistical error associated to the asymmetry is too high to appreciate whether there is a linear dependence in the data. For example, in figure 4.11 we plot the asymmetries  $A$  versus  $X$ . A different approach is to divide the  $x$  axis in small intervals, and average the asymmetries in each interval. The result are shown in figure 4.12, where each point represents the overall asymmetry for a particular interval of  $X$ ,  $Y$  or  $E$ .

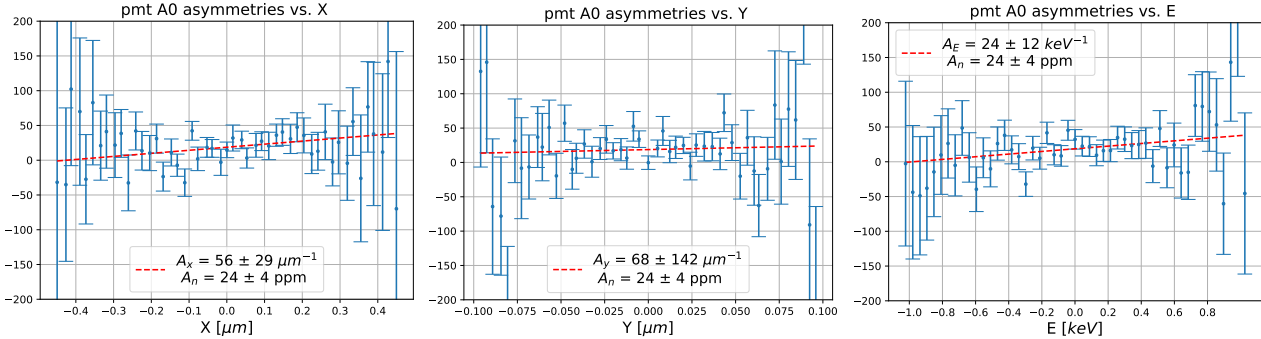


Figure 4.12:  $A$  versus  $\delta x$ ,  $\delta y$  and  $\delta E$ . The plot are generated with 50 equally spaced bins. The red line is the best fit with a linear model.

We report for brevity only the values for PMT A0 of detector A. In this case is simpler to identify the presence of a linear dependence in the data. The errors are computed with the formula defined in equation 2.2, considering each interval separately. Another approach that we used to further reduce the fluctuations related to the statistical error of  $A_n$  is an additional average over all the PMTs of each detector. The result is shown in figure 4.13.

This procedure decreases the error of a factor  $\sqrt{8}$  for detector A and  $\sqrt{3}$  for detector B. However, this does not take into account the different linear dependencies on the beam parameters for the various PMTs, and therefore is not immune from a possible bias. We have explored different models to describe the asymmetry dependence on beam parameters. The first one is the linear model:

$$A = A_x \delta x + A_{phys} \quad (4.9)$$

For  $X$  and  $Y$  positions, we tried to use a 5th order polynomial:

$$A = c \delta x^5 + A_x \delta x + A_{phys} \quad (4.10)$$

While for the energy monitor, we tried a 3rd order polynomial:

$$A = c \delta E^3 + A_E \delta E + A_{phys} \quad (4.11)$$

The choice of an odd exponent is due to the observation that  $A$  increases near the edges of the plot with opposite sign. The values of the fit parameters are reported in the plots of figures . The  $\chi^2$  of the fit are reported in table 4.5

detector A	$X$	$Y$	$E$
linear fit $\chi^2_{17}$	99	59	94
alternative model $\chi^2_{16}$	76	55	78

Table 4.5:  $\chi^2_{ndf}$  for the different models used to fit the data show in figure 4.13

The  $\chi^2$  values are higher than the expected and we observe that the values for the model 2 are lower than the ones of linear fit. This high values can be explained with two considerations: the first one is that this procedure of averaging the data based on  $x$  interval leads to the loss of information that can influence the fit, the second consideration is that we are ignoring the possible error in the determination of  $\delta x$ . Despite of this, we observe that using a model with more complicated dependencies does not change the values of  $A_{phys}$ . Therefore we do not see a strong reason to change the linear model. The model that is used to extract the asymmetry is given in equation 4.12.

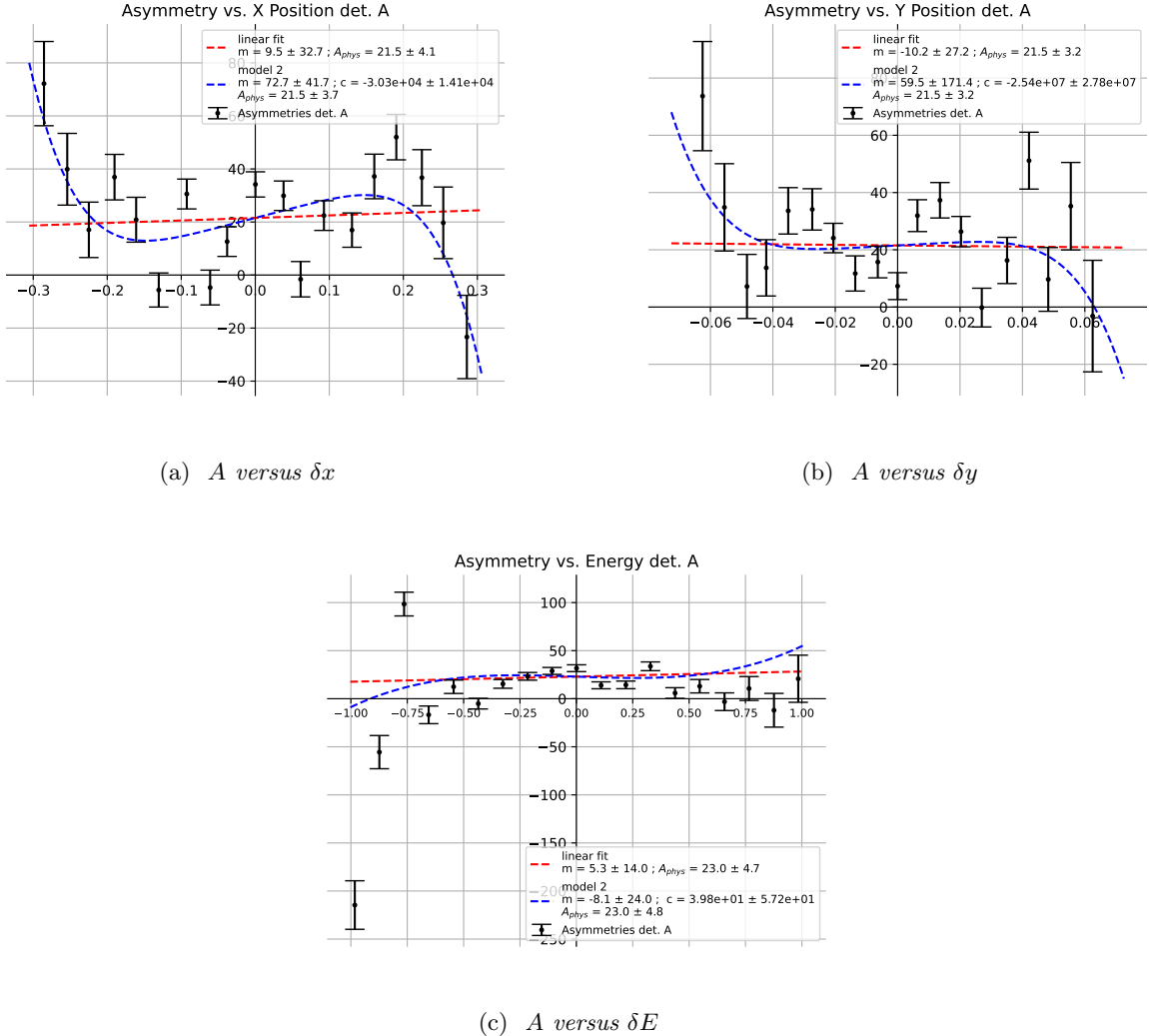


Figure 4.13: Averaged asymmetries versus the beam parameters  $\delta X$ ,  $\delta Y$  and  $\delta E$ . The x axis is divided in 19 intervals, and for each of them we average the asymmetries  $A$ . The linear model is the red line, the second used to fit the data is a polynomial, represented in blue.

$$A_{tot} = A_{phy} \cdot P + \delta_I + A_x \delta x + A_y \delta y + A_E \delta E \quad (4.12)$$

the result of the fit are reported in table 5.2, together with the final result of the asymmetry for detector A and B.

## 4.5 False Asymmetries

In the data analysis, the values of the false asymmetries have been treated as parameters of the linear fit. In this section we will investigate how we can obtain another different estimations, useful to check the validity of all the process of analysis of the data.

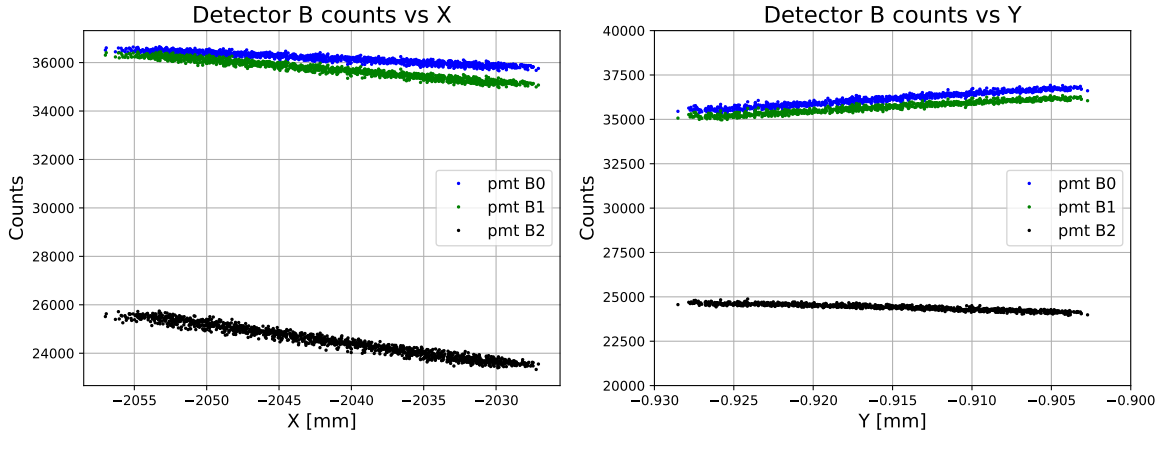
For  $\frac{dA}{dX}$  and  $\frac{dA}{dY}$ , we conceptually exploit the possibility of varying the position of the beam on the target, as we did during one of the calibration phases. Using the same *wobbler* 16 we asked MAMI to slowly change the beam position on the X and Y monitor. The change in position has the effect to modify the rates for the two detector, and from them it is possible to extract estimate the two false asymmetries related to the beam position. Now we will see how the two quantities are related. From the plot 4.14 we see that the counts are changing linearly with the beam position, so we assume that the  $N$  are given by

$$N(x, \dots) = N_0 + m \cdot (x - x_0)$$

it is clear that the linear model has limits, and at some point the electron will be deflected completely out of the detector, with the counts falling rapidly to zero. However, the magnets used to deflect the beam are producing small variation in the position, on the order of hundredths of a millimeters. Let's suppose that the beam position for two sub-events is  $x_1$  and  $x_2$ , we can calculate the asymmetry between the two events, taking care of the possible effects due to the different position. We write explicitly:

$$\text{Asym} = \frac{N(x_1) - N(x_2)}{N(x_1) + N(x_2)} = \frac{N_0 + m \cdot (x_1 - x_0) - N_0 - m \cdot (x_2 - x_0)}{N(x_1) + N(x_2)} = \frac{m}{2N_0 + m \cdot (x_1 + x_2) - 2mx_0} (x_1 - x_2) \quad (4.13)$$

In this equation three different parameters appear:  $N_0$  is the offset of the linear model,  $m$  is the angular coefficient, or the slope, and  $x_0$  is the initial position respect to which we compute the position variation. The first two terms are obtained by a linear fit, while  $x_0$  is fixed conveniently.



(a) Plot for slow variation in  $x$  direction for detector B.  
(b) Plot for slow variation in  $x$  direction for detector B.

Figure 4.14: Plot of the PMT counts versus the  $X$  position. The  $X$  position was slowly changed during the acquisition.

If the values  $x_1$  and  $x_2$  are distributed symmetrically<sup>1</sup> We can simplify the denominator deleting the term  $m \cdot (x_1 + x_2)$ , fixing  $x_0 = \frac{x(1)+x(2)}{2}$ .

$$\text{Asym} = \frac{m}{2N_0} (x_1 - x_2) \quad (4.14)$$

The term in front of  $(x_1 - x_2)$  can be compared to  $\frac{dA}{dX}$ . For  $N_0$ , the offset, we substitute the averaged value counts of each PMT for the polarized beam acquisitions. The data are reported in the table 4.6:

The values for the false asymmetries obtained with this method are:

These values are not in agreement with  $A_x$  and  $A_y$  obtained from the fit (5.2). This may be due to the high correlation with the  $\theta_x$  beam parameter. The negative correlation with  $\theta_x$  means that when  $\delta X$  increases  $\delta\theta_x$  decreases, and then the false asymmetries combined together. Using linear regression, it is not possible to disentangle the effects of the correlation in the data, and therefore the corresponding coefficient of the fit are not reliable.

<sup>1</sup>In the same way of the beam parameter difference, shown in figure 4.3

PMT	Detector A	Detector B
PMT 0	63733	17609
PMT 1	67262	17514
PMT 2	59782	14055
PMT 3	51736	
PMT 4	39057	
PMT 5	39667	
PMT 6	32768	
PMT 7	23593	

Table 4.6: Average counts per pmt, for time length of 20 ms.

'PMT'	$A_x \text{ } \mu\text{m}^{-1}$	$A_y \text{ } \mu\text{m}^{-1}$
B0	692	795
B1	395	682
B2	289	601
A0	233	533
A1	223	518
A2	202	493
A3	190	473
A4	211	503
A5	214	506
A6	217	510
A7	220	514

Table 4.7: Values for the false asymmetry, computed with the slow horizontal and vertical variation mode.

#### 4.5.1 Energy Asymmetry

For the energy asymmetry, a different method is necessary. We directly compute the Mott cross-section of the electron-carbon elastic scattering, and from that we can derive the false asymmetry due to energy variation. We start from the formula of the expected rates:

$$\frac{\text{events}}{\text{time}} = n_e N_t v_e \frac{\partial \sigma}{\partial \Omega} (\Delta \Omega_a) \epsilon \quad (4.15)$$

Where:

- $n_e$  electron density of the beam.
- $N_t$  Number of scattering centers of the carbon target.
- $v_e$  electron speed.
- $\Delta \Omega_a$  solid angle acceptance of the spectrometers.
- $\epsilon$  detector efficiency.

We do not need to compute directly the expected rate for the two detectors, because some terms cancel out when substituted in the formula for the asymmetry, the only relevant term is the cross section:

$$A = A_n + \frac{\sigma(E_1) - \sigma(E_2)}{\sigma(E_1) + \sigma(E_2)}$$

Because  $\Delta \Omega_a$  is a common term in the numerator and in the denominator, we can simplify the expression and substitute  $\sigma$  with  $\frac{\partial \sigma}{\partial \Omega}$ . The Mott cross section is given by the formula below:

$$\frac{\partial\sigma}{\partial\Omega} = \frac{Z^2\alpha(\hbar c)^2}{E^2\sin^4(\frac{\theta}{2})} \cdot \frac{E'}{E} \cdot \cos(\frac{\theta}{2}) \cdot F^2(\vec{q}) \quad (4.16)$$

Where the first term is the Rutherford cross-section, the second term represent the recoil of the nucleus, the third terms is the  $\cos(\frac{\theta}{2})$ , and the last term is the nucleus form factor. The Recoil term can be written:

$$\frac{E'}{E} = \frac{1}{1 + \frac{E}{Mc^2}(1 - \cos(\theta))}$$

With this final substitution we can rewrite the Mott cross section as:

$$\frac{\partial\sigma}{\partial\Omega} = \frac{D}{AE^2} \cdot \frac{1}{1 + EC} \cdot B \cdot F^2(\vec{q})$$

Where  $D = Z^2\alpha((\hbar c)^2)$ ,  $A = \sin^4(\frac{\theta}{2})$  and  $B = \cos(\frac{\theta}{2})$ . To compute the false asymmetry related to energy, we always assume that for small energy variation, a first order approximation is valid:

$$\sigma(E_1) \simeq \sigma(E_0) + \frac{\partial\sigma}{\partial E}(E_1 - E_0)$$

The approximations is done for small variations around the beam energy, which is 570 MeV. Now it is possible to compute the false asymmetry, the searched expression is:

$$A_E = \frac{\partial\sigma}{\partial E \partial\Omega} \cdot (2 \frac{\partial\sigma}{\partial\Omega})^{-1} \quad (4.17)$$

We compute the above formula with the constant A,B,C,D defined in 4.16.

$$A_E = -\frac{1}{2} \frac{2 + CE_0}{E_0 + E_0^2 C} \quad (4.18)$$

Applying the above formula, we end with  $A_E = -1.75 \frac{\text{ppm}}{\text{keV}}$ . We can compare this result with the values obtained from the fit, that are reported in table 5.2. There is at least an agreement on the sign, with an expected negative effect related to the beam variation. However, the false asymmetries from the fit are one order of magnitude higher than the values computed here. An explanation could be that the energy variation is correlated to other beam parameters, or effects that are not considered in this analysis. Usually correlated data alters the result of the regression algorithms, which are not able to estimate the value of the coefficients. Looking at the values reported in table 4.4, we observe a positive correlation between current and energy. Even if the correlation is not high, it still might cause a combination of effects which can be responsible for the lower values of  $A_e$  measured with the fit. Since it is not possible to compute analytically the correlation between the beam parameters parameters, the linear fit seems to be an easier method. An alternative approach may include Monte Carlo simulations of the beam, to take care of possible correlation between the various beam parameters, which in contrast are computationally expensive, compared to linear regression.

## 4.6 Rates on Lead

After all the calibrations are done, we proceeded with the measurement of the rates on lead target, one of the objectives of the experiment. The lead target installed is made of a thin layer with a thickness of 0.5 mm, and it is not isotopically pure. We took 14 acquisitions lasting  $\simeq 2,5$  minutes, which corresponds to 6950 events. For each of these acquisitions we set the beam current at different values, ranging from 10  $\mu\text{A}$  to 22  $\mu\text{A}$  of intensity. The rates are then reported as a function of the current and linear model is used to fit the data.

We fit using a linear model the data. The angular coefficient  $m$  and the offset  $q$  are reported in the table 4.8 for each PMTs of the two detectors.

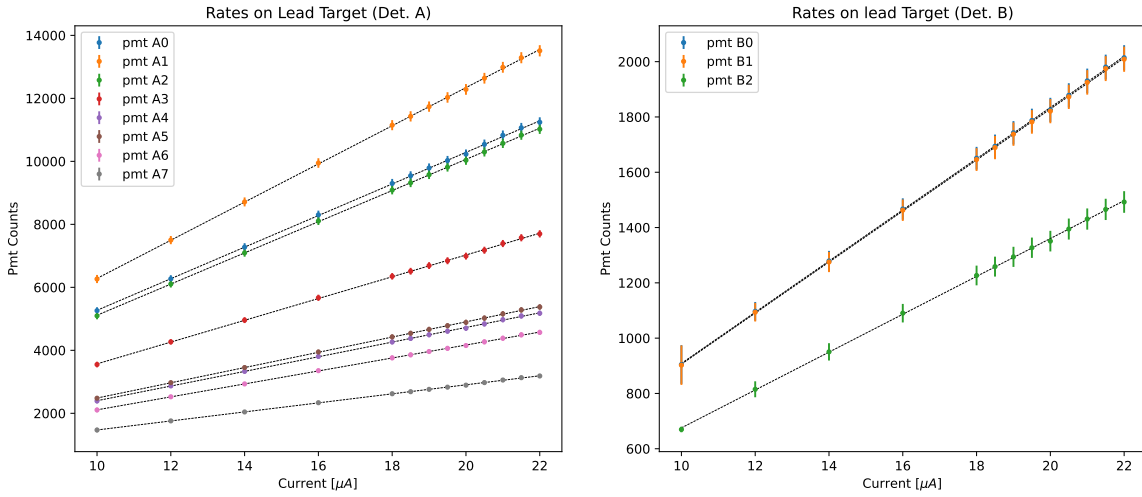


Figure 4.15: rates on lead Target as function of the beam current. The rates for each PMT of detector A (on the left), and detector B (on the right) are reported.

PMT	$m [\mu\text{A}^{-1}]$	$q$	$\chi^2$ (dof = 9)
A0	501.4 +/- 2.2	257 +/- 40	13.8
A1	605.8 +/- 2.3	226 +/- 42	13.4
A2	495.0 +/- 1.5	163 +/- 27	7.0
A3	345.7 +/- 1.6	113 +/- 30	12.0
A4	232.6 +/- 0.9	74 +/- 16	5.4
A5	242.0 +/- 0.7	66 +/- 14	3.5
A6	205.8 +/- 0.7	52 +/- 12	3.1
A7	143.4 +/- 0.5	36 +/- 9	2.3
B0	92.6 +/- 0.3	-17 +/- 6	2.1
B1	92.3 +/- 0.3	-17 +/- 6	1.9
B2	68.5 +/- 0.3	-9 +/- 6	2.8

Table 4.8: Lead rates, the values are measured for a target width of 0.5 mm.

The PMT Counts with this target, increase from 100 counts for detector B to 500 counts every 1  $\mu\text{A}$ . It is interesting to recover the formula of the experimental standard deviation  $\sigma$  associated to the asymmetry distribution:

$$\sigma = \sqrt{\frac{1}{2N \cdot n}} \quad (4.19)$$

Where  $N$  is the counts per sub-event, while  $n$  is the number of event analyzed. Let's suppose that we want to obtain, for each PMTs, a statistical error not greater than 4,8 ppm. With this accuracy, the overall result A will have an error given by  $\frac{4.8 \text{ ppm}}{\sqrt{8}} \simeq 1.7 \text{ ppm}$ , equal to the statistical error that we have obtained for the measurement of  $A_n$  with  $^{12}\text{C}$  ( see table 5.4) while for detector B an overall result of 2.8 ppm. We have computed the time needed to achieve this accuracy for both detectors, given in total hours of experiment. This values are arbitrary: as shown in chapter 5, the transverse asymmetry on carbon has been measured with the same accuracy.

The amount of time needed to obtain this accuracy with carbon is roughly 15h with 10  $\mu\text{A}$ . The same measurement with lead will need 23 times the time accumulated for Carbon. This is due to the fact that the target thickness for lead target must be smaller than the target thickness for carbon. Because the atomic number of lead is greater than carbon, the amount of radiation during the experiment is exponentially higher. During the experiment, the A1 experimental hall is constantly monitored, the radiation level can not exceed a certain threshold. This imposes an important constrain to the maximum target thickness. As a consequence, despite the Mott cross section increases as  $Z^2$  and favor heavy nuclei, the radiation levels dictates to work with lower beam currents and smaller

current I $\mu\text{A}$	T [h] Det A	T [h] Det B
10	344	1487
12.5	277	1185
15	232	985
17.5	199	843
20	175	737

Table 4.9: Estimated time needed for the upcoming experiments to measure the transverse asymmetry for Lead with an aimed precision of  $1.7 \text{ ppm}$  for detector A and  $2.8 \text{ ppm}$  for detector B.

thicknesses for the target. Another experimental problem is the low melting point of  $Pb$ . To prevent the target from melting, the beam current intensity must be controlled in order to reduce the amount of heat produced by the beam. For the lead target a cooling system with a mixture of alcohol and water at  $0^\circ C$  degree is installed. In addition, the beam position is continuously varied, following a Lissajous curve, in order to spread the beam hitting points. This is done using fast bending magnets, with a frequency much higher than the frequency of the polarization sequence, in order to avoid possible false asymmetry induced by the change in the positions. The combinations of all these factors makes the measurement with lead more challenging. However the  $A_n$  is valuable, in order to cancel possible systematics effect for the parity violating scattering, besides the fact that measurements made by PREX collaboration [18] do not agree with the theoretical prediction, suggesting the need to repeat the measurement independently.

# Chapter 5

## Final Result and Conclusion

In this chapter we show the result obtained for the transverse asymmetry measured on carbon during the experiment. The first result that we report is the values of asymmetry  $\bar{A}_n$  computed as the average over all the events, after applying the various cut discussed before to remove wrong data and outliers. The values reported in tables 5.1a 5.1b are corrected for beam polarization ( $A_{raw} \times \frac{1}{P}$ ) and for the current asymmetry:

$$\bar{A}_n = \frac{\bar{A}_{raw}}{P} - \bar{A}_I \quad (5.1)$$

The sign of the asymmetry is given by the sign of the cross product between the momenta  $\vec{k}$  of the incident electron and  $\vec{k}'$  the scattered electron. It is positive for detector A and negative for detector B, according to the kinematics. In section 3.3.6 we have discussed possible effects that arise from the presence of an offset when we consider the linearity of the PMTs as a function of the beam current variation. This systematic effect tends to decrease the reconstructed values of the asymmetry by a factor  $c$ , computed in equation 3.12. The predicted value of  $c$  is reported in table 5.1c; we also compute the ratio between the final asymmetries with and without subtracting the offset, that is shown in table 5.1c. The values of  $c$  computed in these two ways are coherent.

PMT	$\bar{A}_n$ [ppm]	$\sigma$	PMT	$\bar{A}_n$ [ppm]	$\sigma$	PMT index	$\bar{A}_{notcorrected}/\bar{A}_{corrected}$
B0	-19.92	7.7	B0	-20.61	8	B0	0.97
B1	-19.0	7.8	B1	-19.69	8	B1	0.96
B2	-23.42	8.7	B2	-24.13	9	B2	0.97
A0	18.8	3.7	A0	24.55	4.2	A0	0.77
A1	16.05	3.4	A1	22.54	4.1	A1	0.71
A2	18.45	3.7	A2	24.37	4.3	A2	0.76
A3	19.0	4.2	A3	23.49	4.7	A3	0.81
A4	20.84	5.0	A4	24.21	5.4	A4	0.86
A5	22.83	4.9	A5	26.39	5.3	A5	0.87
A6	17.49	5.5	A6	19.82	5.9	A6	0.88
A7	19.24	6.6	A7	20.97	6.9	A7	0.92

(a) Asymmetries, with offset not subtracted.

(b) Asymmetries with offsets subtracted

(c)  $c$  factor, as defined in equation 3.12

Table 5.1: Averaged asymmetries over all the events. The values are corrected subtracting  $\bar{A}_I$  and considering the effective polarization  $p$  of the beam

The results reported in table 5.1b are shown in plot of figure 5.1. To obtain a final asymmetry for detector A and B, the asymmetries for each plot are averaged using the formula:

$$A_n = \sum_{i=0}^{n_{PMT}} \frac{w_i A_i}{\sum_{i=0}^{n_{PMT}} w_i} \quad (5.2)$$

With  $w_i = \frac{1}{\sigma_i^2}$ .

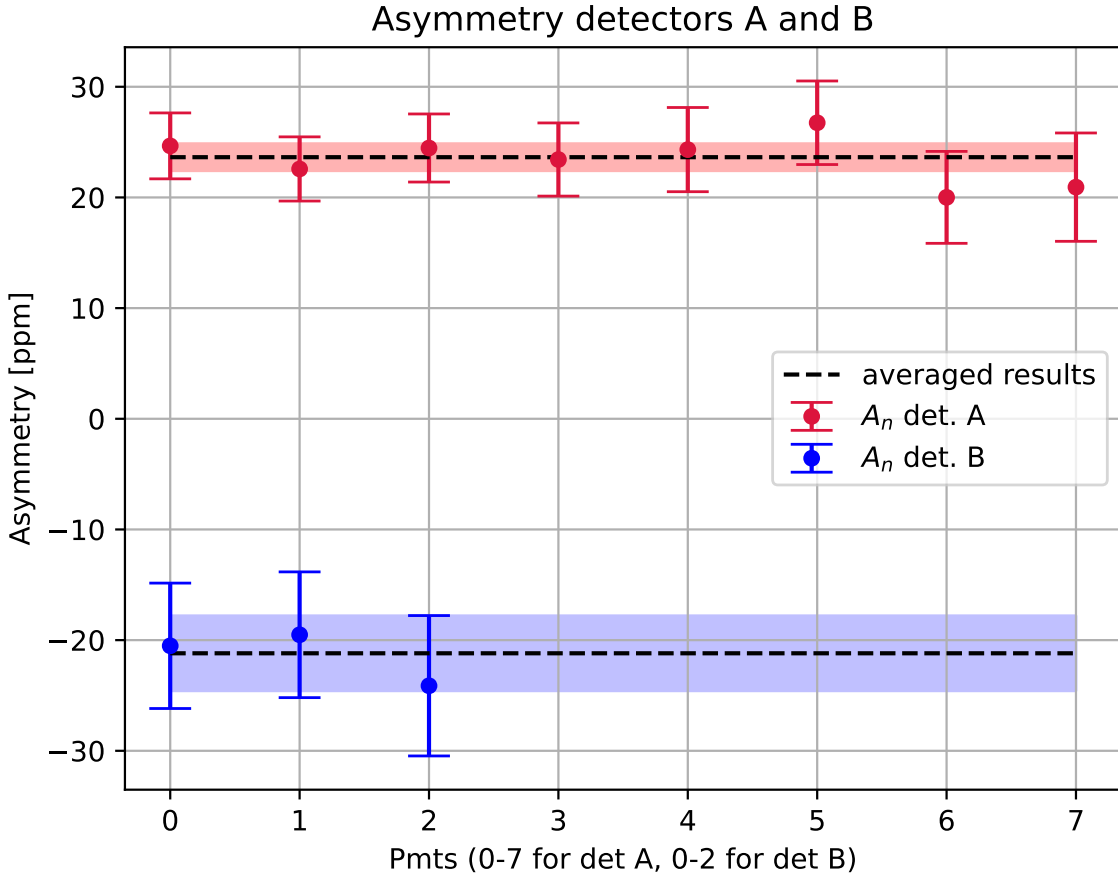


Figure 5.1: Plot of  $\bar{A}_n$ . The result are corrected by the beam asymmetry current and polarization. The black line represent the overall value  $A_n$  computed with the formula 5.2.  $\overline{\delta I}$ .

The result for the two detectors are in agreement with the expected sign and compatible with the previous measurement performed at MAMI [21].

- Asymmetry for detector A,  $A_A = 23.6 \pm 1.7$  ppm.
- Asymmetry for detector B,  $A_B = -21 \pm 5$  ppm.

## 5.1 Linear Model Result

The result obtained from the linear fit of the asymmetries versus the beam parameters are reported here, together with the false asymmetry values. The final parameters for the model are  $X$ ,  $Y$ ,  $E$ , and the current asymmetry  $I$  is subtracted for each event:

$$A_{tot} - A_I = A_n \frac{1}{P} + A_x \delta X + A_y \delta Y + A_e \delta E \quad (5.3)$$

The result for detector A:

PMT	$A_n$	$A_x$	$A_y$	$A_e$	$\chi^2_{reduced}$
A0	$24 \pm 4$	$67 \pm 27$	$-8 \pm 135$	$-22 \pm 12$	$1.000 \pm 0.002$
A1	$23 \pm 4$	$9 \pm 26$	$-85 \pm 130$	$-10 \pm 11$	$1.001 \pm 0.002$
A2	$23 \pm 4$	$-12 \pm 27$	$-24 \pm 134$	$-21 \pm 12$	$1.000 \pm 0.002$
A3	$23 \pm 5$	$14 \pm 29$	$-180 \pm 142$	$-31 \pm 12$	$0.999 \pm 0.002$
A4	$25 \pm 5$	$50 \pm 31$	$-85 \pm 151$	$-26 \pm 13$	$1.000 \pm 0.002$
A5	$27 \pm 5$	$31 \pm 31$	$198 \pm 152$	$-37 \pm 13$	$1.001 \pm 0.002$
A6	$20 \pm 5$	$7 \pm 33$	$142 \pm 164$	$-31 \pm 14$	$1.000 \pm 0.002$
A7	$20 \pm 6$	$6 \pm 38$	$78 \pm 184$	$-14 \pm 16$	$1.001 \pm 0.002$

Table 5.2: Fit result with the linear model, for detector A.

the result for detector B:

PMT	$A_n$	Bx	By	Be	$\chi^2_{reduced}$
B0	$-20 \pm 8$	$-59 \pm 40$	$-25 \pm 187$	$-14 \pm 17$	$1.000 \pm 0.002$
B1	$-20 \pm 8$	$-64 \pm 40$	$47 \pm 188$	$-22 \pm 18$	$1.000 \pm 0.002$
B2	$-24 \pm 9$	$-65 \pm 46$	$-170 \pm 211$	$-61 \pm 20$	$1.000 \pm 0.002$

Table 5.3: Fit result with the linear model, for detector B.

The final results of the transverse asymmetry for the two detectors, for a  $Q^2 = 0.04 \text{ GeV}^2$  are shown in table 5.4

DETECTOR	$A_n$
A	$23.1 \pm 1.7$
B	$-21 \pm 5$

Table 5.4: Overall result for detector A and B.

the values obtained from the linear fit, and the values obtained with a simple data averaging do not differ much from each other. This implies that the contribution due to the false asymmetries is generally small. This indicates that the beam stabilization decreased the correlated differences due to the different polarization of the beam, and confirm the goodness of the measurement of the transverse asymmetry at MAMI accelerator.

## 5.2 Data Without Polarization

In this section we report the result obtained for the block of runs that showed an unexpected behaviour, compatible with the absence of a transverse polarization of the beam. This data are analyzed in the same way as good data, and the result are reported in the table 5.5

The overall values are  $-5 \pm 2$  for detector A and  $-8 \pm 5$  for detector B. The two values are compatible with each other and much smaller than the values obtained with polarization.

PMT	An	Ax	Ay	Ae	$\chi_{reduced}$
A0	-12 +/- 5	88 +/- 30	38 +/- 154	-25 +/- 13	1.000 +/- 0.002
A1	-9 +/- 5	44 +/- 29	57 +/- 149	-23 +/- 13	1.001 +/- 0.002
A2	-5 +/- 5	17 +/- 30	111 +/- 154	-38 +/- 13	1.000 +/- 0.002
A3	-7 +/- 6	47 +/- 32	85 +/- 163	-51 +/- 14	1.000 +/- 0.002
A4	-5 +/- 6	38 +/- 33	192 +/- 171	-46 +/- 15	0.999 +/- 0.002
A5	-4 +/- 6	67 +/- 34	177 +/- 173	-52 +/- 15	1.000 +/- 0.002
A6	-1 +/- 7	70 +/- 36	-101 +/- 186	-54 +/- 16	1.000 +/- 0.002
A7	-1 +/- 7	25 +/- 41	-494 +/- 209	-41 +/- 18	1.000 +/- 0.002
B0	-13 +/- 11	48 +/- 58	-48 +/- 294	14 +/- 26	1.001 +/- 0.002
B1	-11 +/- 11	51 +/- 58	44 +/- 295	-3 +/- 26	1.001 +/- 0.002
B2	-7 +/- 12	90 +/- 65	-166 +/- 333	-9 +/- 30	1.000 +/- 0.002

Table 5.5: Analysis result for the data with polarization loss

### 5.3 Conclusion and Outlook

The transverse asymmetry for  $^{12}C$  target, at a  $Q^2 = 0.04 \text{ GeV}^2$  has been measured with the new counting-based data acquisition systems. The values are in agreement with the theoretical sign due to the different scattering kinematics of detector A and B. These measurement are in agreement with the ones reported in [21], which are  $23.9 \pm 1(\text{stat}) \pm 0.7(\text{syst}) \text{ ppm}$  for detector A and  $-21.9 \pm 1.5(\text{stat}) \pm 1.6(\text{syst}) \text{ ppm}$  for detector B. These results are encouraging: with the new electronic setup we have obtained similar values for the transverse asymmetry with respect to the old measurement, that were based on the integration of the PMT current, instead of the detection of the single electron pulses. With this new electronic, it will be possible to measure, for the first time, at MAMI, the transverse asymmetry for lead target, important in prevision of the future parity-violating experiment that will take place at MESA accelerator.

# Appendices



## .1 Abbreviations

Here we report a list of common abbreviation:

- **EOS**: equation of state.
- **PV**; parity violating experiment.
- **BNSA**: beam normal single spin asymmetry.
- **ENMO**: energy monitor.
- **PIMO**: current monitor.
- **VFC**: voltage to frequency converter.
- **PMT**: photomultiplier tube.
- **RTM**: race track microtron.
- **XYMO**: position monitor.

## .2 Data Tree

In this section we discuss briefly the functions implemented to fill the data tree, from the monitor raw values. In the majority of the transverse asymmetry experiments, the position of the beam respect to the transverse plane is measured in three different position (see next figure). The three monitors are named XY21, XY25, XY26. During this experiment, only two monitors are available, XY25 and XY21, and are used in the analysis.

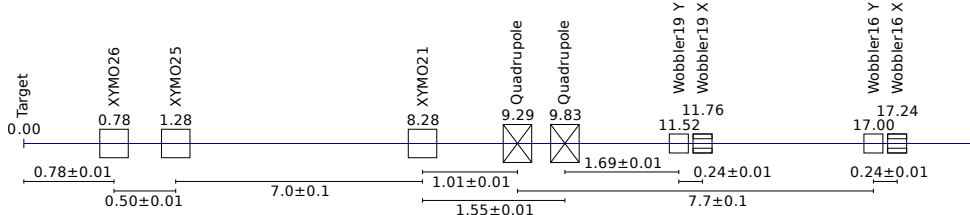


Figure 2: Scheme of the beam line, the target is on the left side of the picture.

Other monitors that are used are I21, I13 and E18, the current monitors and energy monitor, respectively. In the figure above, the current monitor I21 correspond to XY21. The E18 monitor, named also ENMO, and I13 are not shown in this picture, because they are placed in the racetrack RTM3 (see figure 2.3). The raw values from these monitors and the detectors are collected and stored in binary files produced by the A1 computer. The monitors data are made by integers numbers, the digital output of the voltage to frequency converter. The beam parameters measured by the beam monitors are saved in the class *Beam*, in figure 3.23. The output of the VFCs is proportional to the signal of the beam monitors, as shown in figure 2.14. The analysis program converts from raw counts to values in V using the formula is given in equation 2.16. Once the voltage values are computed, the analysis program does another conversion, from voltage to the physical units. The formula for this conversion is given in 4:

$$\frac{V \cdot scale - offset}{I} \quad (4)$$

In th formula the coefficient *scale* and *offset* are loaded from the standard configuration files, where all the scaling factors measured during the calibrations are stored. In the above formula we divide by the beam current *I*, because the output signal of positions and energy the monitors are proportional to the intensity of the beam, and need to be normalized. For the current monitor, the

signal is directly proportional to the current, so the denominator is omitted. The important quantities that are computed by the analysis program are:  $X$ ,  $Y$ , position of the beam on the target,  $\theta_x$  and  $\theta_y$  scattering angles, current  $I$  and energy  $E$ . These quantities are saved in a different class, the *Target* class. We now briefly present the function implemented to process the raw data and retrieve these quantities. The position  $X$  and  $Y$  are computed as explained in section 3.3.2. In brevity, assuming that the beam is moving in a straight line, the beam trajectory is described by:

$$\begin{aligned} y &= m_y \cdot z + q_y \\ x &= m_x \cdot z + q_x \end{aligned}$$

The values that we are looking for are  $q_x$  and  $q_y$ , x and y intercept. Imposing in the above equations the passage through the points  $(Z_{25};X_{25})$  and  $(Z_{21};X_{21})$ , the intercepts of the equation are given by:

$$q_x = \frac{Z_{25} \cdot X_{21} - Z_{21} \cdot X_{25}}{Z_{25} - Z_{21}} \quad (5)$$

The scattering angles  $\theta_x$  and  $\theta_y$  are instead related to the slope  $m$ , knowing that  $\tan(\theta) = m$ . The angles are given by the formula:

$$\theta_x = \frac{X_{25} - X_{21}}{Z_{25} - Z_{21}} \quad (6)$$

With these values, the analysis program compute the differences between different polarization states, that are the independent variables for the linear fit. The data tree contains other two classes: detector A and detector B. Each detector class is structured in a number of sub-classes equal to the number of the PMTs, where the counts are stored and processed. The raw data are saved in the variable *rawCounts*, that contains 4 integer number, one for each sub-events. Then the analysis program load the parameters saved in the standard configuration files, where the PMTs offset measured during the auto-calibration are stored. The *offsetCorrectedCounts* are given by equation 7

$$offsetCorrectedCounts = rawCounts - N_i \quad (7)$$

where  $N_i$  is the offset measured for PMT i. Other two variables, *positivePolarityCounts* and *negativePolarityCounts* are given by the sum of the offsetcorrectedCounts for sub-events with the same polarization. The *asymmetry* is given by the formula 8

$$asymmetry = \frac{(Pc[1] + Pc[2]) - (Nc[1] + Nc[2])}{(Pc[1] + Pc[2]) + (Nc[1] + Nc[2])} \quad (8)$$

where  $Pc$  and  $Nc$  stands for positive and negative polarity counts.

# List of Tables

3.1	Detector B counts for 10 acquisition of 1 min long, with $Att$ equal to 600.	42
3.2	Mean, variance and correlation coefficient for detector B and PMT in overlap.	42
3.3	Gosset test for detector B	42
3.4	Detector B counts for 10 acquisitions of 1 min long, with PMT $Ov$ in overlap.	43
3.5	Mean, variance and correlation coefficient for detector B and PMT in overlap.	43
3.6	Gosset test for detector B and the PMT in overlap, for the 10 acquisition in table 3.4	43
3.7	PMTs A2,A1,A0 counts for 10 acquisition of 1 min long.	44
3.8	Mean, variance and correlation coefficient for detector A and PMT in overlap.	44
3.9	Gosset Test for PMTs A2,A1,A0 of detector A.	44
3.10	Correlation coefficient between the PMTs (A2,A1,A0) and the PMT in overlap.	44
3.11	Best fit result for the model defined in equation 3.11	54
3.12	Attenuation settings for both the detectors.	54
3.13	Angular coefficient and offset obtained for the auto-calibration. The third column is contains the estimation of $c$ , as defined in equation 3.12	57
4.1	Beam parameters table, in the second column the mean $\mu$ with the standard deviation $\sigma_\mu$ of the mean is shown. The third column is $\sigma$ , the standard deviation of the distributions in figures 4.3.	62
4.2	Example of the Polarity sequence and PMT counts that are saved in the analysis program. The values of the PMT counts given are for example.	64
4.3	Reduced $\chi^2$ for the gaussian fit of the asymmetry data.	67
4.4	Correlation coefficient between beam parameters.	68
4.5	$\chi^2_{ndf}$ for the different models used to fit the data show in figure 4.13	70
4.6	Average counts per pmt, for time length of 20 ms.	73
4.7	Values for the false asymmetry, computed with the slow horizontal and vertical variation mode.	73
4.8	Lead rates, the values are measured for a target width of 0.5 mm.	75
4.9	Estimated time needed for the upcoming experiments to measure the transverse asymmetry for Lead with an aimed precision of 1.7 ppm for detector A and 2.8 ppm for detector B.	76
5.1	Averaged asymmetries over all the events. The values are corrected subtracting $\bar{A}_I$ and considering the effective polarization $p$ of the beam	77
5.2	Fit result with the linear model, for detector A.	79
5.3	Fit result with the linear model, for detector B.	79
5.4	Overall result for detector A and B.	79
5.5	Analysis result for the data with polarization loss	80



# Bibliography

- [1] M Thiel, C Sfienti, J Piekarewicz, C J Horowitz, and M Vanderhaeghen. Neutron skins of atomic nuclei: per aspera ad astra. *Journal of Physics G: Nuclear and Particle Physics*, 46(9):093003, aug 2019.
- [2] H. A. Bethe and R. F. Bacher. Nuclear Physics A. Stationary States of Nuclei. *Rev. Mod. Phys.*, 8:82–229, 1936.
- [3] J. Piekarewicz and M. Centelles. Incompressibility of neutron-rich matter. *Physical Review C*, 79(5), may 2009.
- [4] Richard H. Helm. Inelastic and Elastic Scattering of 187-Mev Electrons from Selected Even-Even Nuclei. *Phys. Rev.*, 104:1466–1475, Dec 1956.
- [5] C. J. Horowitz et al. Weak charge form factor and radius of  $^{208}\text{Pb}$  through parity violation in electron scattering. *Phys. Rev. C*, 85:032501, 2012.
- [6] S. Abrahamyan et al. Measurement of the Neutron Radius of  $^{208}\text{Pb}$  Through Parity-Violation in Electron Scattering. *Phys. Rev. Lett.*, 108:112502, 2012.
- [7] D. Adhikari et al. Accurate Determination of the Neutron Skin Thickness of  $^{208}\text{Pb}$  through Parity-Violation in Electron Scattering. *Phys. Rev. Lett.*, 126(17):172502, 2021.
- [8] F. J. Fattoyev and J. Piekarewicz. Accurate calibration of relativistic mean-field models: Correlating observables and providing meaningful theoretical uncertainties. *Physical Review C*, 84(6), dec 2011.
- [9] Lee Lindblom. Determining the nuclear equation of state from neutron-star masses and radii. *The Astrophysical Journal*, 398:569–573, 1992.
- [10] J. R. Oppenheimer and G. M. Volkoff. On Massive Neutron Cores. *Phys. Rev.*, 55:374–381, Feb 1939.
- [11] J Lattimer and M Prakash. Neutron star observations: Prognosis for equation of state constraints. *Physics Reports*, 442(1-6):109–165, apr 2007.
- [12] B. G. Todd-Rutel and J. Piekarewicz. Neutron-Rich Nuclei and Neutron Stars: A New Accurately Calibrated Interaction for the Study of Neutron-Rich Matter. *Phys. Rev. Lett.*, 95:122501, Sep 2005.
- [13] B. P. Abbott et al. GW170817: Observation of Gravitational Waves from a Binary Neutron Star Inspiral. *Phys. Rev. Lett.*, 119(16):161101, 2017.
- [14] Taylor Binnington and Eric Poisson. Relativistic theory of tidal Love numbers. *Phys. Rev. D*, 80:084018, 2009.
- [15] F. J. Fattoyev, J. Piekarewicz, and C. J. Horowitz. Neutron Skins and Neutron Stars in the Multimessenger Era. *Physical Review Letters*, 120(17), apr 2018.
- [16] B. P. Abbott et al. GW170817: Measurements of neutron star radii and equation of state. *Phys. Rev. Lett.*, 121(16):161101, 2018.

- [17] M. Gorchtein and C. J. Horowitz. Analyzing power in elastic scattering of electrons off a spin-0 target. *Physical Review C*, 77(4), apr 2008.
- [18] S. Abrahamyan et al. New Measurements of the Transverse Beam Asymmetry for Elastic Electron Scattering from Selected Nuclei. *Phys. Rev. Lett.*, 109:192501, 2012.
- [19] Mikhail Gorchtein. Doubly virtual Compton scattering and the beam normal spin asymmetry. *Physical Review C*, 73(3), mar 2006.
- [20] Oleksandr Koshchii, Mikhail Gorchtein, Xavier Roca-Maza, and Hubert Spiesberger. Beam-normal single-spin asymmetry in elastic scattering of electrons from a spin-0 nucleus. *Physical Review C*, 103(6), jun 2021.
- [21] A. Esser et al. First Measurement of the  $Q^2$  Dependence of the Beam-Normal Single Spin Asymmetry for Elastic Scattering off Carbon. *Phys. Rev. Lett.*, 121(2):022503, 2018.
- [22] B. S. Schlimme et al. Vertical Beam Polarization at MAMI. *Nucl. Instrum. Meth. A*, 850:54–60, 2017.
- [23] Robert Goldstein. Pockels Cell Primer. *Laser Focus*, 34:21, 1968.
- [24] Timothy Gay and F. Dunning. Mott electron polarimetry. *Review of Scientific Instruments*, 63:1635 – 1651, 03 1992.
- [25] M. Dehn. Strahldiagnostik und Analyse der optischen Eigenschaften des Strahlführungssystems von MAMI. *Diplomarbeit*, 2004.
- [26] Single and Multichannel, Synchronous Voltage-to-Frequency Converters, AD7741. *Analog Devices*.
- [27] F. Anghinolfi, P. Jarron, F. Krummenacher, E. Usenko, and M.C.S. Williams. NINO, an ultra-fast, low-power, front-end amplifier discriminator for the Time-Of-Flight detector in ALICE experiment. In *2003 IEEE Nuclear Science Symposium. Conference Record (IEEE Cat. No.03CH37515)*, volume 1, pages 375–379 Vol.1, 2003.